CLASSIFICATION OF LIVER DISEASES USING CT AND MR IMAGES

A Thesis

submitted for the award of

DOCTOR OF PHILOSOPHY

by

ABHAY KRISHAN

Registration No. 901204001

Under the Supervision of

Dr. DEEPTI MITTAL

Associate Professor

Department of Electrical and Instrumentation Engineering

THAPAR INSTITUTE
OF ENGINEERING & TECHNOLOGY
(Deemed to be University)

Department of Electrical and Instrumentation Engineering

THAPAR INSTITUTE OF ENGINEERING & TECHNOLOGY

(Deemed to be University u/s 3 of UGC Act., 1956)

Patiala-147004, Punjab (INDIA)

JULY-2021

CERTIFICATE

I hereby certify that the work which is being presented in thesis entitled **"CLASSIFICATION OF LIVER DISEASES USING CT AND MR IMAGES"** submitted to the Department of Electrical and Instrumentation Engineering, Thapar Institute of Engineering and Technology (Deemed to be University), Patiala in the fulfilment of the requirements for the award of degree of **"Doctor of Philosophy"** is an authentic record of my own research work carried out under the guidance of **Dr. Deepti Mittal** and refers other research work, which are duly listed in the reference section.

The matter presented in this thesis has not been submitted in part or full for the award of any degree in any other University or Institute.

(ABHAY KRISHAN)
Registration No. 901204001

This is to certify that the above statement made by the candidate is correct and true to the best of my knowledge.

(Dr. Deepti Mittal)
Associate Professor
Department of Electrical and Instrumentation Engineering
Thapar Institute of Engineering & Technology (Deemed to be University)
Patiala, Punjab, India

ACKNOWLEDGEMENTS

I want to express my heartiest gratitude, indebtedness, and sincere appreciation to my esteemed supervisor, **Dr. Deepti Mittal** (Associate Professor, Electrical and Instrumentation Engineering Department, TIET), for his continuous inspiration, support, guidance, encouragement, advice, patience and feedback throughout my Ph.D. I felt very grateful and blessed to have worked under her supervision. He always motivated me to achieve my research goals. Most of the novel ideas found in this thesis are the result of our numerous discussions. Her editorial comments were very meaningful and significant for writing this thesis.

I am thankful to Dean of Research and Sponsored Projects **Dr. Rafat Siddique** for his support during the thesis work. I would like to express my heartfelt gratitude towards **Dr. Prakash Gopalan** (Director, TIET, Patiala), and **Dr. R.S. Kaler** (Head, Electrical and Instrumentation Engineering Department), for providing me with the facilities and support to complete this research work. I am also thankful to **Dr. Gurbinder Singh** (Registrar, TIET, Patiala) for his support in the smooth proceeding of the administrative needs associated with the work.

I would like to thank the esteemed members of my Doctoral Committee, **Dr. Kulbir Singh,** Professor, Department of Electronics and Communication Engineering, Thapar Institute of Engineering & Technology, **Dr. Gagandeep Kumar,** Associate Professor, Department of Electronics and Communication Engineering, Thapar Institute of Engineering & Technology and **Dr. Jainy Sachdeva,** Associate Professor , Department of Electronics and Communication Engineering, Thapar Institute of Engineering & Technology for their constructive comments and regularly ensuring the progress of my research work. I would like to thank the faculty and staff members of the Electrical and Instrumentation Engineering Department, Thapar Institute of Engineering & Technology for their day to co-operation.

I would like to thank Dr. A.K. Bansal Consultant-medical physicist radiation oncology, MAX Hospital, Saket, New Delhi, for helping in providing the medical images dataset.

Most importantly, I am incredibly thankful to my **Parents** for their support, boundless love, affections and blessings all the time.

Finally, I am thankful to my Family members and my Friends, for their support and encouragement, as the present work is finally concluded.

(ABHAY KRISHAN)

Dedicated

to my

Father Shri Yogendra Kumar

and

Mother Smt Mandalsa

ABSTRACT

Over the last few decades, liver cancerous diseases have become a major leading cancer disease worldwide. The classes of liver cancer diseases enable further investigation with the diagnosis as the pre-treatment. Early detection and diagnosis lessen the need for many implanted diagnostics, and receiving treatment sooner are advantageous. As a result, the current study was carried out to diagnose the many types of liver cancer diseases and their classifications, levels of tumor, and interpretation. The diagnosis of liver cancerous disorders is based on detecting and classifying the diseases: Hepatocellular carcinoma (HCC) and Metastases (MET). However, variability within the liver tumor portion allows a different class of intensities as the normal region and tumor region intensities mix-up. As a result, it is essential to perform the processing work that results in a varied tumor appearance in the images. An effective Computer Aided Diagnosis (CAD) system is designed to identify, classify, and interpret the level of liver tumor classes. We created a composite database that allows us to execute image processing work rapidly to complete the procedure. This database has a huge number of images for all tumor classes. The data images enable thorough analysis with all objectives work, resulting in the desired effect outcomes.

In this research work, a composite database was created that included 4566 images from the CT and MR imaging domains for both the normal liver and the tumor region of the liver. Several classes in this composite database are described by the medical domain, including tumor classes and normal liver classes. There are 1957 abnormal CT and MR tumor images and 2609 normal CT and MR images. There are a total of 1054 abnormal MR tumor images and 2274 normal MR domain images. There are 844 abnormal CT tumor images and 395 normal CT domain images in total. For the tumor images, 600 MR images of HCC images and 513 MR images of MET were used, 361 CT images of HCC and 483 CT images of MET were used. These images were formed as a result of data collecting from several hospitals between January 2013 and July 2016. For the CT imaging, data were obtained from 15 patients, 15 normal liver patients, 4 HCC patients, and 16 MET patients. Four normal liver patients, six HCC patients, and nine MET patients were selected for MR imaging. Many of these patients have multi-phase data, meaning they have more than one phase of the same condition with varying specifications. The entire database, which has various aims, qualities, and levels of completeness. As a result, a data structure was created to handle the image processing work.

Medical image factors include blur and artifacts that reduce contrast resolution, blurring two separate classes of intensities, and not allowing the required information to be obtained. Their presence complicates liver cancer diagnosis and interpretation. As a result, normal and malignant images of the liver are pre-processed. This is done utilizing the contrast limited adaptive histogram equalization (CLAHE) and constrained variational histogram equalization (CVHE) algorithms. Both approaches equalize histograms. Histogram equalization (HE) is image enhancement for low contrast images. As part of the pre-processing, photos are enhanced. Bilinear interpolation removes the CLAHE-induced boundary of these locations. CLAHE's CT image processing is robust, reliable, and flexible. With the CVHE method, you get the

benefits of the histogram equalization algorithm in contrast enhancement for gray level images while preserving the overall quality of the image. A differentiated look with the tumor for varied class intensities resulted in the tumor increased regions. The improved images were verified and confirmed by qualified radiologists using visualization.

An automated CAD technique for the detection and the classification of multi class liver cancer diseases using the CT and MR images is developed. The primary liver cancer is HCC, and the secondary liver cancer is MET. The CLAHE enhanced images offer a better tumor look on visualization than the original. The features are extracted from the enhanced images for the identification and categorization of liver tumors. For non-tumor types, the Region of Interest (ROI) may be the normal liver portion and for malignant types, the tumors region ROI can be 30 × 30 or 25 x 20 pixels. With these pixels, the class features are evaluated. First order statistics (FOS), Gray Tone Difference Matrix (GTDM), Gray Level Co-Occurrence Matrix (GLCM), and Gray Level Run Length (GLRLM). This study employs numerous internal ROIs (ranging from 1-5) from a given enhanced image in the FOS, GLCM, and GTDM. Individual and group features are used to classify the IROI. The ratio feature compares the IROI and SROI feature values. Feature class may be a type of feature or a set of characteristics selected based on their individual classifier rate. A Genetic Algorithm (GA) is used to choose the IROI and ratio features automatically. SVM classifier classifies automatic and manual feature selection. With all the derived features utilizing ROI, tumor detection is possible using normal and malignant images. When a tumor is detected, it is classified as HCC or MET. Decision tree, Adaboost, Random Forest (RF), Support vector machine (SVM), Generalized Linear Model (GLM) and Neural network (NN) were used in study 2. Detection and classifier accuracy rate and area under the curve are improved using a multi-level ensemble (AUC). The sensitivity/specificity and recall/precision curves are assessed. The classifier rate was tested using k-fold cross-validation (CV).For the study 3, The Gabor filter scaling and orientation parameters are designed for the detection and classification. The optimized Gabor filter is used by five different scaling and eight orientation parameters, yields 40 different filters that cover the frequency domain, in multi resolution. The experiments are designed for detection and classification using CT, MR and the combination of the CT and MR images. The ROI is used as the inputs for the scaling and the orientation of Gabor filters using the classifier accuracy, AUC, sensitivity/specificity and the precision by all the six classifiers. The CV has been done on the best classifier to check their robustness with the detection and the classification experimentations.

CT and MR images are segmented using the OKK-means clustering algorithm, which outperforms the previous accuracy, sensitivity, and specificity approaches. It eliminated noise with adaptive median filtering. Histogram equalization reduces the noise. The OKK-means clustering technique and the oppositional firefly algorithm (OFA) are used to choose the best features from the feature sets.

Image registration is performed using a multi-phase CT image of the same patient. The moving and fixed images are selected to get the registered image for mutual information (MI). There are two extracted features: maximally stable extreme regions (MSER) and Speeded up robust features (SURF).

This helps to give correct registered images. The registered images differ in color combinations. A good output form, color combination, output look, or proper difference of images offers MI with registered images.

These results aid the radiologist as a second opinion for liver cancer diagnosis. The output parameters assist in the assessment of the tumor size and comment on tumor level in those images. Before treatment, the images of the tumor should be analyzed. The treatment should be based on the size and location of the liver tumor. This allows the radiologist to obtain tumor classes, show level information, and analyze many features of the tumor prior to diagnosis, utilizing both CT and MR images. To assist the radiologist, the more delayed phases contain more regions in the registered images. To gather more information, the radiologist needs to capture more stages images.

Finally, the current research includes (i) liver image enhancement utilizing HEs methods, (ii) liver tumor identification and classification using ROIs and classifiers, (iii) segmentation of liver tumor, and (iv) registration of multi-phase CT images. Trying to assist radiologists, these computer-aided diagnosis experiments work provides the generalization of a clinical database, to analyze the position and size of the tumor and proves generalization ability, in real-time diagnosis of detection, classification, level of the tumor and the way to do the analysis before the treatment.

List of Publications

1) Abhay Krishan and Deepti Mittal, "Effective segmentation and classification of tumor on liver MRI and CT images using multi-kernel K-means clustering" *Biomedizinische Technik/Biomedical Engineering*, vol. 65, issue 3 pp. 301–313, 2019.
   doi: doi.org/10.1515/bmt-2018-0175
   Publisher: De Gruyter, Category: SCI/SCIE, Impact factor: 1.44
2) Abhay Krishan and Deepti Mittal, "Ensembled liver cancer detection and classification using CT images", Journal of engineering in medicine, vol. 38, no. 1, pp. 27–53, 2020.
   Doi: doi.org/10.1177/0954411920971888
   Publisher: Sage journal, Category: SCI/SCIE, Impact factor: 1.617
3) Abhay Krishan and Deepti Mittal, "Feature based CT image registration of Liver Cancer", Journal of engineering in medicine (accepted).
   Publisher: Sage journal, Category: SCI/SCIE, Impact factor: 1.617
4) Abhay Krishan and Deepti Mittal, "Multi classes liver cancer diseases classification using CT images", The Computer Journal (under review).
   Publisher: Oxford Univ Press, Category: SCI/SCIE, Impact factor: 1.494
5) Abhay Krishan and Deepti Mittal, "Detection and classification of liver cancer using CT images", International Journal on Recent Technologies in Mechanical and Electrical engineering, vol. 2, no. 5, pp. 93–98, 2015.
   Publisher: Auricle Technologies, Category: non-SCI
6) Abhay Krishan and Deepti Mittal, "Performance of CT Metastases and compare their results with others" International Conference on Signal Processing and Communication Engineering Systems, pp. 380–383, 2015.
   Publisher: IEEE Xplore, Category: Conference
7) Abhay Krishan and Deepti Mittal, "Feature identification to detect CT Metastases" 2nd National conference on Recent trends in Electronics and Electrical engineering (NCRTEEE-2018), pp.200-205, 2018.
   Publisher: IEEE (UP Section), Category: Conference

List of Abbreviations

AUC	Area Under Curve
BP	Back Propagation
BPNN	Back Propagation Neural Network
CAD	Computer Aidid Diagnosis
CLAHE	Contrast Limited Adaptive Histogram Equalization
CNN	Convolutional Neural Network
CT	Computed Tomography
CV	Cross Validation
CVHE	Constrained Variable Histogram Equalization
DICOM	Digital Imaging and Communications in Medicine
FCM	Fuzzy c-means Clustering
FDCT	Fast Discrete Curvelet Transform
FN	False Negative
FNR	False Negative Rate
FOS	First Order statistics
FP	False Positive
FPR	False Positive Rate
FV	Feature Value
GA	Genetic Algorithm
GLCM	Gray Level Co-occurrence Matrix
GLM	Generalized Linear Model
GLRLM	Gray Level Run Length Matrix
GTDM	Gray Tone Difference Matrix
HCC	Hepatocellular Carcinoma
HE	Histogram Equalization
HEM	Hemangioma
HEP	Hepatoma

ICA	Individual Classification Accuracy
IROI	Internal Region Of Interest
MET	Metastases
MI	Mutual Information
MMI	Maximization of Mutual Information
MRI	Magnetic Resonance Imaging
MSER	Maximally Stable Extreme Region
NN	Neural Network
NPV	Negative Predictive Value
OCA	Overall Classification Accuracy
OFA	Oppositional Fruit Fly Algorithm
OKK-means	Optimal kernel K-means
PCA	Principal Component Analysis
PPV	Positive Predictive Value
QPO	Quadratic Program Optimization
RBF	Radial Bias Forward
RDL	Regularized Distance Level
RF	Random Forest
ROC	Region of Convergence
ROI	Region of Interest
SGLDM	Spatial Gray Level Difference Matrix
SROI	Surrounding Region of Interest
SURF	Speeded Up Robust Features
SVM	Support Vector Machine
TN	True Negative
TP	True Positive
WT	Wavelet Transform

List of Figures

List of Tables

Chapter 1

1. INTRODUCTION

Liver cancer is the most occurring diseases throughout the world since last few decades. Every year millions of people either died or diagnosed with liver cancer. American cancer society estimates about 42,810 new cases (30,170 in men and 12,640 in women) diagnosed and about 30,160 people (20,020 men and 10,140 women) died by the primary liver cancer and intrahepatic bile duct cancer in the United States in 2020 [1]. Clinical trials are the way to get state-of-the-art cancer treatment. Detect liver cancers at their early symptomless clinical stage to provide an effective diagnostic treatment with the increase in recovery rate. Further, the medical treatments at later stage of liver cancers are less effective. Therefore, in order to avoid much suffering of patients, doctors need to have a second opinion about the type of liver cancer and want to be become assured about their line of treatment. In this scenario, computer-aided identification and classification methods may aid to the doctors in their decision making. Even in the absence of expert opinion, computer aid detection and classification methods are a need of the time and provide a less costly preposition for the second opinion [2]. Therefore, the present research work is focused on the designing of a computer-aided system for the detection of liver cancers at an earlier stage and to classify them into the major categories.

It is not easy to find liver cancer at its early stage with the reason that signs and symptoms do not appear until it reaches up to later stages. The most commonly used diagnostic techniques for the detection of liver cancer are the alpha-fetoprotein (AFP) blood tests, whereas many experts often recommend ultrasound along with the AFP test [3]. In the clinical practice, usually doctors prefer to go for a non-invasive imaging modality to make initial diagnosis about the disease. These non-invasive modalities are usually ultrasound and most of the time computed tomography (CT) or magnetic resonance imaging (MRI) depending on the patient conditions, need of the time, availability, cost involved and above all of these, the opinion of expert/doctor involved. Whatever the reason, non-invasive imaging modalities like CT and MRI are frequently used to get the inside pictures of the body, to diagnose liver with initial signs and symptoms, to get the precise information about the size, shape and position of tumors in the liver and to distinguish between benign and malignant tumors [4, 5].

Accurate cancer detection and classification is utmost important in liver cancer diagnosis and treatment planning. Hepatocellular carcinoma is the most common primary liver cancer that start in the liver itself. Other common type of cancer is metastatic, a secondary liver cancer that can spread to the liver from other organs of the body. Treatment for liver cancers is most effective when it is diagnosed at early stage and its type is clearly known. Therefore, in the present research work, CT and MR images are used to design a computer-aided system to detect and classify hepatocellular carcinoma and metastatic cancers.

1.1 PREFACE

Liver cells that grow out of control become abnormal liver cells. That abnormal liver cells start forming the lump that is called as cancerous tumor or liver cancer. Cancer cells have damage DNA. Liver cancers are the result of many causes of dysfunction of liver or other organs. Every year millions of people are died or diagnosed with liver cancer. The liver cancer can be classified as the primary liver cancer and the secondary liver cancer. These categories are defined according to their origin of occurrence in the liver. Hepatocellular carcinoma (HCC) is the most common primary liver cancers mostly occurs in adults. About 80% of the liver cancers that originate in the liver are HCC. Cancer that starts from somewhere else and then affects the liver, is the secondary liver cancer. Metastases is the most common secondary liver cancer. The primary liver cancer HCC represents the fastest rising cause of cancer-related death in the US. It accounts for 75–85% of primary liver cancers and is the second leading cause of cancer death in East Asia and sub-Saharan Africa and the sixth most common in western countries [6]. Secondary cancer MET is responsible for about 90% of cancer related deaths worldwide [7]. Figure 1.1 shows the various parts details of the liver and the main functioning of the organ. Figure 1.2 depicts the photographic view of healthy liver, liver with hepatocellular carcinoma and liver with metastases.

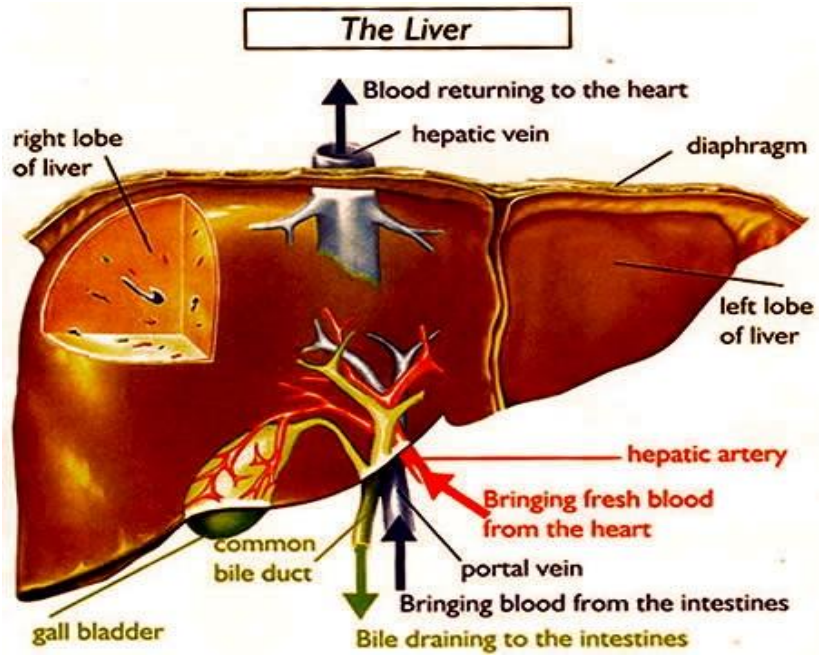

Figure 1.1: The details of liver organ and its functioning with all the nearby connecting parts inside the human body.

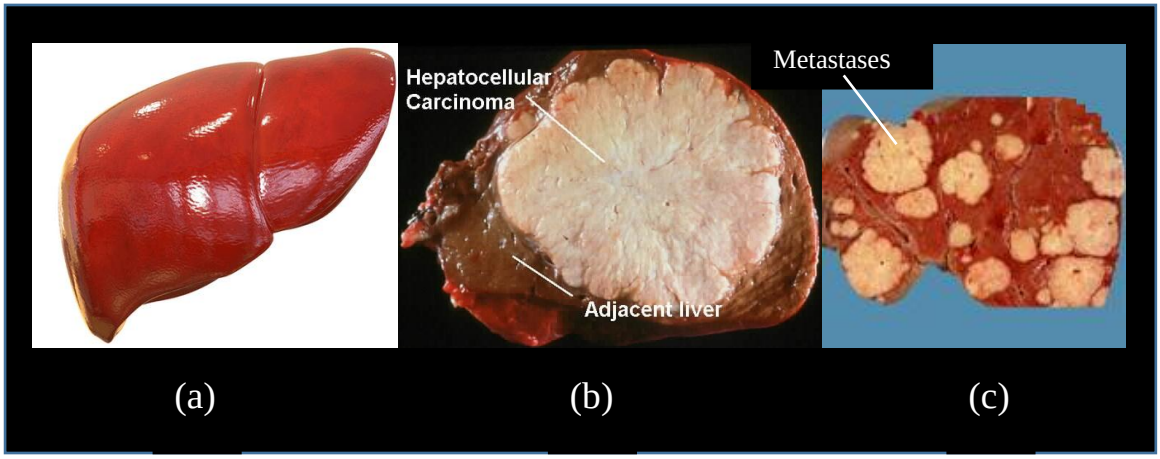

Figure 1.2: Images of (a) healthy liver, (b) liver with hepatocellular carcinoma and (c) liver with metastases.

1.2 LIVER IMAGING MODALITIES

There are various imaging techniques to identify the liver tumor, blood test, biopsy and image test. Blood test and biopsy is an invasive, time consuming, cumbersome and painful techniques. Medical imaging modalities that do not penetrate the skin physically are non-invasive. The non-invasive imaging modalities to detect the liver tumor are MRI, X-ray,

Ultrasound and CT-scans. Medical imaging is the technique and process of creating visual representations of a body's internal organs for clinical analysis and medical intervention, as well as visual representation of the function of certain organs or tissues. These techniques are not only helpful in detecting the tumor size and locations but also helps in finding that tumors spreading in the different parts/regions of the human body. In the medical field, physicians routinely identify structures in medical images to facilitate the treatment of patients [8]. Medical image processing generates a lot of data and to analysis that data set manually, an automated computer aided diagnosis (CAD) techniques to diagnose the tumor in real-time and that lead to improve in the data image analysis [9].

All modalities have its advantages and limitations. The choice of which modality to use is determined based on the expert radiologist, the availability of the equipment, the condition of the patient, and the experience of the radiologist. Information contained in confocal micrographs, CT, MRI and fMRI scans are the best conveyed through a flexible and realistic 3D visualization system that combines adjacent slices into a 3D image volume [10]. So, the present work is done by using the CT and MR images for the liver organ as shown in Figure 1.3, it allows to collect the usual information in combination and independently for both of them.

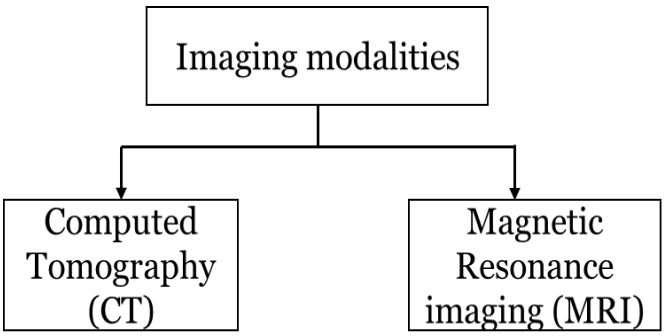

Figure 1.3. The present work imaging modalities are the CT and the MRI. In the present work, the experimentation work is done using the CT and MR images.

There are various machines used to do the processing of the CT and MRI image scans. For both of these type of scans, the patient lie in a tunnel like machine, the machines inside parts rotates and generating the pictures, these pictures send to the computer combined to form the image slices. They may also be combined to produce a 3-D image of a particular area of the body. The following two figures represents the details of the CT and MR machine, with their details image processing.

1.3 CT AND MRI

The whole analysis of number of pathologies such as tumor and edema by radiologist using CT and MR images is a dynamic analysis and differentiating the position of tissues continues to be a challenging task which is susceptible to error. Extension or modifications in the tumor volume and its elements are likely to serve as signals for disease progression for being employed to decide the appropriate treatment and also to assess its efficiency.

1.3.1. Computed Tomography (CT) images

CT is a capable of obtaining many images from different angles and joins them together to produce multiple cross sectional images of the head with special X-ray equipment [12]. CT images widely adopted having high imaging speed, excellent spatial resolution, and relatively low cost. CT images are the two-dimensional images in the form of the slices of a particular organ of the human body by the process of rotation. CT processing is a single-phase CT and multiphase CT. The X-ray beam moves throughout the detector only once, in single-phase CT. In multi-phase CT, there are repeated processing of CT scan with different specifications, that are the different phases. CT evaluates the scanning for various specific symptoms such as pain, dizziness, vomiting, *etc.*[13]. A tumor present in the CT image has a continuation with a particular series. The CT images due to the intensity difference may provide detection and the classification for the tumor classes. CT images have the advantages to obtain those parts in an organ that not seen with standard X-ray or ultrasound.

CT machine has the main components, as the X-ray tube, Gantry, detector, and Control console. Gantry is the main body of the CT scanning machine, which contains CT X-ray tube, High voltage generator, Detector array, Data acquisition system and Slip ring. X-ray modality used in the cross section of the human body. The detector elements captures energy that has not been attenuated by the patient. The control console set scanned parameters.

Multi-phase CT images

In multi-phase CT, there are repeated processing of CT scan with different specifications, that are the different phases. Multi-phase CT images are the different phases, repletion of the same phase with some specifications may be injected into the veins or the artery, or delayed by some seconds/minutes. Arterial phase imaging is most useful for the detection of HCC as its predominant blood supply is from the hepatic artery. Multi-detector

CT has a higher sensitivity in the detection of HCC in patients with cirrhosis due to increased speed and improved spatial and temporal resolution [14]. Figure 1.6 represents the image how the multi-phase data is being processed to generate.

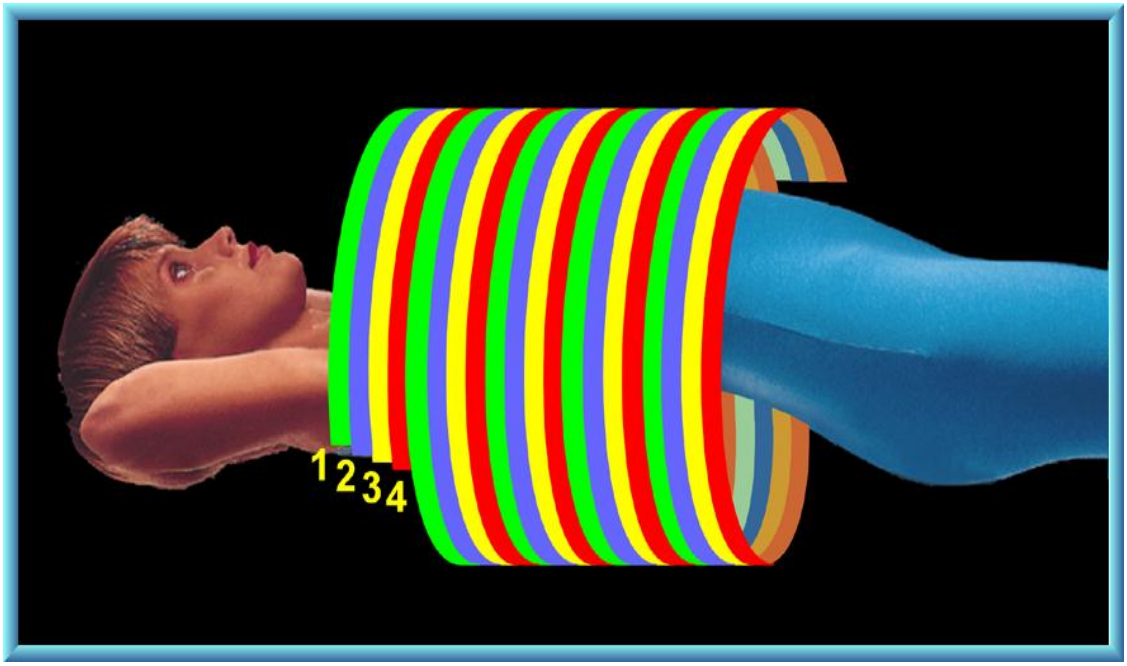

Figure 1.4. The multi-phase CT image processing data. It represents the four phase's indication with the CT images. A patient undergoes a CT machine for interpreting the multi-phase CT.

1.3.2. Magnetic Resonance Imaging (MRI)

A magnetic with a field strength of 1.5 Tesla (T) or higher required to optimally perform a liver MRI [15]. High field strengths generally produce images with the greatest liver to lesion contrast and have shorter image acquisition times. MRI has the advantages, high contrast in case of soft tissues, avoidance of ionization radiation and the iodinated contrast media, and the possibility of performing functional imaging sequences. Liver MRI protocols usually use a combination of T1-weighted, inversion recovery, and T2-weighted images. These provide complimentary information for image interpretation.

Liver MR is more sensitive and accurate for the detection and characterization of focal lesions than CT or US. Specific sequences such as invers ion recovery, highly sensitive for the detection of lesions. MRI provides the unique ability to interrogate multiple parameters such as T1, T2, diffusion characteristics, and enhancement patterns of focal liver lesions, enabling liver lesion detection and characterization. Most normal tissues possess short T1 and T2 values. Benign liver lesions such as cysts and hemangiomas have longer T2 relaxation times than other primary liver lesions and most metastases, appear brighter on T2-

weighted images [14]. The following Figure 1.7 represents the detailed parts of the MRI machine.

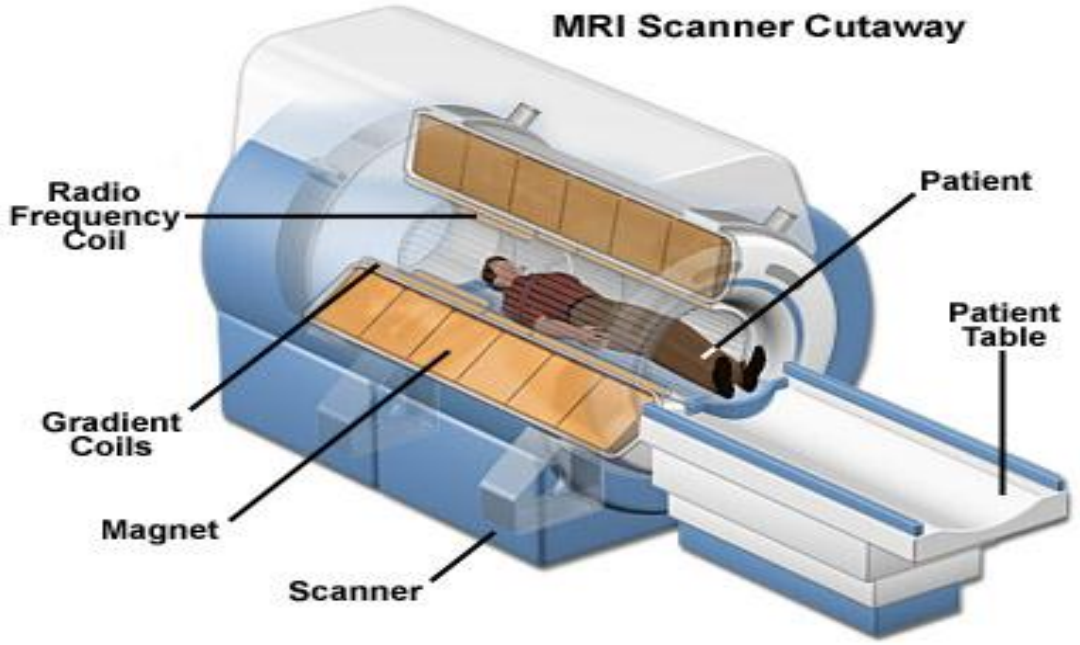

Figure 1.5. The detailed parts of MRI machine. In this picture, the patient lies on the patient's table. When the scanner going on, the Radio frequency coil, gradient coils and magnet processing works, that results in the MR Images.

Components of the MRI Scanner machine:

- **Magnet:** It provides a strong, uniform, steady magnetic field for the MRI processing of the system.
- **RF Transmitter:** It is the Radio frequency transmitter. It delivers radio frequency magnetic field to the sample.
- **Gradient system:** It produces time varying magnetic fields of the controlled spatial non-uniformity.
- **Detection system:** It yields the output signal.
- **Imager system:** It includes the computer, which reconstructs and display the images.

Liver specific MR contrast agents may be used in selected clinical situations when the goal is to achieve the highest detection rate for liver focal lesions.

1.4 LIVER ANATOMY AND CANCER DISEASES

The liver is a largely composite design, and its fragmentation is a crucial step for many issues, grouped with studies in temporal change detection of morphology, and three-

dimensional (3D) visualizations for surgical planning. Liver is the largest organ that plays a very important role in the human body, it supports many organs in the body. The main functions of liver are to filter the blood and change food into energy. The liver lies below the diaphragm in the abdominal-pelvic region of the abdomen. Its strategic location and multidimensional functions, prone to many diseases. Excessive fat of the body, excessive intake of alcohol and increasing age factors also leads to various liver diseases. Liver diseases are mainly classified as, diffuse liver diseases and the Focal liver diseases. Diffuse liver disease s are the diseases that have symptoms on the complete liver and the focal liver diseases are the diseases that have symptoms on a particular part of the liver. The present work is all about the focal liver diseases. Liver tumors are discovered on medical imaging equipment or present themselves symptomatically as an abdominal mass, abdominal pain, jaundice, nausea or liver dysfunction. To avoid or prevent liver cancer early diagnosis is needed [11].

1.4.1. Normal Liver

On the CT and MRI, the appearance of normal liver is isoechoic and homogeneous. The normal liver on the CT is of uniform echo reflectivity, composed of low and medium echoes. Therefore, its ecogenicity can be said as of isoechoic nature. Also, normal liver has a homogeneous echo texture; the numerous vessels coursing through the organ give it a “salt-and-pepper” appearance [8, 9].

1.4.2. Hepatocellular Carcinoma (HCC)

HCCs differ in signal intensity on T1- and T2- weighted images. A large HCC has fibrous tumor appearing hypo-intense on T1- and T2-weighted images, rarely hyper-intense on T2-weighted images, with delayed enhancement. Most small HCCS show intense arterial phase enhancement. Most HCC are characteristically hypo-intense on T1 W and hyper-intense on T2 W images with intense enhancement during the hepatic arterial phase of a dynamic gadolinium contrast [10].

1.4.3. Metastases (MET)

Liver metastases are variable in their T1 and T2 signal intensities but are usually prolonged resulting in hypo- to iso intensity on T1W images and iso to hyper-intensity on T2W images. T1 weighted imaging is performed with the breath hold Spoiled Gradient Echo (SGE) technique. It advantages, fast data acquisition, avoidance of breathing artifacts and

complete coverage of the liver in a single breath hold. T2 weighted imaging is most frequently performed as echo train spin echo. In phase and opposed phase T1 W gradient echo images are useful for the evaluation of fatty infiltration of lesions. Liver metastases tend to lose signal in heavily T2W images. Metastases show the doughnut sign on T1W images and target sign on T2W images. A hyper-intense on T1W images described for various liver metastases due to internal component of paramagnetic substance. Hyper vascular metastases show peak enhancement in hepatic arterial phase images. MR imaging with gadolinium chelates offers an accurate non-radiation based imaging test for detection of liver metastases [14].

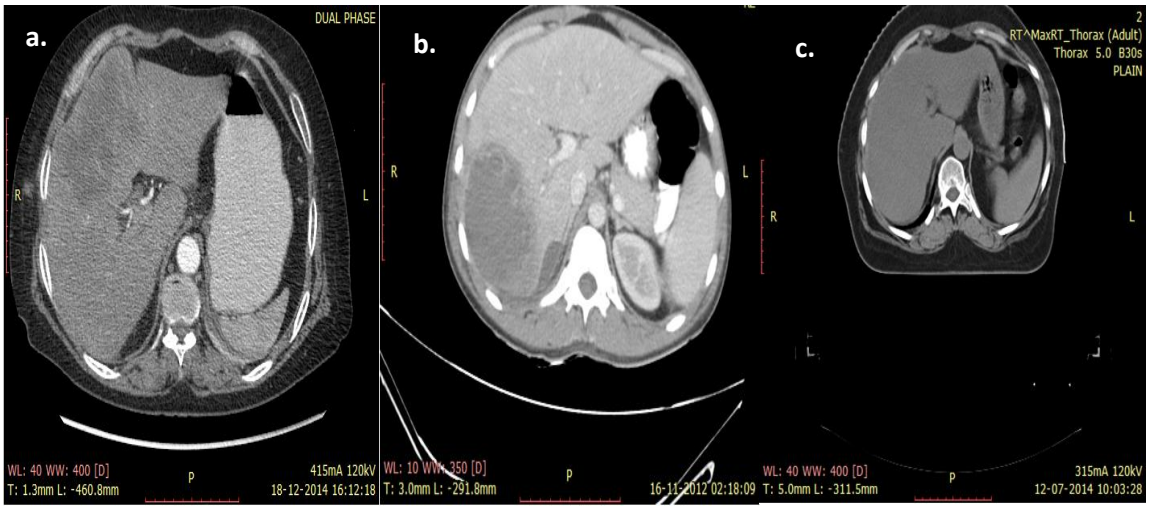

(a) HCC **(b) MET** **(c) Normal liver**

Figure 1.6: (a), (b) and (c) are the original images for the HCC, MET and the normal CT scan images of the liver, respectively. These images are the original images that collected from the Hospitals.

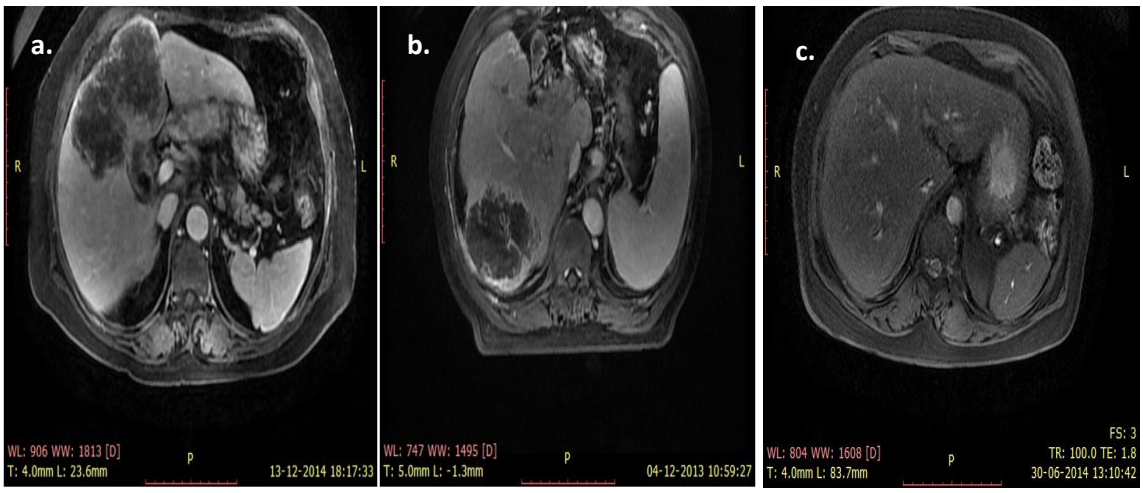

(a) HCC **(b) MET** **(c) Normal liver**

Figure 1.7: (a), (b) and (c) are the original images for the HCC, MET and the normal MR scan images of the liver, respectively. These images are the original images that collected from the Hospitals.

Most of the liver cancers don't have any symptom with the earlier stage that is difficult to detect but the cancer functions destroy the liver cells properly.

The major challenges in the liver anatomy are noise, Intensity Non-Uniformity (INU), partial volume effect, structure complexity and natural tissue intensity variations.

The segmentation of images is utilized to place and determine objects and boundaries (lines, curves, etc.) in the images.

1.5 NEED OF THIS PRESENT WORK

The present work deals with the CAD system designing to detect the liver cancer, for the classification of the cancerous diseases and to categorize them with primary and the secondary liver diseases, as the HCC and MET classes respectively. Very few researchers worked with the designing of CAD system for the classification of different classes' cancerous diseases.

The present work is with the large number of the CT and MR images database, which have a better look with the liver anatomy information. There is pre-processing using a suitable CLAHE algorithm to get a better look with the images. These algorithms allow to get a better visualization with the tumor, CLAHE have a better noise removal characteristics. The experiment for IROI, on the tumor enhanced tumor portion of the image. Sub-experiments using IROI values, with various class of features. There is automatic selection of features by feature selection and manual selection of features by types of features or groupings. The ratio features to check the ratio classifier rate by automatic and manual feature selection. These selected features are classified using a particular classifier. The CT enhanced images ROIs are classified using six classifiers and also ensemble them to increase their classifier rate. These have the feature selection both the way, to get a better result variation with the number of the features and to compare the individual classifier results, get the best classifier and improve their overall results. The ROIs are worked for the optimization of Gabor filters using different scaling and orientation parameters by CT and MR images. These Gabor filter parameters work for detection and classification of liver cancer diseases using all the six

classifiers with different combinations of the images. It allows getting the combination of the CT and MRI, to get a better way for the detection and the classification of the liver tumor. The segmentation and classification is done using both the CT and MR images using K-means clustering method in addition with the conventional firefly algorithm. In the diagnosis, the information about the single-phase CT image not provides too much desired information. The multi-phases CT images registration improve the acquired information. The same patient have the multi-phases records to extract more information, as the mutual information of two particular phases for the early diagnosis based on that particular phase using the image registration.

1.6 OBJECTIVES OF THE PRESENT STUDY

The following objectives of the present study to detect, extract and classify the liver cancer diseases using CT and MR images:

1. Development of the medical **image database** of CT and MR images with normal liver, liver with HCC and liver with MET diseases and multi-phase CT images.
2. Image enhancement of the acquired medical images.
3. Extraction of mathematically important **features** to discriminate HCC and MET from the CT/MR images.
4. **Classification** of HCC and MET with CT and MR images.
5. Image **segmentation** of tumor area from the CT/MR images.
6. Image **registration** in case of multi-phase CT images.

1.7 CONCLUDING REMARKS

The proposed work focuses on the automatic detection and classification of several types of liver cancer utilizing CT and MR images. The image has been pre-processed to provide a better understanding of the tumor visualization. An appropriate size ROI extracted from the tumor or liver region for the enhanced images to obtain the features. The calculated features are used to detect the liver, and once detected, the liver tumor is classed as either primary or secondary. The feature selection is carried out in order to select the features with the highest rank of features [15]. The feature selection group is intended to choose between automatic or manual feature selection to test the classifier rate variation. To evaluate the classifier rate variation, the classifiers may be single or multi classifiers, and their rates may be ensembles

to increase the classifier rate. The classifiers could be the final classification rate for the work's needed classification.

The segmentation procedure begins with a classification that differentiates between the normal and the tumor. The features are extracted and selected in order to minimize the features using a suitable algorithm and classify them as normal or tumor. Segmentation that uses a multi-kernel K-means clustering approach to remove the abnormal section from the original images.

The registration of multi-phase CT images using the efficient methodology. To extract mutual information about two selected phases from a multi-phase system. The registration improves the image acquisition information. The specific phase information and their combination allow for extracting meaningful information about a phase and its application in experiments.

Chapter 2

LITERATURE REVIEW

2.1 INTRODUCTION

Computer-aided diagnostic aid to radiologist plays a vital role by carrying out repetition of the imaging phases in the detection and diagnosis of the liver cancer imaging [10, 12]. Apparently, several techniques, such as enhancement, extracted features with the liver cancer input images, selection of the features, various classifiers to get the best classifier results, Gabor filter scaling and orientation methods, segmentation methods, registration methods are being used to develop such aids for the quantitative analysis of the liver cancer images. Additionally, it is possible to represent visual understanding of many radiologists in a particular CAD method. Application and selection of non-invasive medical imaging techniques using computer-aided methods requires sequential application of various medical image processing steps on these medical imaging techniques, CT and MRI [13].

Specifically, these image processing steps are the liver image enhancement (resulted with clear tumor intensity levels), liver cancer abnormal tumor portion detection and classification, segmentation, all the lesions segmentation of the CT and MR images and registration of the multi-phase CT images.

In order to design a CAD method for the diagnosis of Liver cancerous CT and MR images, it is necessary to first enhance liver cancerous images, extract the features, selection of features, and to classify them, with the segmentation of the liver cancer, and registration of multi-CT images Liver cancerous regions [10].

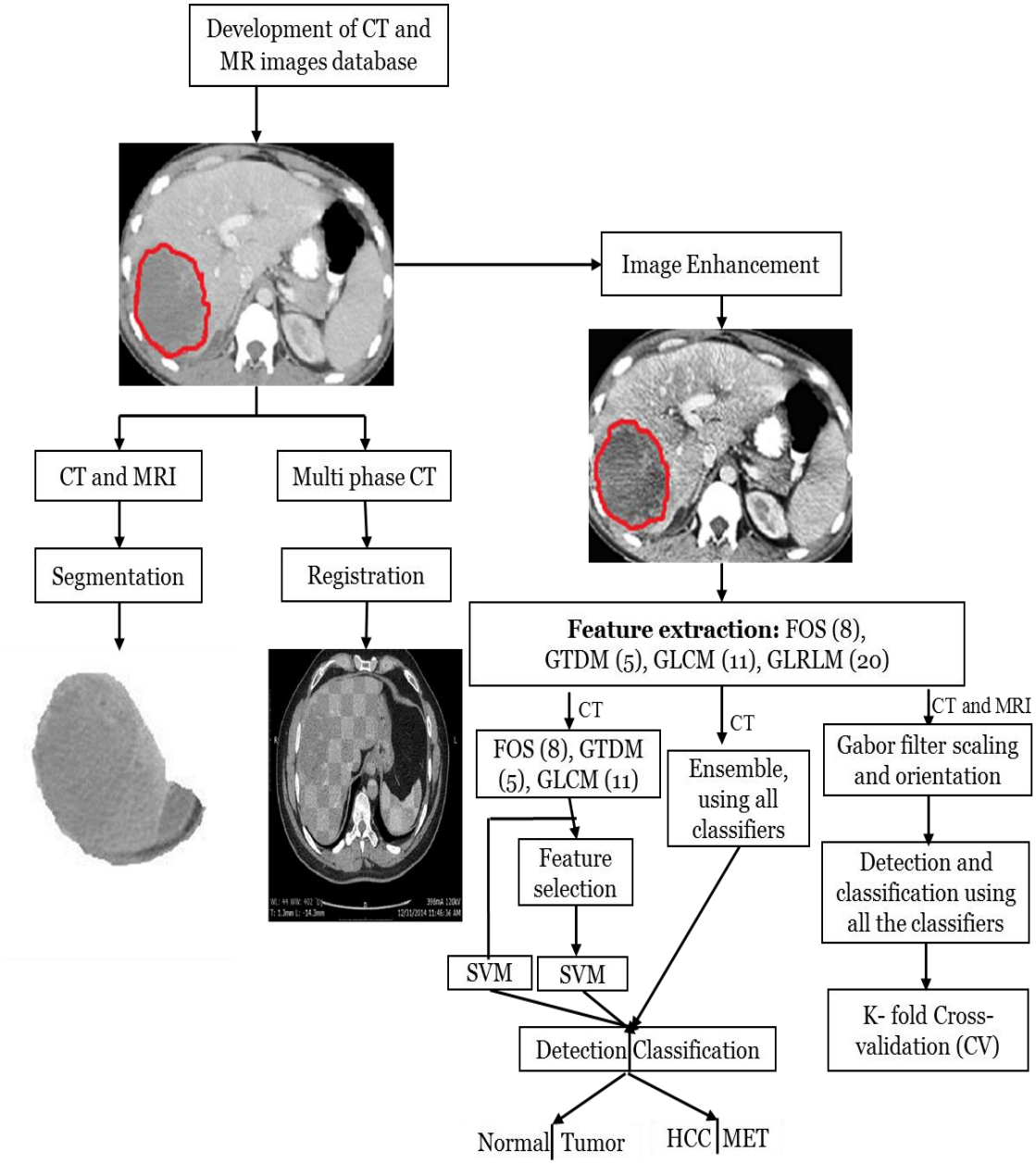

Figure 2.1: Flowchart of the experimental Methodology.

Figure 2.1 represents the complete work flowchart, the present work that has been done. For all the studies and the experiments that have done, from the input medical images to do the complete processing. Overall, the pre-processing, all the features extracted, classifiers, medical processing domains and the different experimentation details are provided [37].

In this chapter, the reviews of significant work done in the diagnosis of the liver cancers, liver tumor location and detection, their classifications, types of the lesions segmentation and the registration of the liver cancer, with different features extractions,

feature selections, types of the classifiers, involving various methods with different medical imaging techniques are provided.

2.2. DATABASE COLLECTION

The database plays a huge role in the designing of the CAD. It acts as the input images function for the CAD. It details is all about how to do an analysis with a particular class of non-invasive technique, that allows also to know the radiologist which particular non-invasive technique is preferable to get the detailed analysis of the internal organ of the body, to get their detailed imaging. There are several researchers' image details, which allows to know how they performed their work with the images as the input.

Chen *et. al.* (1998) worked on 30 enhanced liver images to design an automatic diagnostic system [16]. Gletsos *et. al.* (2001) worked with CT images on 147 ROI samples of normal liver, cysts, hemangioma (HEM) and HCC [17]. Valavanis *et. al.* (2007) worked on 97 ROI with CT images of normal liver, cysts, HEM and HCC [18]. Rajendran *et. al.* (2010) worked on 160 CT images [19]. Padma *et. al.* (2011) worked on 120 CT brain images [20]. Gunasundari *et. al.* (2012) worked on 70 CT images of HEM as benign and hepatoma as malignant [21]. Umamaheshwari *et. al.* (2012) worked on 150 CT images [22]. Leena (2015) worked on 50 CT brain tumor images [23]. Veeramuthu *et. al.* (2014) worked on 150 CT images [24]. Veeramuthu *et. al.* (2015) worked on 75 CT images [25]. Alahmer *et. al.* (2016) worked on 60 images of 33 malignant and 27 benign images [26]. Perumal *et. al.* (2018) worked on 100 images [27]. Ozyurt *et.al.* (2019) worked on 112 CT liver samples images of benign and malignant [28].

The above mentioned work doesn't have the detailed analysis of the images. These images are such type that don't have the details about the type of the diseases, and what type of organ it is. The images presented here are very less with the number of images. The present work is having a large number of images with the CT and MR images, with the details of all the experimentations that have what images have the input with what type of processing. There are also the large number of images, which allows to do the proper analysis with a better performance of the experiments.

2.3. CT IMAGE PROCESSING DETECTION AND CLASSIFICATION

Several researchers have been carried out work on the CT images on different parts of the body organ for the identification, detection and various types of classification of numerous types of diseases.

Several researchers only worked to classify the normal and abnormal classes, such as Chen *et. al.* (1998) worked on 30 enhanced liver images to design an automatic diagnostic system. They extracted the texture features from the liver images using Spatial Gray Level Co-occurrence Matrices (SGLCM) features. They used a Modified Probabilistic Neural Network (MPNN) classifier to classify the disease Hepatoma (HEP) and Hemangioma (HEM) [16]. Bhatnagar *et. al.* (2017) used HE to improve the quality of the images. They extracted the feature using GLCM and binarization to predict the normal/abnormal case. They used Principal Component Analysis (PCA) as the feature selector for better classification of images and classified using SVM, Neural Network (NN), and Naïve Bayes binarization type to determine the image is normal or abnormal [29].

Gletsos *et. al.* (2001) worked with CT images on 147 ROI samples of normal liver, cysts, HEM and HCC. They extracted 48 texture features using SGLCM, selected the features using a sequential forward floating method and classified using NN. They provide the classification with one class vs. rest other classes. They have not shown much improvement using the feature selection. They classified normal and abnormal, further classify cyst and other diseases and furthermore HEM and HCC using a NN [17].

Padma *et. al.* (2011) worked on 120 CT images. They used CLAHE to enhance the contrast of the brain images and hybrid mean filtering to improve the image quality. They extracted the features by Grey Level Run Length Matrix (GLRLM), wavelet co-occurrence texture and GLCM method. They used GA as a feature selector. They achieved 98.3% highest accuracy with GLRLM. They classified the Brain tumor using an SVM classifier with Wavelet-based features and SGLDM feature extraction that resulted in a better classifier rate in comparison to segmentation methods [20].

Leena (2015) worked on 50 CT brain tumor images. They used a bilateral filter for noise reduction and to remove artifacts. They extracted the features using texture descriptors, Radon transform and 1D Fourier transform of an image. They classified using the statistical classifier, SVM, and Hysteretic Hopfield NN (HHNN) and classified results in 98% with HHNN [23].

Punia *et. al.* (2013) used median filters to denoise the image with the image sharpening filter to enhance edge qualities. They extracted the features by six histogram features and 28 Wavelet Transform (WT) features. They selected the features using GA with 4 FOS and 9WT. They classified using the combination of NN and GA, achieved 96% highest accuracy. They worked on the automatic detection of the liver by evaluated FOS and WT [30]. They worked on the classification of liver and non-liver regions.

Many researchers also have worked on categorization into various liver image categories,

Valavanis *et. al.* (2007) worked on 147 ROI with CT images of normal liver, cysts, HEM and HCC. They extracted texture features using FOS, GLCM, laws texture energy measures, fractal dimension texture measurement. They applied GA on the individual feature methods, where the total number of features used more than 10. They classified using NN and performed one vs all criteria to classify. The Receiver Operating Characteristic (ROC) area curve for all, one-versus-all discriminations of hepatic tissue [18].

Gunasundari *et. al.* (2012) worked on 70 CT images of HEM as benign and HEP as malignant. They calculated the texture features by Fast Discrete Curvelet Transform (FDCT), GLCM, biorthogonal WT and classified by Back-Propagation Neural Network (BPNN), Probabilistic NN and Vascade feed-forward BPN. They used FDCT yields better results in all NN. They also used GLCM with BPN. They done a direct classification of the extracted features. Segmented the liver by histogram analyzer and segmented the lesion by Fuzzy C-Mean (FCM). Evaluated the texture features by FDCT, GLCM, and bi-orthogonal WT [21].

Ozyurt *et.al.* (2019) worked on 112 CT liver samples images of benign and malignant. They used a Convolutional Neural Network (CNN) classifier that converts from binary to logistic regression using accuracy and execution time. They used only the image size variation to calculate the classification accuracy. They classified using ANN, SVM, and CNN. CNN features achieve a better classification performance [28].

Alahmer *et. al.* (2016) worked on 60 images of 33 Malignant and 27 Benign images, divided the segmented lesions using FCM into inside, outside and border areas. They used SVM and 5-fold Cross-Validation (CV), confusion matrix to get the classification accuracy [26].

. Khachane (2015) worked on 100 CT images by evaluating the FOS and SD on the cut axial. Fuzzy rule-based system, SVM quadratic, RBF resulted in 88% accuracy with the

best results. They classified for segmentation purposes, not to classify that particular disease by k-NN, SVM and fuzzy rule-based system [31].

Rajendran *et. al.* (2010) worked on 160 CT images. The Median filter is used to find the edges of the tumor in the CT image and used a Hybrid Association Rule Classifier (HARC) with 95% accuracy. They only detected the edge using feature extraction [19].

Bhuvaneshwari *et. al.* (2014) worked on CT images lung disease to detect by features through moment invariants. Median filters are used to remove the salt and pepper noise. They selected the features using GA to select top-ranked 30 features and classified using decision tree classifier, 95% accuracy. They classified with only a particular class [32].

Umamaheshwari *et. al.* (2012) worked on 150 CT images of normal and abnormal images of the CT brain that evaluated the features using statistical image features, co-occurrence based textual features of images and classified by k-NN, sequential minimal optimization and SVM-Quadratic Program Optimization (QPO). The accuracy with SVM-QPO is 96.6%, result in best classifier results [22].

Veeramuthu *et. al.* (2014) worked on 150 CT images. They extracted the features by biorthogonal spline wavelet. They reduced the features using Association Rule Mining (ARM). KNN with ARM results in the best accuracy of 93.33% [24]. They didn't provide the class of the diseases of the image.

Veeramuthu *et. al.* (2015) worked on 75 CT images. They used a bilateral filter for noise reduction and to remove artifacts. They extracted the features using a discrete wavelet transform. They selected the features using PCA, with the best four features they classified using hybrid classifier results in 97.3% accuracy [25]. They didn't provide the class of the diseases of the image.

Perumal *et. al.* (2018) worked on 100 images, enhanced the images using CLAHE [19]. They extracted the features using five-level haar WT, predict cancer, analyses them and find pathological issues using Artificial Neural Network (ANN) [27]. They worked with only the detection of cancer and classify it.

Rajathi *et. al.* (2019) extracted the features by GLCM and Tamura for the ROIs. They selected the features using wrapper methods, WOA-SA hybrid enhanced the final solution and classified using SVM, k-NN and Random Forest (RF) to classify the liver diseases. The

95% confidence level yields the best result in terms of accuracy, sensitivity, and specificity [33]. They didn't provide the disease class of the image and the number of images. Table 2.1 summarizes the study of different CT images of tumors.

Table 2.1. Details of the classifier, Dataset and the ROI segmented region for the different images.

Authors	**Dataset and Pre processing**	**Feature extraction methods**	**Feature selection methods**	**Classifier(classification accuracy)**
Chen *et. al.* [1998]	30 Liver cases of hepatoma and hemageoma	Initial liver boundary detection Spatial gray level co-occurrence matrices	--	Modified Probabilistic neural network (95%)
Gletsos *et. al.* [2007]	147 ROI 76 normal 19 cyst 28 HEM 24 HCC	Spatial gray level co-occurrence matrices	Sequential forward floating selection	Neural network (97%)
Valavanis *et. al.* [2007]	97 ROI 38 normal 15 cyst 24 HEM 20 HCC	First order statistics Spatial gray level dependence matrix Gray level difference matrix Laws texture energy measures Fractal dimension texture measurement	Genetic algorithm	Neural network
Gunasundari *et. al.* [2012]	70 images 40 HEP 30 HEM Histogram analyzer	Morphological operations Fuzzy c-means Fast discrete curvelet transform Gray level co-occurrence matrix Biorthogonal Wavelet transform	--	Back propagation neural network (96%)
Punia *et. al.* [2013]	5x5 window size	First order histogram Wavelet transform	Genetic algorithm	Neural network (96%)
Rajathi *et. al.* [2018]	Square ROIs	Gray level co-occurrence matrix, Gray level curvature co-occurrence matrix, Gray level gradient co-occurrence matrix	Wrapper method	SVM, k-NN, RF 95% confidence level

Ye *et al.* (2009) worked on 131 multi-phase CT images, using 16 X 16 pixels ROIs, evaluated the features using FOS, SGLCM, and temporal features [34]. Zhang *et al.* (2011) worked on 12 normal cases and 25 abnormal cases to detect 44 cases of metastatic tumors

and a spherical gray level differentiation searching filter to detect the spherical shape of the tumor [35]. Stoitsis *et al.* (2006) extracted the ROI to evaluate the features: FOS, spatial gray level dependence matrix (SGLDM), gray level difference matrix (GLDM), texture energy measure (TEM), Fractal dimension measurement (FDM) [36]. Zhang *et al.* (2008) enhanced with contrast material, HCC with high and low-intensity regions in arterial, and equilibrium phase images. HCC extracted the areas without edges by Sobel and Laplace of Gaussian (LoG) the filters for edge detection [37]. Kayaalti *et al.* (2012) worked on liver fibrosis images to evaluate GLCM, Discrete Wavelet Transform (DWT), and Discrete Fourier Transform (DFT) [38]. Ali *et al.* (2015) worked on CT images of normal, Hepatoma, cyst, Cirrhosis to detect the tumor using FOS features [39].

Ye *et al.* (2009) classified using SVM to detect and classify the tumor [34]. Stoitsis *et al.* (2006) classified the normal, hepatic cyst, HEM, and HCC using a multi-layer perceptron neural network (MLPNN) [36]. Kayaalti *et al.* (2012) classified using k-NN and SVM [38]. Ali *et al.* (2015) classified by geometrical features [39]. Anthimopoulos *et al.* (2016) used the Conventional Neural Network (CNN) to classify 7 classes, including 6 different ILD patterns and healthy tissue [40]. Bogomasov *et al.* (2018) classified using a decision tree, RF, and linear regression, with RF as the best result with the RMSE and AUC measures [41].

Table 2.2. Details of the classifier, and the Dataset for the different classes of tumor images.

Authors	Image classes	Classifiers
Ye *et al.*	Normal, cyst, HCC, HEM	SVM
Rajendran *et al.*	Brain tumor	HARC, C4.5, Associate rule
Kayaalti *et al.*	Fibrosis	k-NN classifier, SVM
Gunasundari *et al.*	HEP, HEM	BPN, PPN, CFBPN, NN
Umamaheshwari *et al.*	Brain Normal, abnormal	k-NN, SMO, SVM-QPO, SVM-APO
Bhuvaneshwari *et al.*	Lung disease	Decision tree, Naive Bayes
Khachance	Brain tumor	SVM, k-NN, Fuzzy rule base
Leena	Brain tumor	Statistical classifier, SVM, HHNN
Veeramuthu *et al.*	Brain tumor	k-NN, SVM, Hybrid
Ali *et al.*	Normal, HEP, cyst,	Geometrical features

	Cirrhosis	
Alahmer *et al.*	Malignant, Benign	SVM, 5-fold CV
Rajathi *et al.*	Normal liver, Fatty liver, Metastases, Cirrhosis	SVM, k-NN, RF
Anthimopoulos *et al.*	Lung interstitial diseases	CNN
Bogomasov *et al.*	Lung Tuberculosis	Decision tree, RF, linear regression
Ozyurt *et al.*	Malignant, Benign	ANN, SVM, CNN
Bhatnagar *et al.*	Normal, Abnormal	SVM, NN, Naive Bayes

2.4. GABOR FILTERS

The Gabor filter parameters work for the texture classification accuracy: the highest frequency as the center frequency of the filter (F_M), the total number of frequencies (n_F) and the number of orientations (n_O). Gabor wavelet implements rotation invariant texture, feature extraction for texture classification and texture segment. Extracting texture features, Gabor wavelet with pre-defined scale set and orientations, extracting time-frequency coefficients from each scale and each direction. Gabor wavelets also attain maximum joint space-frequency resolution in the process of texture extraction for texture representation and texture spatial localization. Gabor filters have a higher potential to separate tumor regions. Several researchers have been worked out to evaluate the Gabor filter parameters scaling and orientation parameters, designing various combinations to extract the features and classify them.

Yu *et al.* (2011) designed a local spectral with optimal properties regarding the time-frequency certainty principle, that modified the original Gabor filter, the skew Gabor filter to correct skewness for the filter response as the sum of Gaussians model in the mid-frequency space [42]. Sadeghi *et al.* (2016) applied Gabor wavelet to detect defection on steel sheets, a fast and highly accurate approach to detect these defects results in highly accurate correct detection [43]. Sahoolizadeh *et al.* (2008) used Gabor wavelets for facial recognition and identification. Gabor wavelet faces combined with an extended neural network (NN) feature space classifier [44]. Vyas *et al.* (2006) filtered the image using Gabor filters in the domain of the spatial frequency [45]. Gabor feature vectors used as input to a classification or transformed into new feature vectors. A texture pair gave the optimal Gabor filter. Arca *et al.*

(2006) applied Gabor filters, varying the orientations and the frequency/scales to measure the similarity between the images, on a smaller set of points [46]. Thiang *et al.* (2003) extracted the features using Gabor filters, convolved the filter kernel with the image [47].

P. Monero *et al.* [2005] estimated the local image neighborhood using Gabor features. Gabor functions as the low-level oriented edge and texture discriminators, that sensitive to different frequencies and scales. The effects of Gabor response vary to rotated patterns on the detector rate [48]. Sabri *et al.* (2004) worked on kernel function using Gabor filter decomposition, linear predictive coding (LPC) in sub-bands of Gabor filter banks to extract an efficient set of features [49]. SVMs generalized in high dimensional spaces. Fasel *et al.* (2002) compared the various Gabor filter methods for facial landmarks automatic detection [50]. The best performance concentrated using large orientations (8) on very-low-frequency carriers. Clause *et al.* (2003) combined the robust and reliable features, Gabor filters with a matched frequency convolved with each signal and the magnitude response determined, and then weighted using the feature contrast method by k-means clustering segmentation [51]. Chen *et al.* (2004) extracted the features for image retrieval, the scale of six and orientations of four (number of filters: 24), better resulted when all the images are taken [52]. Ahmadian *et al.* (2004) classify by Gabor wavelet. Gabor parameters, the scales numbers and the number of orientations different values [53]. The highest frequency set as a driving parameter fixing.

S. Monti *et al.* (2014) used a Gabor filter bank to extract the motion information with the grip parameters for the group of images [54]. The final filter output is a voxel-based interpolation. The optimal tag spacing should be a compromise between the smallest tag periods achievable in a real acquisition. R. Rajagopal *et al.* (2014) acquired images in spatial domain mode [55]. Morphological operations performed over a segmented binary image to refine rough segmentation results using an SVM classifier. S. Echegaray *et al.* (2015) described the intensity, texture, shape, and margin for the segmented lesion [56]. The Intensity feature used ROI pixel values. Margin features characterized the margin of the lesion, a manually selected subset of the imaged tumor. Z. Li *et al.* (2017) used a Gabor transform feature to reflect the spatial relationship of the image on a different scale and frequency domain [57]. Texture analysis quantized the arrangement of tumor cells with different pathological types. R. Patil *et al.* (2017) surveyed CAD using feature extraction and classification [58]. Accuracy improved with texture analysis and its result improved by

various combinations. R. Pasternack *et al.* (2010) worked on Gabor a filtered image, and every adjacent pixel region averaged into one pixel before orientation processing, de-magnified the filtered images [59]. Differential response to the Gabor filters characterized the morphometric features with different dimensions and orientations. S. Parvathy *et al.* (2010) characterized using moment invariant features to translation, size and rotation, able to compute moments from a point shifted to a distance from the image centroid, at any rotation of any size [60]. S. Mohammad *et al.* (2003) distributed the bank of Gabor filters the entire frequency to mimic the HVS for prostate texture segmentation [61]. Pixels from the same texture region have the same characteristics. Multi-channel filtering captured key texture information through a separate channel. S. Rana *et al.* (2016) computed the Gabor feature from the ROI [62]. Gabor wavelet transform feature classified the tissue and captured the textual variations, works for two-class characterization. R. Pasternack *et al.* (2010) used 2-D Gabor simple Fourier filter functions tuned for size and orientation [63]. Gabor filter response maximized when the scatters diameter is the same as the half Gabor filter period. R. Rajagopal *et al.* (2015) surveyed on various tumor detection and methodology for diagnosis [64]. Gabor wavelet for multi-resolution images for frequency v/s time. Binary image extracted the region shape as the image components to yield better segmentation accuracy.

The filtered image using Gabor filters has different orientations and spatial frequencies set for the spatial frequency domain, and the features vector field and further analysis, classification or segmentation applications [65]. The parameters of the Gabor function are specified using the frequency, the sinusoid orientation and the scale having Gaussian function. In filter design approaches, only a few filters are designed to reduce the filter bank approaches difficulties for a particular application. The selection of best filters by the textual properties derived from a spectral Fourier analysis for a particular image. The mostly signified and the preferred frequencies and orientations of the Gabor filters [66, 67].

The above described work, has been evaluated for a particular classes according to a category. Gabor filters with maximum of eight orientations and four scales/wavelengths. More scale/wavelength of Gabor filter, the more significant recognition rate. The present work is with the eight orientations and five scales using the Gabor filters. The CT and MR images both have a Gaussian function, that's results an appropriate result with Gabor filter parameters. There are a classes of experiments that allows' to do the analysis with the CT images, MR images and their combinations. There are various classifiers and performance

evaluations, which are more in the number to do the analysis and extracting the better results. These performance allows to detect the tumor, classify the tumor, comment on the level of the tumor, that's' allow to assist the radiologist as a second opinion prior to do the diagnosis.

2.5. SEGMENTATION

The segmentation is carried out to several research work with the segmentation of the medical tumor images. This segmentation is done to divide an image to separate out the tumor portion, boundaries of the tumor, classes of the tumor levels. It matters also with the type of the medical imaging techniques. There are less methods, algorithms involvement to do the complete segmentation techniques. The segmentation parts allowed to detect and interpret the tumor region present in an image. There are various researchers segmentation work described below.

Bereciartua *et al.* (2016) evaluated the minimization of a 3D active surface using multichannel MRI automatic liver segmentation. The 3D surface methodology normally coordinates volumetric regularization in the factual model, advanced over a probability map dependent on a new compact descriptor comprising spatial and multi-grouping data. The upsides of the compact visual descriptor together with their exhibited methodology result in a quick and precise 3D segmentation strategy. The method tested on 18 healthy liver examinations and results contrasted with the best quality level determined. The obtained outcomes improved those systems, with a dice similarity coefficient of 98.59 [68].

Chartrand *et al.* (2017) experimented a semi-automated segmentation method for the liver and calculated the performance on the CT and MR images. An approximate 3D model of the liver initialized from a few user-created contours to globally outline the liver shape. Their model automatically deformed by a Laplacian mesh optimization scheme until it precisely delineated the patient's liver. A correction tool simplified to allow the user to enhance the segmentation. The outcome tested with 30 CT scans and 20 MR studies, covering a wide spectrum of liver morphologies and pathologies. The average volumetric overlap error 5.1% for CT and 7.6% for MRI and the average segmentation time 6 min. the result of the method efficient, reliable and efficiently used in the clinical setting [69].

Lopez-Mir *et al.* (2014) worked on a liver segmentation based on the watershed transform and stochastic patterns. The over-segmentation of classical watershed was minimized by applying a marker controlled algorithm. To enhance the exactness of explicit

forms, the gradient of the original picture effectively improved by utilizing another variation of the stochastic watershed. Besides, the last classifier was performed to accomplish the final liver mask. Ideal parameters of the technique tuned utilizing a training data set connected to the rest of studies [70].

Swierczynski *et al.* (2018) experimented an image registration and segmentation approach, created a new scientific definition to mutually segment and register 3D lung CT volumes, which based on a level-set detailing, consolidated a great Chan-Vese segmentation with the active thick displacement field estimation. Combining registration with segmentation had two key points, wipe out the issues of introducing surface based segmentation strategies and to fuse earlier learning into the registration [71].

Huang *et al.* (2018) experimented a fully automatic procedure by applying modified graph cuts and feature detection for precise and quick liver segmentation. The initial slice and seeds of the graph cuts automatically determined by utilizing an intensity based strategy with prior position data. They additionally exhibited a local organ across multi-slices based on the similarities and differences of contrast to improve the weak boundaries of soft organs and to prevent over-segmentation. The vessel anatomical data based on a feature detection method [72].

Anter and Hassenian (2018) designed an improved segmentation approach for stomach CT liver tumor based on neutrosophic sets (NS), particle swarm optimization (PSO), and fast fuzzy c-mean algorithm (FFCM). To improve the contrast, the intensity values and the high frequencies of the original images erased and balance initially utilizing the median filter approach. It followed by changing the stomach CT image to NS space. The entropy utilized to ascertain indeterminacy in NS space. The NS image passed to optimize FFCM utilizing PSO to improve and upgrade cluster results and segment liver from stomach CT. these segmented livers passed for PSO-fuzzy C-means (PSOFCM) procedure to cluster and section the tumors [73].

Masoumi *et al.* (2012) designed a new automatic system for liver segmentation in abdominal MRI images. Pre-processing to improve the image by edge preserved noise reduction, using MLP neural networks and watershed algorithm. They used trained neural networks to extract features of the liver region. The extracted features used to monitor the quality of the segmentation using watershed transform and adjust them [74].

Table 2.3. Details of the segmentation results, their data and feature extraction methods.

Authors	Dataset and Pre processing	Feature extraction methods	Result
Bereciartua *et. al.* [2016]	18 Healthy liver MRI	Volumetric regularization factual model	Dice similarity coefficient
Chartrand *et. al.* [2017]	30 CT and 20 MRI	Laplacian mesh optimization	Slice wise segmentation
Lopez-Mir et. al. [2014]	MRI	Watershed transform, stochastic patterns	Jaccard coefficient
Swierczynski et. al. [2018]	3D lung CT volume	Chan Vese segmentation	Surface based segmentation
Anter Hassenian [2018]	CT liver tumor, Median filter	PSO-fuzzy C-means	Upgrade cluster and section the tumors.
Masoumi et. al. [2012]	Abdominal MRI liver, edge preserved noise reduction	Watershed algorithm, Neural networks	Boundary tracking algorithm, extract the liver region

The above described work is the work done with the medical images to do the segmentation, that doesn't allow to do the segmentation work by the classification and the segmentation. The present classification work allows to classify by the normal liver or the tumor. The segmentation work allows to segment the tumor portion separately. The feature extraction is done by using GLCM. The above described work doesn't have the feature selection work in segmentation. The present work feature selection is by using OFOA. The feature selection work allows to do classification using ANN classifier. The further classification on the tumor is done by using MKKC algorithm, to interpret the tumor levels present in the image.

2.6. REGISTRATION

Several researchers have been worked with the image registration algorithm to get mutual information (MI) from the images. The registration maybe of feature based registration and intensity based registration. Feature based registration minimizes an objective function based on image features. Intensity based registration have a difference in the intensity of the segmented images. Registration algorithm have a strong correlation between the images that are used as the input images, that helps in co-locate areas of interest with the registered images.

S. Klein *et al.* (2010) worked with a toolbox to configures, test, and compares different registrations using intensity-based registration for a specific application that

supports the use of all voxels (pixels of 3-D images), voxels subset on a uniform grid, random sampling of voxels, and random sampling of the voxel grid [75]. C.V. Stewart *et al.* (2010) worked on a registration algorithm that registers retinal image pairs, initially automatic matching with vascular landmarks, aligned images used by detected blood vessel centerlines [76]. A. Roche *et al.* (2004) developed the general maximum likelihood problem [77]. The rigid registration of several images to know about the importance of the similarity measures appropriately. X. Huang *et al.* (2009) determined the registration accuracy by calculating the desired parameter, the rms distance of the two sets on the homologous points measured with all the phases [78]. The registration transformation is visualized. M. N. Aktar *et al.* (2014) provided a robust rigid registration using similarity measures with the CT to volume MRI [79]. The rigid body transformation is done to use three translations and three rotations parameters. F. Alam *et al.* (2019) designed automatic detection of registration of sub-regions with local features and the entire image using global parameters [80]. W. Cao *et al.* (2018) developed a multimodal medical image registration using features [81]. With the features detection, an algorithm to construct the feature sphere in conformal geometric algebra that register the images with the correspondence parts of the images.

The above described work is all about to design a class of toolbox, and to determine some classes of the parameters. There are various algorithms that allows to do the registration process and evaluating various types of the functions. These work don't provide the details about the particular phase details linked with the registration. The present work is having the phase details linked with the registration. The two phases registration have the output registered image to get the MI among them. The phases act as the input images allows the benefit for the radiologist to get the detailed information that linked with the phases. Further, a detailed phase allows to take such type of useful information about the organ, and to get those type of phases as the other patients' data. These phases allow to get the further information for the patients' about the detailed analysis about the patient.

2.7 CONCLUDING REMARKS

Based on the critical review of the literature, the following conclusions have been drawn:

(i) Literature related to the database collection indicates that different classes of data used for the image processing work in the medical domain. The work done is to determine the cancerous area or non-cancerous area, a different class/ category for the tumor, the organ or non-organ region of the image, using a less number of images using as the

input image with not properly defined type of non-invasive technique. The connectivity with the organ details and with the type of cancer not preserved in most of these approaches. Thus, in the present work, this problem is overcome related to the large number of the images, with a proper class of a disease, proper category of the liver cancer diseases classification and how to interpret the levels in the tumor present in the liver region taken care of.

(ii) A comprehensive literature survey on the medical image processing work that the feature extraction based methods are best suitable for the liver diseases cancerous detection. The efficiency of the tumor detection is improved in the present work by extracting a large number of features and using multi-classifiers on a large database. The detection have an excellent classifier rate, the input for the feature extraction is an enhanced images, using suitable algorithm, clear difference of the intensity level among the normal and abnormal tumor images.

(iii) A comprehensive literature survey on the medical image processing work for the classification of the type of liver cancer diseases, in their respective category. The efficiency of the tumor classification is improved in the present work by extracting a large number of features, multi-classifiers and designing various experimentations on a large database. The detection have a consistent classifier rate using all the classifiers. The large database classification results yield a better classifier rate to classify the liver cancer categories. The liver cancer categorized allows to get the information regarding a type of tumor class to interpret the tumor level.

(iv) Medical image segmentation methods (designed for the detection of tumor and interpret their levels) allows to get a proper tumor portion and divided into some suitable portions as to be useful. It was also observed after literature review the segmentation worked out on the less number of images, boundaries of the segmented regions blur, anatomical data based on feature detection method, diverse image content, clustered objects, and non-uniform object texture. Therefore in the present work, to increase accuracy of the segmentation using CT and MRI on various liver images, a large database effectively to be done using OKK-means clustering. The abnormal portion from the original images separated out by suitable clustering algorithm. The performance is analyzed with normal and abnormal images of various persons.

(v) Extensive literature available on the registration methods indicates that geometrical and morphological features are common in providing the image registration work. The

literature review is related to the registration work with the connectivity of the different medical imaging techniques, rotation, and translation processing, detection, and matching with the calculation of various feature parameters. The present work is Feature based registration, which allows to get the useful information in the combination of two images for the multi-phase CT images. There are different output combinations of the same registered image and some post processing work to improve the registration quality for a different classes of the multi-phase CT images.

(vi) Presently, most of the methods available in literature use less number of images, which are not sufficient with no proper details of the organ, and the diseases details about the images to develop and test computer-aided diagnostic methods. Therefore, evaluation of detection and classification methods on such databases is not justified. Although few researchers have combined various databases to classify the tumor classes, but still clinically acquired images which are encountered by radiologists in day to day practice should also be the part of the database. Therefore, in order to maintain a proper liver cancerous images category with respect to type of tumors, field of view, number of patients, machine settings etc., a composite database comprising of both clinically acquired liver cancer tumor classes is considered in the present work. Also, the evaluation to classify the category of the liver cancerous category, some methods on a large composite database would ensure their generalization capability. A large amount of database, to detect the tumor, to classify the tumor, to interpret the tumor levels, to get the useful information in combination of images and to combine different medical image domain classes experiment to yield the useful information.

Chapter 3

METHODOLOGY

3.1. INTRODUCTION

The data set comprises the images of the patients, which were acquired directly from the hospitals. The data collection includes both normal and abnormal liver data (cancerous liver). The gathered data images are examined using the Radiant DICOM viewer software. This software offers the capability of converting DICOM images to a number of different image formats. The data collection includes CT and MR images for all disease classes (HCC and MET) as well as normal liver. Figure 3.1 (a) and (b) shows the CT and MR images of the liver, respectively.

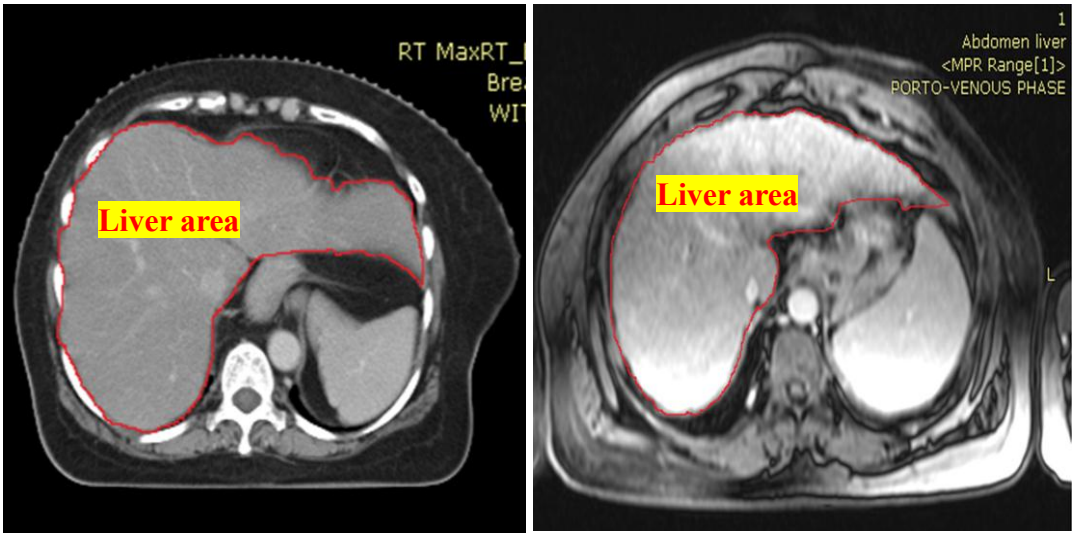

(a) (b)

Figure 3.1: (a) and (b) Liver images of CT and MR, respectively.

The total number of CT images, used in this thesis is 1638, out of which 794 normal liver images collected from 15 patients, 361 images of HCC collected from 4 patients and 483 images of MET collected from 16 patients. The total number of MR images used in this thesis is 3387, out of which 2274 images of normal liver collected from 5 patients, 600 images of HCC collected from 6 patients and 513 images of MET from 9 patients. The data collection is done for both the male and female patients, for different age groups. Figure 3.2: (a), (b) and (c) show the CT scan images of the liver with marked ROI for the HCC, MET and the normal, respectively. The region marked is the tumor portion that is present inside the liver. For the normal liver, the marked area is the complete liver portion of the body. Figure 3.3: (a), (b) and (c) show the MRI scan images of the liver with marked ROI for the HCC, MET and the normal, respectively. The region marked is the tumor portion

that is present inside the liver. For the normal liver, the marked area is the complete liver portion of the body.

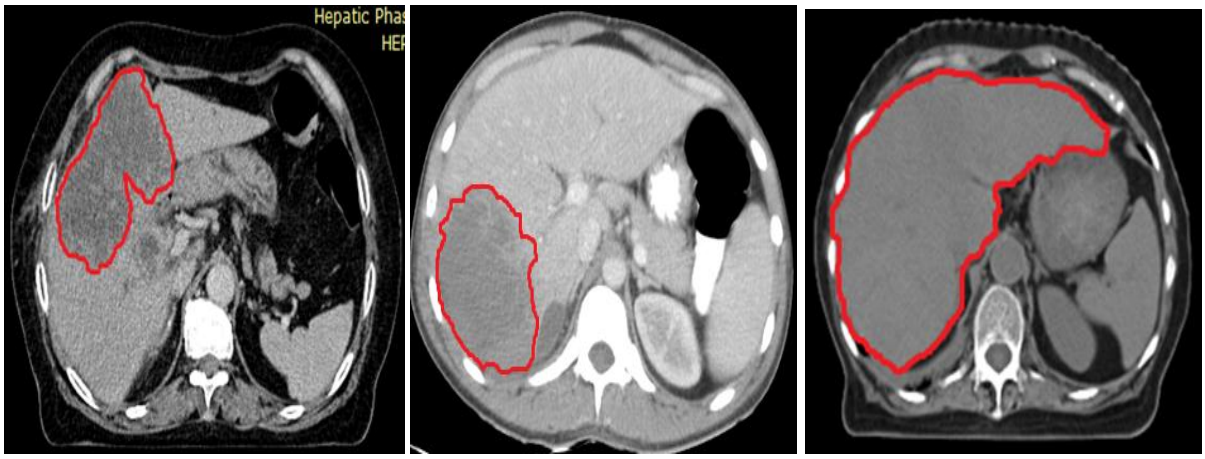

(a) HCC **(b) MET** **(c) Normal liver**

Figure 3.2: (a), (b) and (c) are the Marked ROI for the HCC, MET and the normal CT scan images of the liver, respectively. The region marked is the tumor portion that is present inside the liver. For the normal liver, the marked area is the complete liver portion of the body.

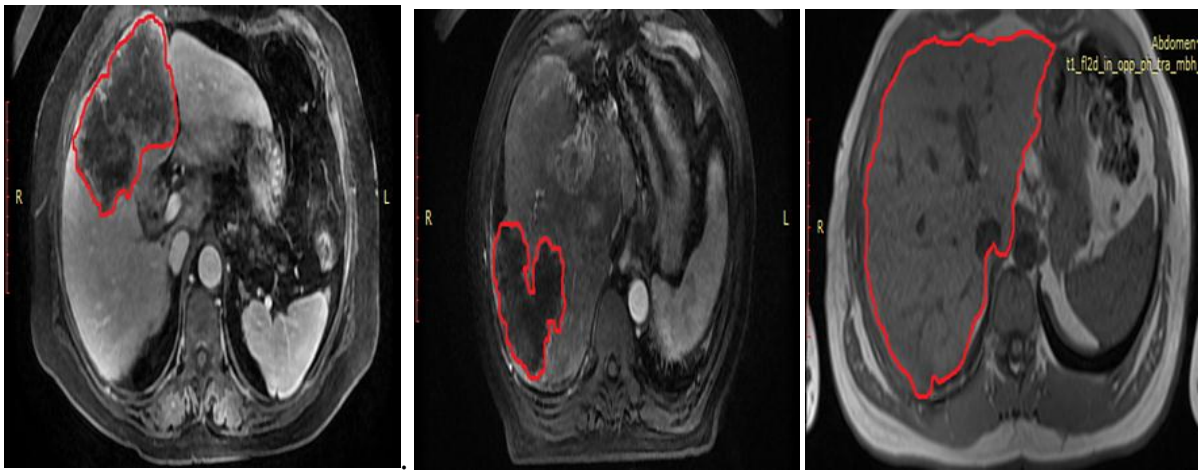

(a) HCC **(b) MET** **(c) Normal liver**

Figure 3.3: (a), (b) and (c) are the marked ROI for the HCC, MET and the normal MRI scan images of the liver, respectively. The region marked is the tumor portion that is present inside the liver. For the normal liver, the marked area is the complete liver portion of the body.

3.2. PRE-PROCESSING

The collected patient data from the hospital is in the form of DICOM images. The DICOM images are converted to the other formats to do the image processing work with the help of Radiant DICOM. The pre-processing of the image is a way to remove the noise of the image and get a better quality of image for visualization.

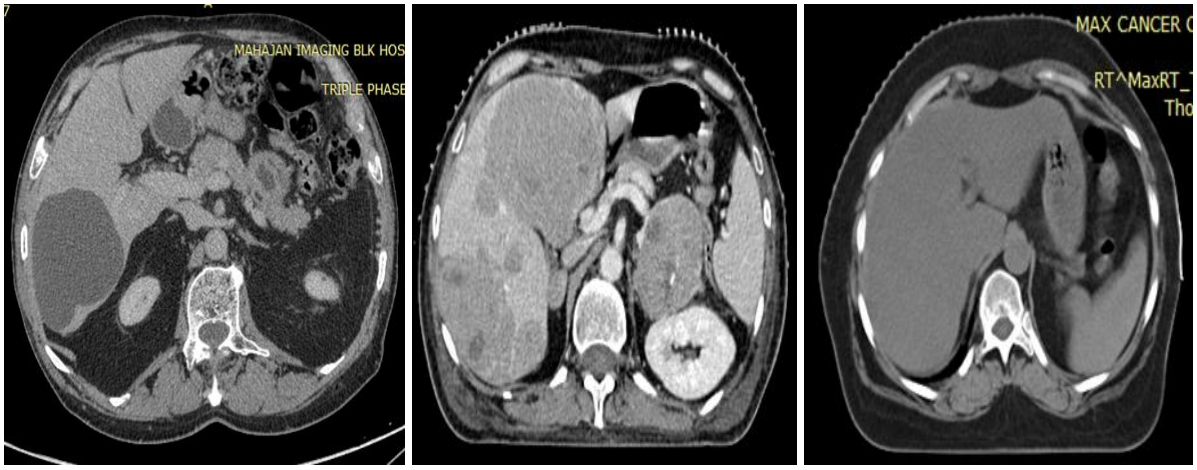

Figure 3.4: (a), (b) and (c) Original raw images of the HCC, MET and the normal liver CT scan images, respectively.

The image is firstly enhanced using suitable algorithms such as contrast limited adaptive histogram equalization (CLAHE) and constrained variable histogram equalization (CVHE). The enhancement improves the overall visual quality of the image.

3.2.1. Contrast Limited Adaptive Histogram Equalization (CLAHE)

CLAHE operate on a particular region in the image, each region is enhanced. It implements the histogram equalization (HE) to that area. HE is the processing of enhancement for low contrast type of images. Those regions have HE their surroundings regions matches their HE. The artificially induced boundaries between these regions are eliminated by using bilinear interpolation. CLAHE have robustness, reliability and flexibility in the CT image processing [82, 83]. The CLAHE enhanced images are the output images after the enhancement or pre-processing. Figure 3.4 (a), (b) and (c) shows the CLAHE enhanced CT images of the HCC, MET and the normal liver, respectively. The CLAHE enhanced images have better tumor portion visualization for further processing.

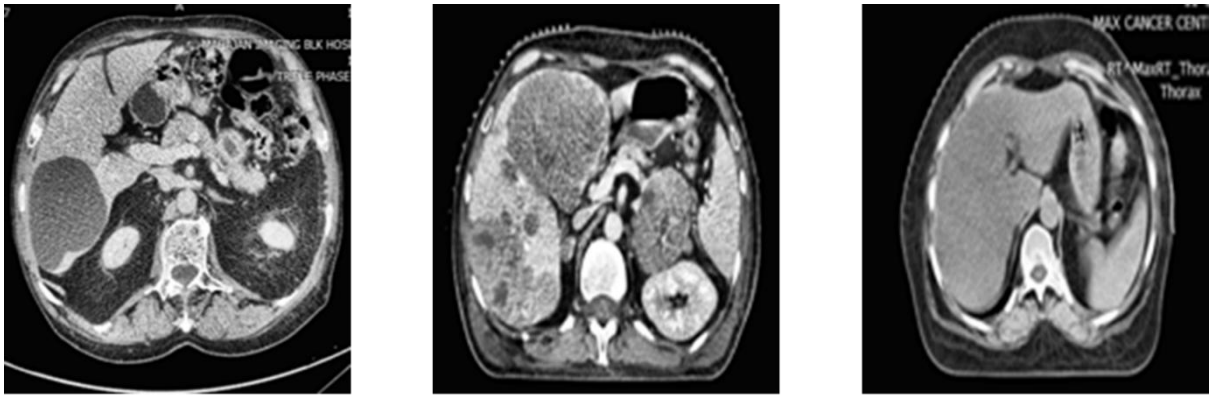

Figure 3.5: (a), (b) and (c) CLAHE enhanced images of the HCC, MET and the normal liver CT scan images, respectively.

3.2.2. Constrained Variable Histogram Equalization (CVHE)

The CVHE algorithm combines the advantages of the histogram equalization algorithm in contrast enhancement for gray level images with the preservation the global outlook of the image, extension of the variation definition of the histogram equalization by adding a constraint that would make the average brightness of the processed image as close to that of original image as close as possible [84]. This algorithm preserves the appearance of the original image and reducing saturation and over-enhancement artifacts. Figure 3.5 (a), (b) and (c) shows the CVHE enhanced CT images of the HCC, MET and the normal liver, respectively.

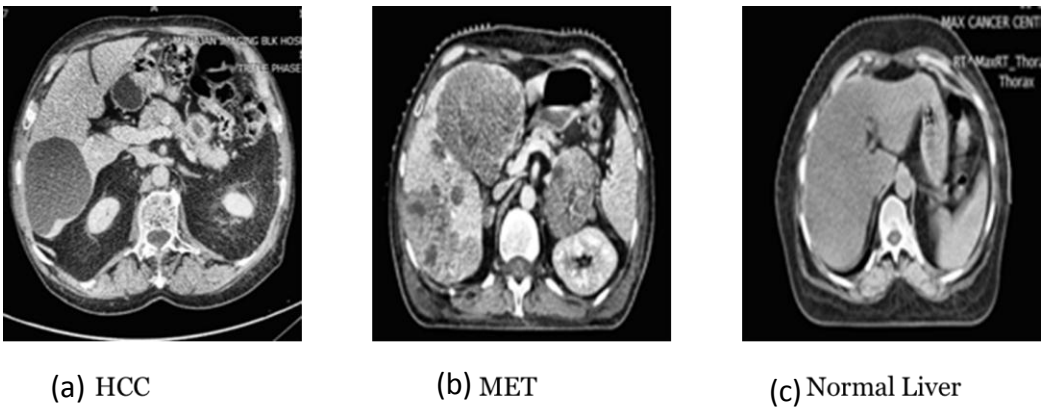

Figure 3.6: (a), (b) and (c) are the CVHE enhanced images of the HCC, MET and the normal liver CT scan images, respectively.

In all these enhanced images, the ROI is extracted of either size of 30 X 30 pixels or 25 X 20 pixels, depends upon the size of the tumor. The tumor portions that having such size in continuation, that size portion is cropped. These ROIs (30 X 30 pixels and 25 X 20 pixels)

use to calculate the various types of textural features in various experimentations. This size work efficiently in determines the number of appropriate IROI. The boundary part of the tumor is not the part of ROI.

3.3. Experimentation

STUDY 1: The 300 IROI images feature values and ratios of IROI and SROI for both HCC and MET is calculated with all the input CT images. 30 X 30 pixels, is chosen for the calculation of all the feature values for each image, for both the IROI and the SROI. IROIs values and the calculated ratio between the IROI and SROI values are considered as feature vector (FV) [85]. These FV were further classified by FOS, GTDM and GLCM as a feature class (FC) for both the types of diseases [38]. Further, GA was used for the feature selection, the feature were rank according to their weights. SVM used as the classifier to classify the group of diseases.

STUDY 2: The inputs are selected from 1638 number of CT images consisting of normal liver and abnormal liver, for which FOS, GTDM, GLRLM, and GLCM are calculated. The ROI is 25 X 20 pixels. The various classifiers used for classifications are R-part decision tree, AdaBoost, RF, k-SVM, GLM, and NN. The ensemble model is designed to improve the classification rate by using a combination of all the six classifiers.

STUDY 3: The various experiments have been designed in a particular way, to detect the tumor present as cancer in CT images, MR images, and combinations of both of them. The ROI is 25 X 20 pixels. The experiments to classify the type of tumor present in the CT images and the MR images. The experiments worked out are described here:

3.4. Feature Extraction

3.4.1. Gray Level Co-occurrence Matrix (GLCM)

GLCM is a statistical technique that designs the co-occurrence matrix to reflect the spatial distribution of the gray levels in the image [86]. It is a statistical technique that designs the co-occurrence matrix to reflect the spatial distribution of the gray levels in the image. Twenty GLCM features are calculated, that are auto-correlation, contrast, correlation, cluster prominence, cluster shade, dissimilarity, energy , entropy, homogeneity, maximum probability, variance, sum average, sum variance, sum entropy, difference variance, difference entropy, information measure of correlation-1, information measure of correlation-

2, inverse difference normalized and inverse difference moment normalized. The notations used in this sub-section are mentioned in Table 3.1.

Table 3.1: GLCM symbols

Symbol	Meaning
P(k)	First-order histogram
k	Corresponding histogram
i ,j	Pixel values
μ	Mean
m	Number of clusters
SAvg	Sum averages of the SGLDM
P_{ij}	Second-order joint probability of the intensity values of the two pixels (*i* and *j*)
N_g	Number of possible gray levels

Autocorrelation is to measure the fineness and coarseness of texture magnitude. Contrast is the local intensity variation measure.

$$Autocorr=\sum_{i=1}^{N_g}\sum_{j=1}^{N_g}(ij)P_{ij} \quad (3.1)$$

Correlation is the linear dependency of gray level values. Cluster Prominence is the skewness and asymmetry measure.

$$Cor=\frac{1}{\sigma_x\sigma_y}\left(\sum_{i=1}^{N_g}\sum_{j=1}^{N_g} ijP_{ij} - \mu_x\mu_y\right) \quad (3.2)$$

Cluster Shade is the skewness and uniformity measure.

$$CShad=\sum_{i=1}^{N_g}\sum_{j=1}^{N_g}(i+j-2\mu)^m P_{ij} \quad (3.3)$$

Energy (Angular Second Moment) is the homogeneity measurement of an image. The image has homogeneity with less discrete gray levels.

$$Homo=\sum_{i=1}^{N_g}\sum_{j=1}^{N_g}\frac{1}{1+(i-j)^2}P_{ij} \quad (3.4)$$

Entropy indicates the uncertainty, measures the average amount of information required to encode the image values.

$$Ent = -\sum_{i=1}^{N_g}\sum_{j=1}^{N_g} P_{ij}\ log\ P_{ij} \quad (3.5)$$

Variance is the dispersion of the parameter values around the mean of the combinations of reference and neighborhood pixels, with values farther from the mean weighted higher.

$$\sigma^2=\sum_{k=1}^{N_g} P(k)(k-\mu)^2 \quad (3.6)$$

Sum Variances are the Weights elements that differ from the average value of the GLCM.

$$SVar=\sum_{k=2}^{N_g}(i-SAvg)^2 P_{x+y}(k) \quad (3.7)$$

Inverse Difference Moment Normalized (IDMN) is a measure of the local homogeneity of an image. IDMN normalizes the square of the difference between values by dividing over the square of the total number of discrete values.

$$IDMN=\sum_{i=1}^{N_g}\sum_{j=1}^{N_g}\frac{1}{\frac{1+(i-j)^2}{N_g}}P_{ij} \quad (3.8)$$

Inverse Difference Normalized (IDN) also local homogeneity measurement that normalizes the difference between the values by dividing over the total number of discrete values.

$$IDN=\sum_{i=1}^{N_g}\sum_{j=1}^{N_g}\frac{1}{\frac{1+(i-j)^2}{N_g*N_g}}P_{ij} \quad (3.9)$$

3.4.2. Gray Tone Difference Matrix (GTDM)

Five GTDM features are calculated, namely busyness, complexity, strength, contrast, coarseness in work [85, 87]. GTDM are the features related to the human perception of the texture, a column matrix formed by summing the absolute value of the pixel being observed minus the average of the pixels in its neighborhood. The notations used in this sub-section are illustrated in Table 3.2.

Table 3.2: GTDM symbols

Symbol	Meaning
i, j	Image intensity levels
$S(i)$	i^{th} entry of GTDM
p_i, p_j	The intensity level i, j occurrence estimated the probability
G	Number of Elements
ε	The small number to prevent the coarseness coefficient from becoming

	infinite

Busyness is a busy texture, with rapid intensity change from a particular pixel to its neighbor, with very high-intensity change spatial frequency. It is described by the high spatial frequency of intensity changes.

$$Busyness = \frac{\sum_{i=0}^{G-1} p_i s(i)}{\sum_{i=0}^{G-1}\sum_{j=0}^{G-1}|ip_i - jp_j|}, p_i \neq 0, p_j \neq 0 \qquad (3.10)$$

Complexity is the texture content visual information, if that is high then complexity.

$$Complexity = \sum_{i=0}^{G-1}\sum_{j=0}^{G-1} \frac{|i-1|}{n(p_i+p_j)}[p_i + p_j], p_i \neq 0, p_j \neq 0 \qquad (3.11)$$

Strength integrates the concept of busyness and coarseness and summarizes them. A strong texture image has easily definable elements. Strength is more when primitives are easily definable and visible.

$$Strength = \frac{\sum_{i=0}^{G-1}\sum_{j=0}^{G-1}(p_i+p_j)(i-j)^2}{\varepsilon+\sum_{i=0}^{G-1} s(i)} \qquad (3.12)$$

Contrast is of a high level if different gray levels are visible, the intensity difference between neighboring pixels is very high. Coarseness has large values where the gray level differences are high.

$$Coarseness = (\varepsilon+\sum_{i=0}^{G-1} p_i s(i))^{-1} \qquad (3.13)$$

3.4.3. First Order Statistics (FOS)

Eight FOS features are calculated, that are Mean, Variance, Median, Mode, Skewness, Kurtosis, Energy, and Entropy, which describes the gray level histogram of an image [85]. The notations used in this subsection are illustrated in Table 3.3.

Table 3.3: FOS symbols

Symbol	Meaning
P(k)	First-order histogram
k	Corresponding histogram
P_{ij}	Intensity values of the two pixels (*i* and *j*), the joint probability of second-order

N_g	Number of possible gray levels

Mean (μ) reveals the general type of brightness for the image. Higher the value of the mean brighter is the image.

$$\mu = \sum_{k=1}^{N_g} k\, P(k) \tag{3.14}$$

Variance (σ^2) reveals the contrast for the image. High variance is an indication of good contrast.

$$\sigma^2 = \sum_{k=1}^{N_g} P(k)(k-\mu)^2 \tag{3.15}$$

Skewness (μ_3) is the asymmetry of the gray level distribution in the image. Energy measurement is directly related to skew.

$$\textit{Skewness, } \mu_3 = \sigma^{-3}\sum_{k=1}^{N_g} P(k)(k-\mu)^3 \tag{3.16}$$

The sample kurtosis (μ_4) is whether there are problem outliers within a data set measurement.

$$\textit{Kurtosis, } \mu_4 = \sigma^{-4}\sum_{k=1}^{N_g} P(k)(k-\mu)^4 \tag{3.17}$$

Energy is how much intensity variation is there in the region. It is the measure of heterogeneity. Its value is one when it contains only one gray level image.

$$\textit{Energy} = \sum_{i=1}^{N_g}\sum_{j=1}^{N_g} P_{ij}^2 \tag{3.18}$$

Entropy is the average number of bits to code each gray level, an inverse relationship with skew and energy measurement.

$$\textit{Entropy} = -\sum_{i=1}^{N_g}\sum_{j=1}^{N_g} P_{ij}\, log\, P_{ij} \tag{3.19}$$

3.4.4. Gray Level Run Length Matrix (GLRLM)

GLRLM is searching the image along a particular direction for the pixels runs across having the same gray level value. Several texture features are extracted by texture analysis using this technique. It is based on computing the number of gray level runs of various lengths. Eleven GLRLM features are calculated, that are Short Run Emphasis (SRE), Long

Run Emphasis (LRE), Grey Level Non-Uniformity (GLNU), Run Length Non-Uniformity (RLNU), Run Percentage (RP), Low Grey Level Run Emphasis (LGRE), High Grey Level Run Emphasis (HGRE), Short Run Low Gray-Level Emphasis (SRLGE), Short Run High Gray-Level Emphasis (SRHGE), Long Run Low Gray-Level Emphasis (LRLGLE), and Long-Run High Gray-Level Emphasis (LRHGLE) [86]. Each feature is calculated for four different types of phases. The phases are at the angles of 0^0, 45^0, 90^0, 135^0, in four different directions.. The notations used in this sub-section are illustrated in Table 3.4.

Table 3.4: GLRLM symbols

Symbol	Meaning
P(i,j)	Number of runs with pixels of gray level, *i* and run length, *j*
i,j	Gray level and run length
M,N	Number of gray levels, Maximum run length
n_r	Total number of runs

SRE is short runs joint distribution measurement.

$$SRE=\frac{1}{n_r}\sum_{i=1}^{M}\sum_{j=1}^{N}\frac{P(i,j)}{j^2} \quad (3.20)$$

LRE is the long runs distribution measurement.

$$LRE=\frac{1}{n_r}\sum_{i=1}^{M}\sum_{j=1}^{N}P(i,j)*j^2 \quad (3.21)$$

GLNU is the similarity of gray level values measurement from the complete image.

$$GLNU=\frac{1}{n_r}\sum_{i=1}^{M}(\sum_{j=1}^{N}P(i,j))^2 \quad (3.22)$$

RLNU is the similarity of the length of runs measurement from the complete image.

$$RLNU=\frac{1}{n_r}\sum_{i=1}^{M}(\sum_{j=1}^{N}P(i,j))^2 \quad (3.23)$$

RP is the homogeneity and distribution of the runs measurement of an image in a particular direction.

$$RPC=\frac{n_r}{P(i,j)*j} \quad (3.24)$$

LGRE, the distribution of low gray level values measurement.

$$LGRE=\frac{1}{n_r}\sum_{i=1}^{M}\sum_{j=1}^{N}\frac{P(i,j)}{i^2} \quad (3.25)$$

HGRE, the distribution of high gray level values measurement.

$$HGRE=\frac{1}{n_r}\sum_{i=1}^{M}\sum_{j=1}^{N}P(i,j)*i^2 \quad (3.26)$$

SRLGE, the joint distribution of short runs and low gray level measurement values.

$$SRLGE=\frac{1}{n_r}\sum_{i=1}^{M}\sum_{j=1}^{N}\frac{P(i,j)}{i^2*j^2} \quad (3.27)$$

SRHGLE, the joint distribution of short runs and high gray level measurement values.

$$SRHGLE=\frac{1}{n_r}\sum_{i=1}^{M}\sum_{j=1}^{N}\frac{P(i,j)*i^2}{j^2} \quad (3.28)$$

LRLGE, the joint distribution of long runs and low gray level measurement values.

$$LRLGE=\frac{1}{n_r}\sum_{i=1}^{M}\sum_{j=1}^{N}\frac{P(i,j)*j^2}{i^2} \quad (3.29)$$

LRHGE, the joint distribution of long runs and high gray level measurement values.

$$LRHGE=\frac{1}{n_r}\sum_{i=1}^{M}\sum_{j=1}^{N}P(i,j)*i^2*j^2 \quad (3.30)$$

3.4. Feature Selection

Feature selection is a way to select a feature subset that results in the best performance for classification. The data dimensionality reduction may allow learning algorithms to perform faster, accurately more effectively in comparison to feature extracted classification.

3.4.1. Genetic Algorithm (GA)

GA is a random search method capable of effectively exploring large search spaces. It starts from a set of randomly created or selected possible solutions referred to as population, randomly creating its initial population. Every individual in the population means a possible solution referred to as a chromosome. Within every generation, a fitness function should be used to evaluate the quality of every chromosome to determine the probability of it surveying to the next generation, usually, the chromosome with larger fitness has a higher survival probability. The selection mechanism ensures that fitter chromosomes have a higher probability of survival.

3.4.1. Oppositional Fruit-fly Algorithm (OFA)

The fruit fly algorithm simulates the foraging behavior of the fruit flies. The fruit fly algorithm is a novel technique for seeking global optimization. It began from the examination of food hunting behaviors of fruit fly swarm. Fruit fly is a superb hunter with sharp osphresis and vision. To begin with, it identifies food source from a wide range of fragrances floating all around and flies towards the corresponding place. After reaching close toward the food, it might discover food or go to that particular place with its delicate vision. Food sources are represented by the optima and the methodology of foraging is reproduced by iteratively seeking for the optima in the FA. The improved form of fruit fly algorithm is said to be OFA.

3.5 Classification Models

Data classification is done to classify the images into a pre-defined category. There are various classes of classification. The various types of classifiers are Decision Tree, Adaptive Boosting (AdaBoost), Random Forest (RF), Support Vector Machine (SVM), Generalized Linear Model (GLM) and Neural Network (NN). These classifiers are chosen as the state of the art methods for the classification and they train all the model types available for data set are typically fast to fit.

3.5.1. Decision Tree

R package party design the decision trees, a graph in the form of a tree to show the choices with their results. The graph nodes act as the choices and the edges as the conditions. A model started with training data in the form of observed data. To verify and improve the model R package, a validation data set is used. A new predictor variable set is used in this model to make the decisions on the data category [88].

3.5.2. Adaptive Boosting

Boosting designs a high accurate prediction rule using a large number of rules that are relatively weak and inaccurate, with sufficient data and weak classifiers that satisfy the condition of weak learning. Successive trees give extra weights to points incorrectly predicted by earlier predictors; a weighted weight is in the last prediction. It success without over-fitting, the weak hypothesis have an accuracy better than random, have sufficient data relative with respect to the complexity of the weak hypothesis [89].

3.5.3. Random Forest

RF response when there are changes in classification or regression trees. RF, add a random layer to bag and construct each tree by the different bootstrap samples. In standard trees, each node is split using the best split from all the variables, from the predictors' subset chosen at the same place randomly [90].

3.5.4. Support Vector Machine

SVM classifier works on the training data that design the optimal separating between the classes. The data results in the decisions, which classify the two types of classes like a hyper-plane [92]. SVM classifies the data as a binary classification. That classification then extended for multi-class problem classification. For the classification of this work, the normal and abnormal classes are considered.

Table 3.5: Parameters details for SVM

Parameters used for SVM	
Kernel	'rbfdot'
Nu	0.01
Epsilon	0.03

3.5.5. Generalized Linear Model

GLM estimates the outcome models using regression. They include not only Gaussian distribution (normal) but also Binomial, Poison, Gamma, and Tweedie distributions. They serve according to purpose, distribution, and choose the link function as per the requirement with prediction/ classification. GLM obtained the exact result of interest, undergo a long historical development. GLM results in asymptotic non-identity link [92].

3.5.6. Neural Network

The NN is used to train the network. Each network has one input layer and some neurons equal to the number of the selected features, one hidden layer, and some neurons and one output layer of one neuron for the classification in the liver portion. The output neuron of each network has two outcome values, 0 and 1, for the classification result [17].

3.6. Concluding Remarks

The experiment methodology to develop research objectives presented in this chapter. Its main constituents are, CT and MR images data description, pre-processing steps, study details in experimentations, feature extraction details and the classifiers details. It presents a general description of the complete medical image processing work. The data details collection, and their description with the experimentations. In the next step, pre-processing details are there, to get a desired look with the tumor region. In the next step, the details of the study are described with the experimentations regarding the details of the images and the aim of the experiment. In the next step, the details of the features are described that are extracted from the enhanced images. In the last step, there is description of the all the classifiers, that are used in the work to detect and classify the cancerous diseases. This methodology section describes about the main steps that are processed in the work, with their details description as the sub-parts of the sections.

Chapter 4

CT IMAGE PROCESSING (STUDY 1 AND STUDY2)

This chapter presents the work that was done on the CT images as the input. It contains the two different studies experimentations. It may be presented as the experimentation with only the CT images, from the dataset set description to the complete image processing work to detect and classify the liver cancer classes. The details present here are the parts of these experimentations.

4.1. STUDY 1

For these experiments, a large number of CT images were used which is a collection of normal liver images and cancer images. There are 600 clinically acquired CT images in total, 300 of which are of HCC and 300 are of MET. The ROI of 30 X 30 pixels is extracted from each image, with a single ROI. The normal liver ROI can be chosen from the entire liver section. The tumor ROI might be chosen from among the abnormal liver HCC and the MET. To detect the tumor, the input might be chosen from a set of all images. After tumor detection, the inputs are the HCC tumor's abnormal liver as the original liver cancer and the MET as the secondary liver cancer. All of these images have an appropriate tumor region extracted as ROI. Each image has its ROI for IROI selection. A particular image has one SROI to determine the ratio characteristics, while IROI can range from 1 to 5 in a particular image. The data is separated into training and testing sets based on the desired performance. The number of IROI sets is the same as the total number of experiments. However, the number of SROI sets may be smaller than the number of IROI sets. A single image may have 1-5 IROI, but the SROI is the same for all IROI. The total number of data images is shown in the Figure 4.1.

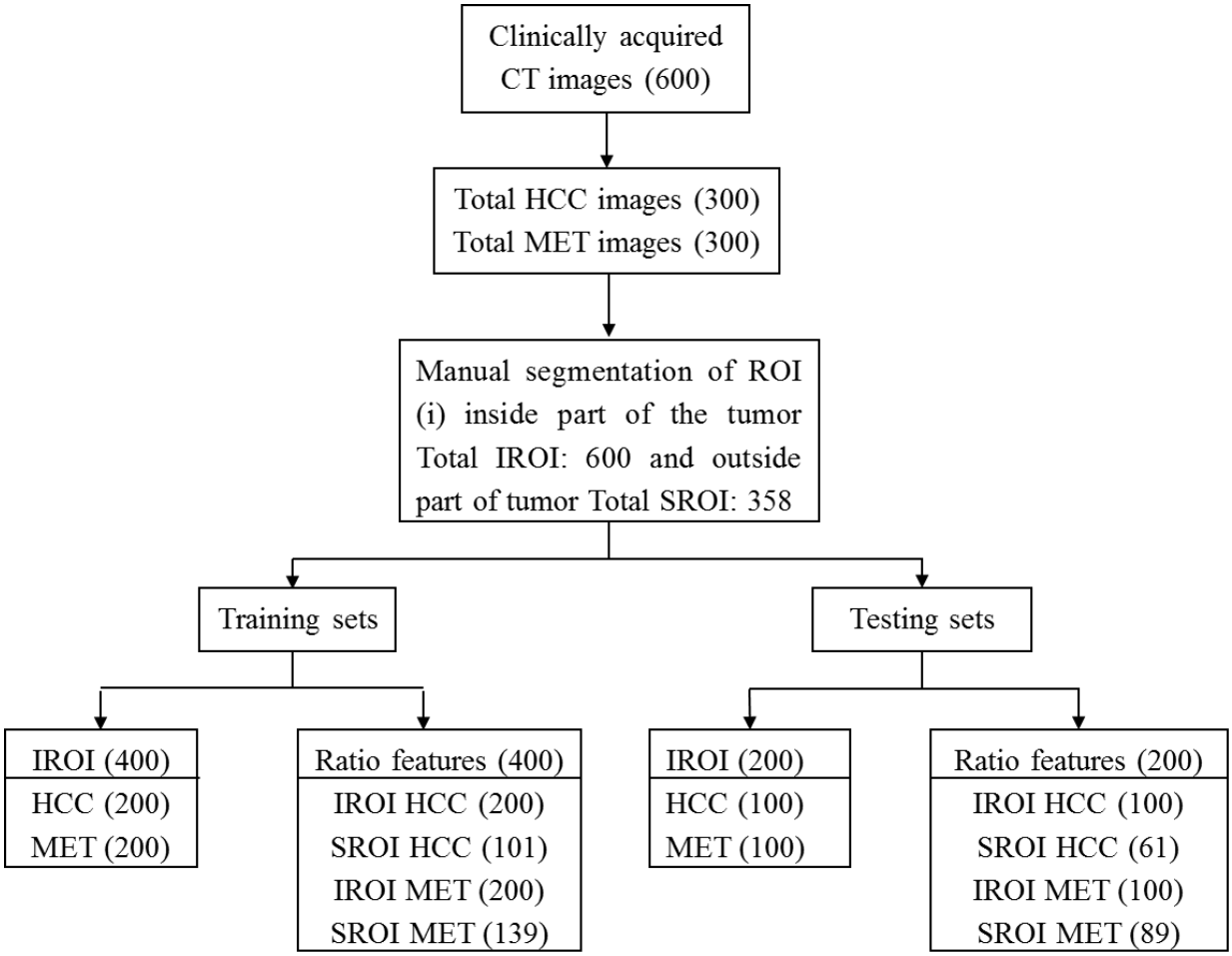

Figure 4.1. Dataset description for the proposed work.

The inputs images were selected from the database in the experiment. The tumor-marked locations are highlighted in red in the images as shown in Figure 4.2 to 4.7. These images represent several samples of a specific type of disease. The tumors marked are the various sides of the tumors in the liver section. A variety of tumor representations are present in the tumor-infected region. These three images depict the presence of a tumor in the liver, which might be present on any side, increasing or decreasing from within the liver region.

HCC marked ROI

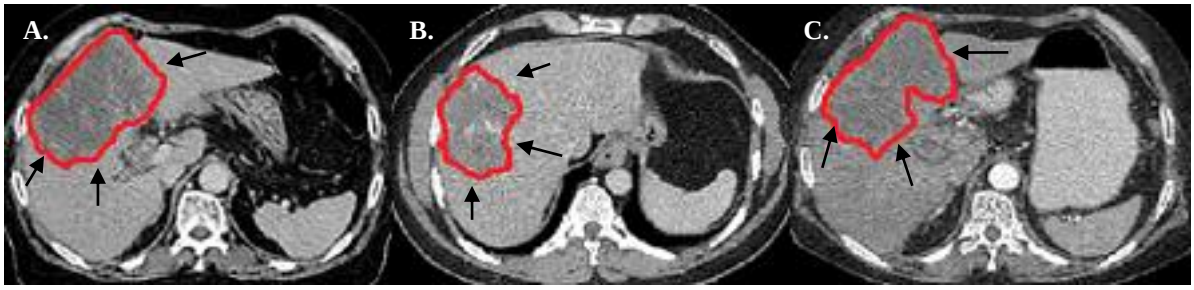

Figure 4.2. HCC marked region by the lines in the arrows mark, **A.** Size of liver changing place. **B.** Side portion region of the liver. **C.** Main boundary region of the liver.

MET marked ROI

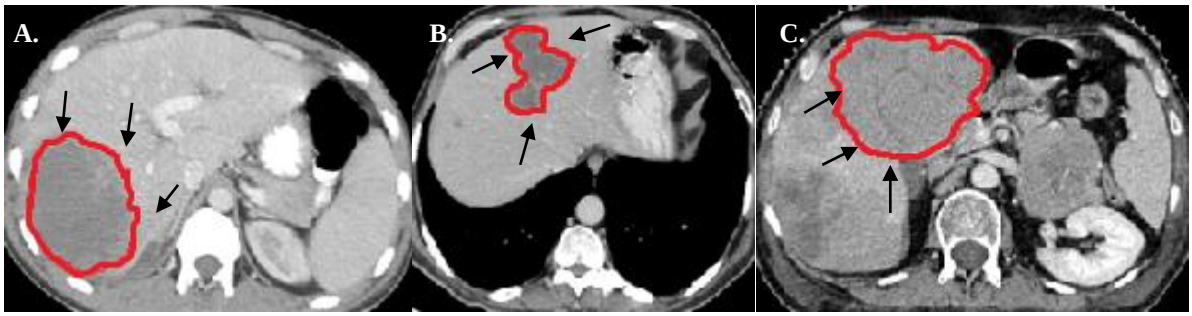

Figure 4.3. MET marked region by the lines with the arrows mark **A.** side bottom portion of the liver. **B.** exists inside the liver portion. **C.** Ending portion of the liver region.

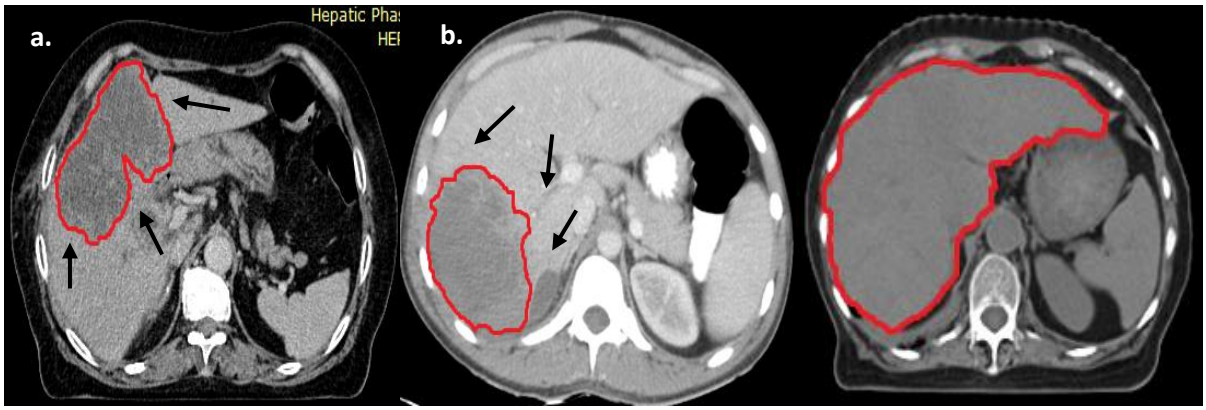

Figure 4.4. a. HCC, b. MET. The region marked is the tumor portion that is present inside the liver; arrows are marked to represent the sides for the direction of the tumor. c. Normal liver, the marked area is the complete liver portion of the body.

The images are enhanced using the CLAHE algorithm. The images are marked by the red color represented the tumor portion. The marked tumor portion have different intensity level present in the images. The enhance images look have a different look on viewing in comparison of the original one. These different tumors enhanced images allow to differentiate with the non-infected regions of the liver.

HCC enhanced images

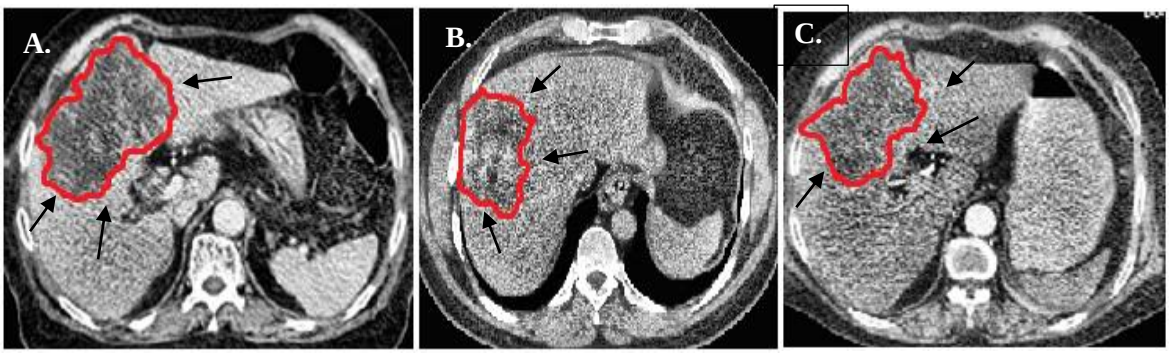

Figure 4.5. HCC marked by the lines in the arrows mark on the enhanced region **A.** size of liver changing place. **B.** side part of the liver. **C.** upper cut region of the liver. The arrows marked are an indication to represent the enhanced tumor from different sides for its position.

MET enhanced images

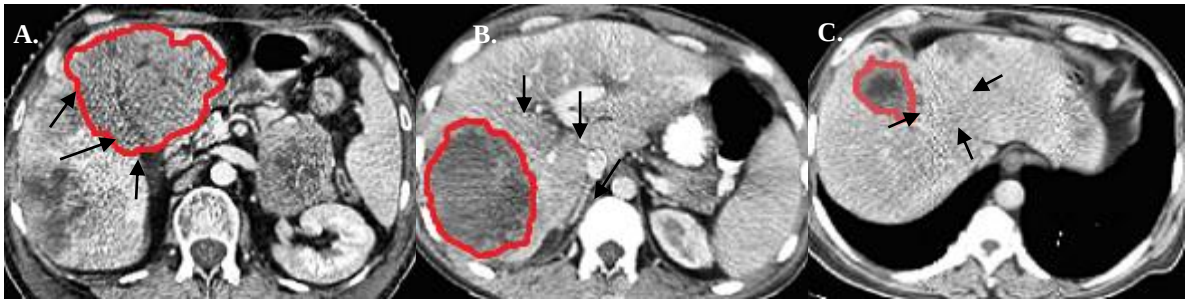

Figure 4.6. MET marked by the lines in the arrows mark on the enhanced region **A.** upper end of the liver portion. **B.** lower part of the liver region. **C.** inside the liver portion. Some liver portion is surrounding the tumor region. The arrows marked are an indication of the tumor portion.

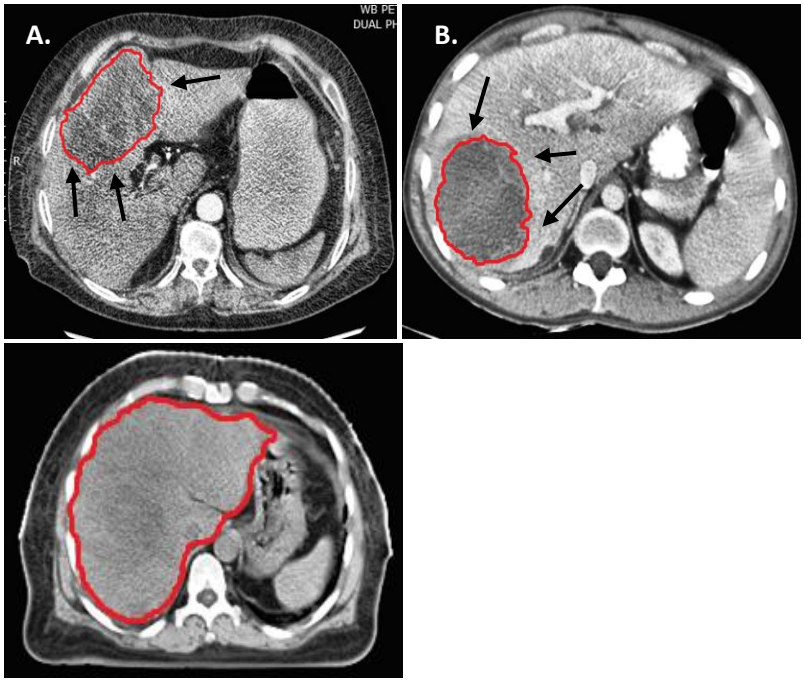

Figure 4.7. a. HCC, b. MET. The region marked is the enhanced tumor portion inside the liver. The arrows marked are the enhanced tumor portion from different sides as directions. c. Normal liver, the marked area is the complete enhanced liver portion of the body.

The 300 IROI images feature values and ratios of IROI and SROI for HCC and MET are calculated with all the input CT images. The total number of images considered for creating a dataset is 300, which is further subdivided into 200 training sets and 100 testing sets for all designed experiments. For both the IROI and the SROI, a size of 30 X 30 pixels is chosen for the calculation of all feature values for each image. The IROI values and the estimated ratio of the IROI and SROI values [85] are called feature vectors (FV). FOS, GTDM, and GLCM identified these FV as a feature class (FC) for both types of diseases [86]. Furthermore, GA was utilized for feature selection, and the features were ranked based on their weights. To classify the group of diseases, SVM was employed as the classifier.

4.1.1. Experiment 1:- A set of 300 images for both HCC and MET are selected from the CT images database. These are selected with the clear indication of the desired tumor size in the image. From one enhanced image the number of the IROIs extracted may vary from 1-5, depends upon the size of the tumor.

4.1.2. Experiment 2:- A set of 300 images for both HCC and MET and their respective SROI are selected from the large CT images database. In case of more than one IROI from the same image, then their SROI is the same for all of them.

4.1.3. Experiment 3:- The experiments performed using GA as a feature selector. The IROI values are tested with the best feature values. For all the sub-experiments, there is a number of selections variation with the best features from the total features.

4.1.4. Experiment 4:- The experiments performed using GA as a feature selector. The ratio values of IROI and SROI are tested with the best feature values, the sub-experiments varying with the number of features, selected from the total number of features. The block diagram shown in the Figure 4.8 is for the purpose of the generalization of the present work. This block diagram represent the overall processing of the Study-1.

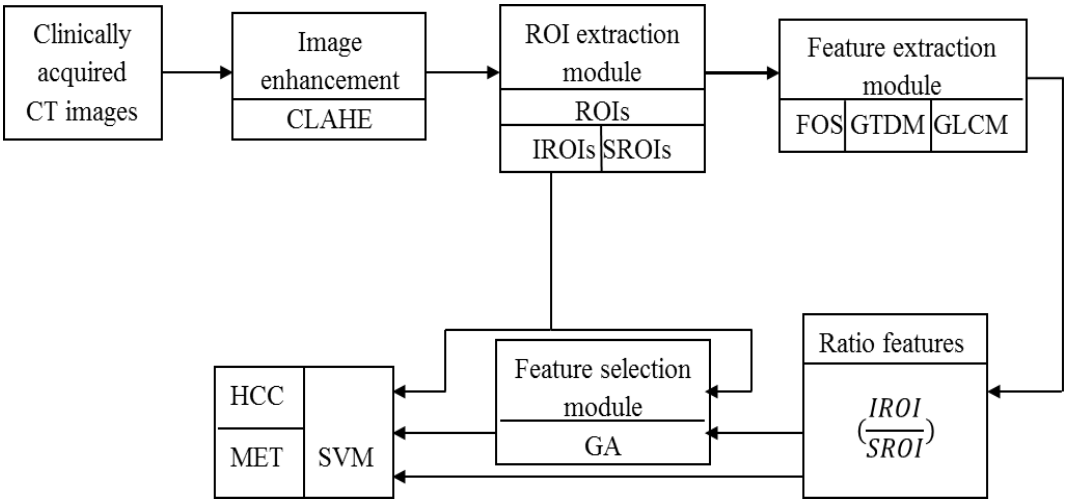

Figure 4.8. Generalized proposed work algorithm.

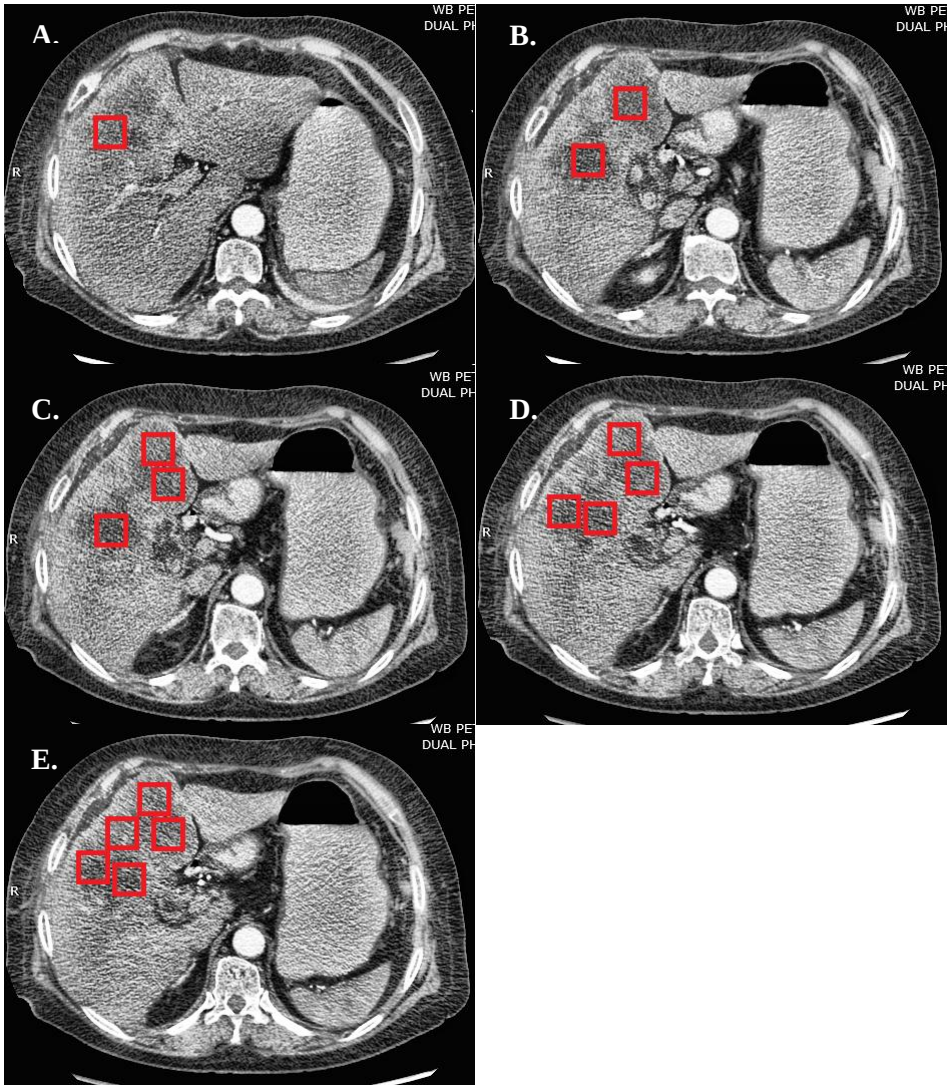

Figure 4.9. Enhanced images marked IROIs CT, the red box represent IROI. **A.** One IROI **B.** Two IROIs **C.** Three IROIs **D.** Four IROIs **E**. Five IROIs. For more than one IROI, any two IROI do not overlap, it doesn't include the tumor boundary and it doesn't include the outside tumor region.

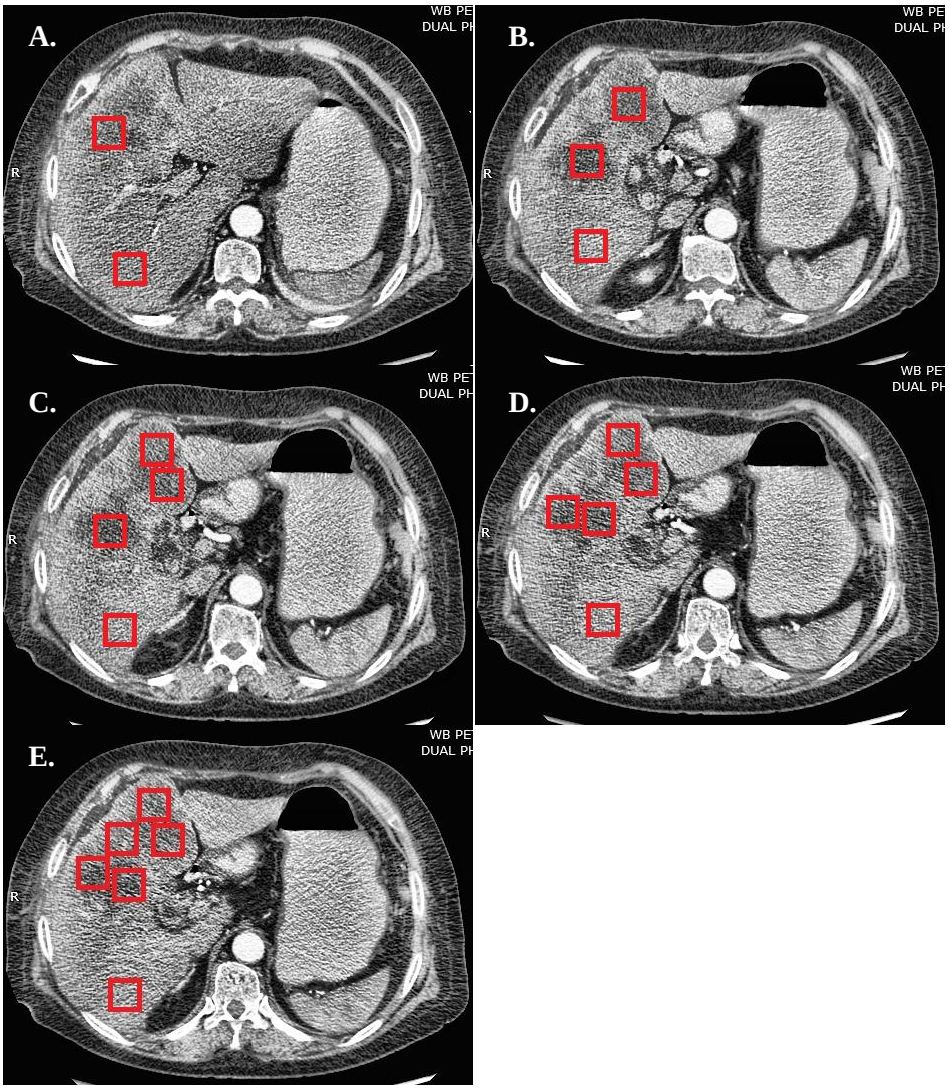

Figure 4.10. Enhanced images marked IROIs and SROI CT. **A.** One IROI and SROI **B.** Two IROIs and SROI **C.** Three IROIs and SROI **D.** Four IROIs and SROI **E.** Five IROIs and SROI.

Figure 4.9 and Figure 4.10 represent the enhanced images five sets. For Figure 4.9, there are five sets that representing the case of IROIs, from Figure A-E, there are one to five IROIs are representing. For Figure 4.10, there are five sets that representing the case of IROIs with a single SROI in each of them, from Figure A-E, there are one to five IROIs are representing. The ratio feature is designing by the ratio of IROI feature to the SROI feature.

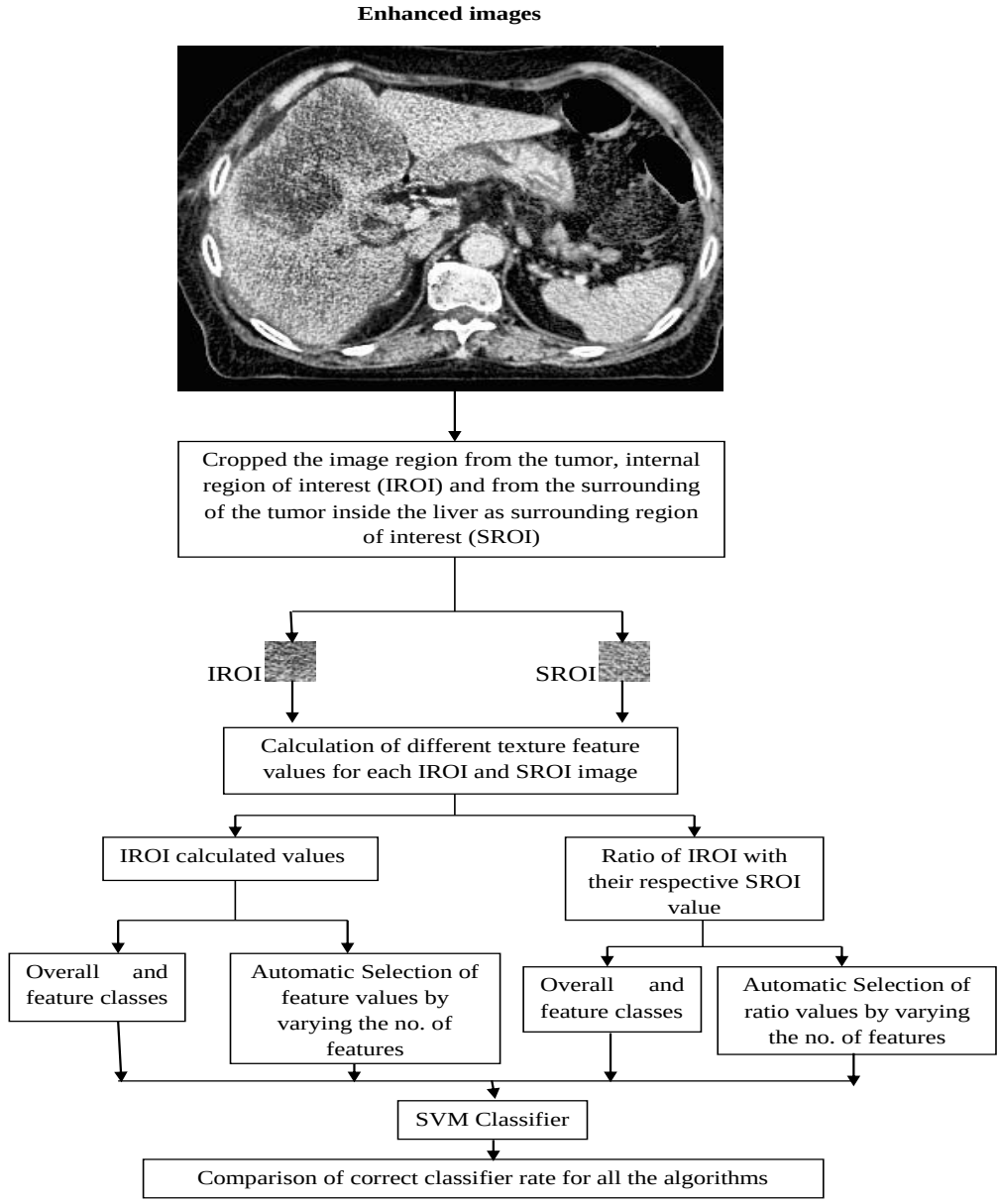

Figure 4.11. Flowchart of the complete work using the original enhanced image.

After applying, GA as the feature selection, there is automatically selection of the features with respect to their classifier rate. There are 20 selected IROI best features and 20 selected ratio features. GA resulted in optimally selected features with the order of preference of the features [93-95].

Table.4.1. Selected features after the applications of GA in the order of preferable rank of the features.

Feature rank	Selected 20 IROI features	Selected 20 ratio features
1	Strength	Skewness (FOS)
2	Entropy	Busyness
3	Kurtosis (FOS)	Cluster shade
4	Contrast	Median
5	Inverse difference moment normalized	Inverse difference moment normalized
6	Difference entropy	Sum average
7	Cluster shade	Difference entropy
8	Variance (FOS)	Entropy
9	Sum variance	Mean (FOS)
10	Difference variance	Complexity
11	Mean (FOS)	Auto-correlation
12	Dissimilarity	Mode
13	Inverse difference normalized	Entropy (FOS)
14	Skewness (FOS)	Dissimilarity
15	Sum average	Sum variance
16	Auto-correlation	Variance (FOS)
17	Contrast (GTDM)	Sum entropy
18	Energy	Energy (FOS)
19	Coarseness	Correlation
20	Homogeneity	Information measure of correlation1

Figure 4.11 shows the complete processing workflow chart utilizing the improved images. In the first, the IROI and ratio features are calculated using the appropriate ROI pixel size. The ROI of the IROI and SROI have feature extracted values calculated. These estimated

IROI values and ratio features are used to classify the types of liver disorders further. These extracted features were processed for the classifier using an individual classifier rate and a group of features, designed based on their classifier rate or a group of feature types. Similarly, ratio features are computed and categorized both overall and by feature class. The SVM classifier is used for classification. The classifier accuracy, specificity, and sensitivity are calculated and compared across all experimental results.

4.2. STUDY 2

4.2.1. Experiment 5:- The inputs are drawn from a set of 1638 images of normal and abnormal liver, from which FOS, GTDM, GLRLM, and GLCM are calculated. For each of the 1638 photos, 44 features are extracted. The ROI is 25 x 20 pixels. R-part decision tree, AdaBoost, RF, k-SVM, GLM, and NN are among the classifiers used for classification. The classifier detects the tumor based on the overall attributes by using 844 abnormal (483 MET and 361 HCC) images and 794 normal images as input. The database workflow is shown in the Figure 4.12.

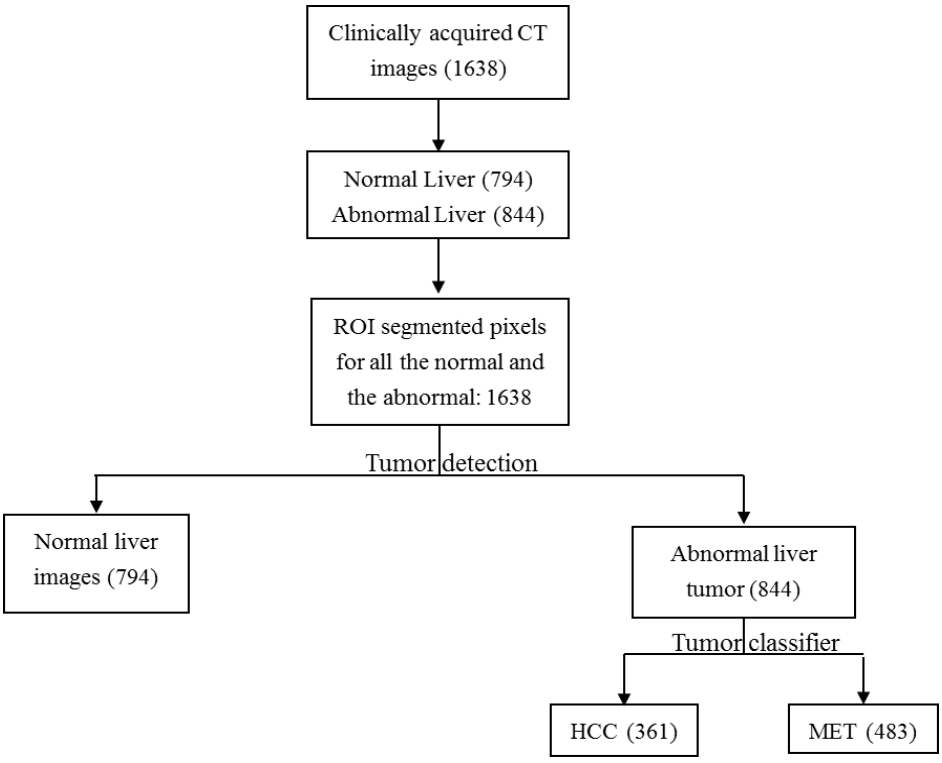

Figure 4.12. Work flow of the data distribution.

The block diagram of Figure 4.13 represents the enhanced images as the input images of the normal liver and the abnormal liver tumor images. The tumor images show HCC and MET liver diseases. The cancer is detected by computing all of the ROI features and comparing the liver's normal and abnormal tumor images. After tumor detection, the tumor is classified, with HCC being the primary liver cancer and MET being the secondary liver cancer. GLM, Adaboost, SVM, RF, R-part, and NN classifiers are used for classification. Their classification accuracy is compared, and all classification results are ensembles to increase detection and classification rate.

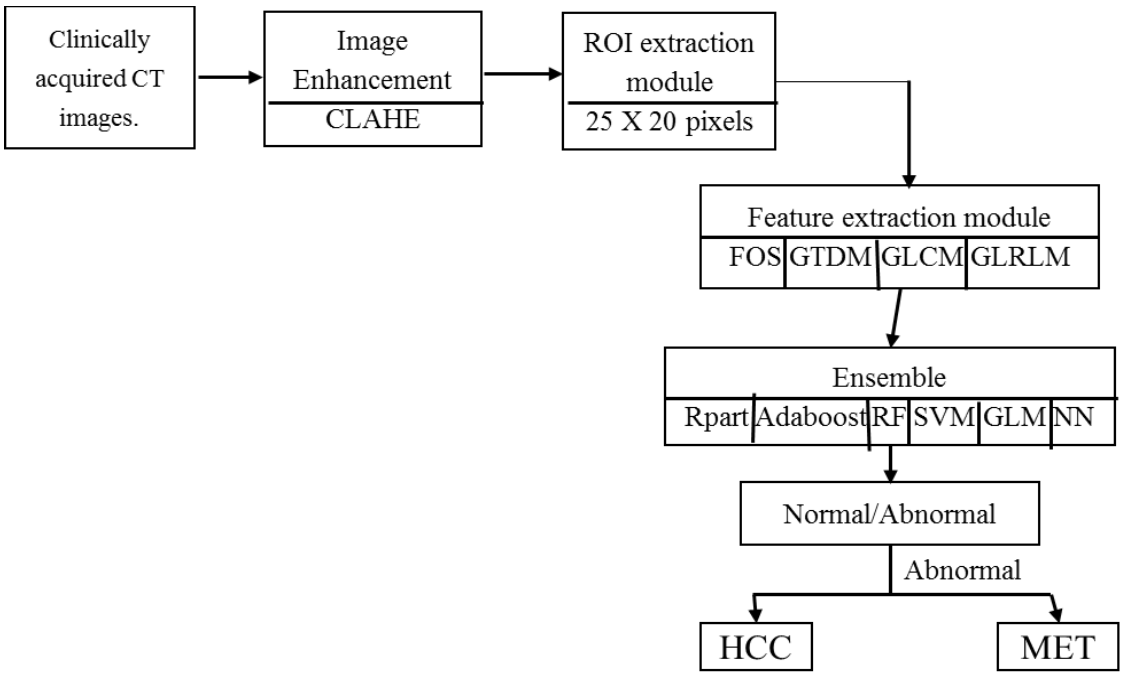

Figure 4.13. Block diagram generalization of the proposed work.

To categorize the tumor further, use the input as 483 MET liver cancer and 361 HCC liver cancer types of images to classify the tumor as main and secondary type of tumor. An ensemble model is created by merging all of the classifiers to improve the overall detection and classification performance shown in the Figure 4.14. The model's primary goal is to detect and

classify liver cancer diseases in their respective categories. To improve accuracy, six models are utilized as classifiers in an ensemble. The models are trained on 70% of the dataset and tested on 30% of the datasets. The suggested model entails ensemble all of the classifiers to increase their detection rate and classifier rate results.

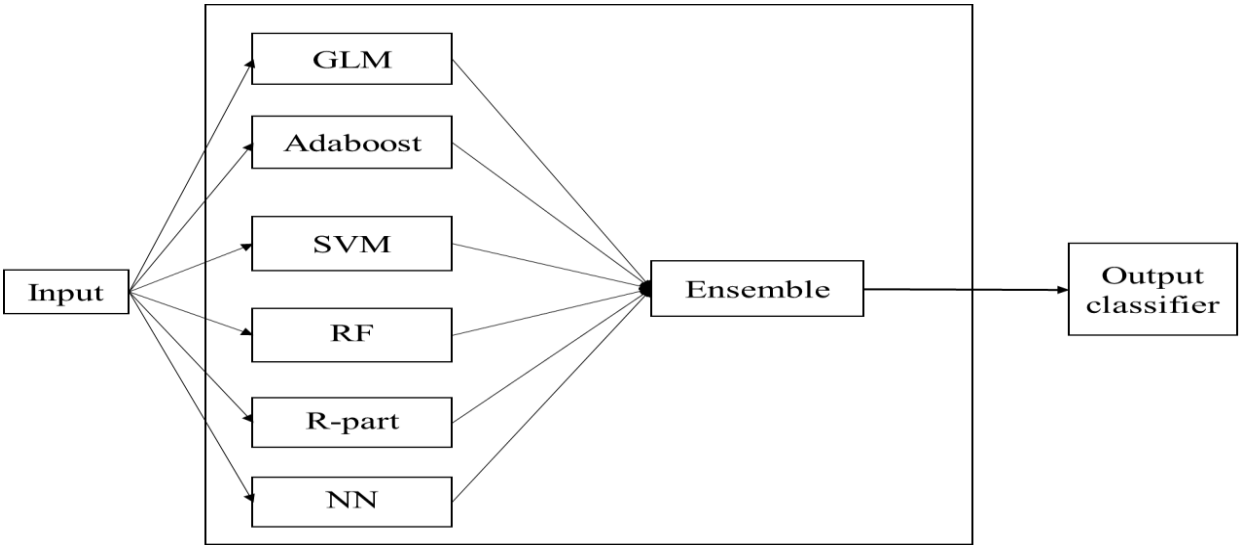

Figure 4.14. Block Diagram to represent Multi-level Ensemble model.

4.3. Concluding Remarks

The CT image processing was used to explain studies 1 and 2. The ROI size varies between the two trials. There are four experiments in Study-1 that use three different types of feature extractions. These experiments use feature selection to determine the classes of experiments for the IROI and ratio features. In Study-2, experiment 5, ROI is extracted using four classes of features, and six classifiers are employed to test their classifier rate for tumor identification and classification. To increase the classifier rate, an ensemble model is designed by employing all six classifiers. A variable ROI size produces different results, allowing for tumor size change in different kinds of experiments.

Chapter 5

CT AND MR IMAGE PROCESSING USING GABOR FILTER (STUDY 3)

5.1. INTRODUCTION

Gabor filter applications have various machine vision learning methods, like texture segmentation, edge detection, object detection, image representation and handwritten numerals recognition. It is used in applications ranging from texture analysis to image compression. It is also selected for texture segmentation: the filter banking and the filter designing approach. The Adhoc filter parameters in filter banking are not necessarily optimal for a particular processing task [96]. The Gabor filter family has frequency bandwidth in octaves and orientation bandwidth in 45 degrees. The orientation is generally selected in four directions: 0, 45, 90 and 135 degrees. The Gaussian function scale parameter is generally selected intuitively and assumed to be a constant. The Gabor filter's real and imaginary components response is typically identical and only has 900 phase differences [97]. Gabor filters are the wavelets group, the filtered images set is obtained by convolving the input image with the Gabor filters. Each wavelet captures energy at a particular frequency and in a particular direction.

Each image represents the image information at a particular scale and specific orientation. Gabor features can be calculated from each filtered image and to retrieve images.

Gabor wavelet implements rotation invariant texture, feature extraction for texture classification and texture segment. Extracting texture features, Gabor wavelet with pre-defined scale set and orientations, extracting time-frequency coefficients from each scale and direction. Gabor wavelet used for variant scale set and direction set. Gabor wavelets also attain maximum joint space-frequency resolution in texture extraction for texture representation and texture spatial localization. Spatial frequency, maximize the simultaneous localization of energy in both spatial and frequency domain. The wavelet filter parameters are tuned to achieve the best result [98]. The Gabor filter parameters work for the texture classification accuracy: the highest frequency as the center frequency of the filter (FM), the total number of frequencies (*n*F) and the number of orientations (*n*O). Gabor filters have a higher potential to separate tumor regions.

Gabor filter is a linear filter, whose impulse response is the harmonic function multiplied by a Gaussian function. Its Fourier transform is the convolution of the Fourier transform of the harmonic function and the Fourier transform of the Gaussian function. Its frequency response is the impact function and Gaussian function's convolution, and the Gabor filters have a very good band-pass (BP) nature.

Gabor filters have excellent properties for feature extraction: scaling, space, spatial frequency, and orientation. A two dimensional Gabor function *g(x, y)* and its Fourier transform *G (u, v)* written as:

$$g(x,y)=\left(\frac{1}{2\pi\sigma_x\sigma_y}\right) exp\left[-\frac{1}{2}\left(\frac{x^2}{{\sigma_x}^2}+\frac{y^2}{{\sigma_y}^2}\right)+2\pi jWx\right] \quad (5.1)$$

In the frequency domain,

$$G\ (u,v)= exp\left\{-\frac{1}{2}\left[\frac{(u-W)^2}{{\sigma_u}^2}+\frac{v^2}{{\sigma_v}^2}\right]\right\} \quad (5.2)$$

The time-frequency transformed the based method of texture discrimination, based on Gabor filters. In Gabor transform, a signal is represented by a sinusoid that is modulated by translated Gaussian windows. Gabor transform employs such a kernel for time-frequency signal analysis. 2D Gabor filter is the local BP filter with optimal joint localization for the spatial and frequency domains. The Gabor feature pairs have the same orientation and spatial frequency but differ in the Gabor energy phase. Gabor functions have low-level oriented edge and texture discriminators, sensitive to different frequencies and scale information. By selectively change each Gabor function parameter, tune the filter to the particular patterns in the images. Gabor function's parameters have the object's particular orientations, scales, and frequencies, considering the good descriptors in the local image content [99-101].

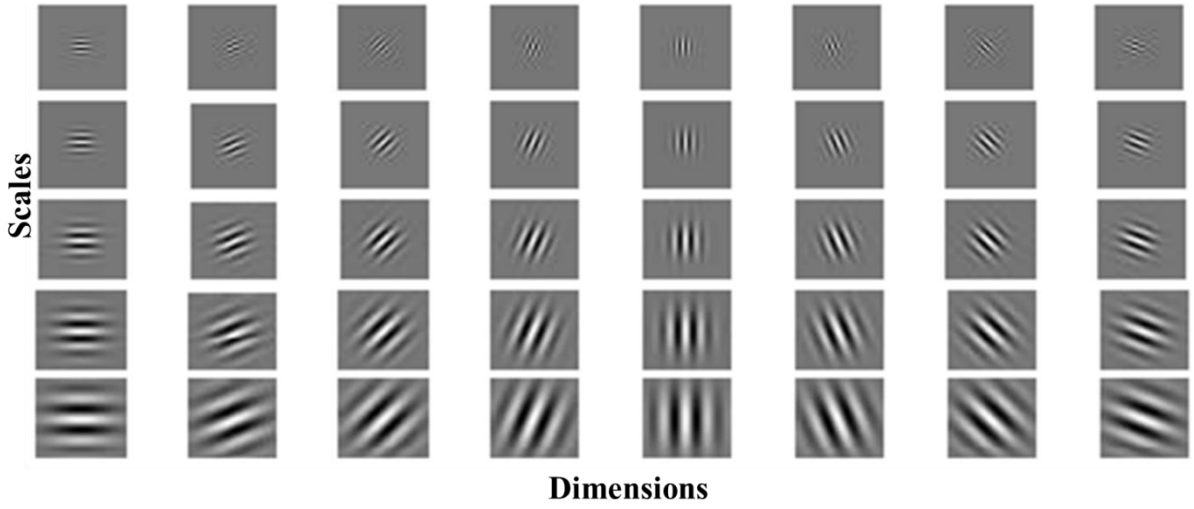

Figure 5.1 a. Five scales and eight orientations of the Gabor filter.

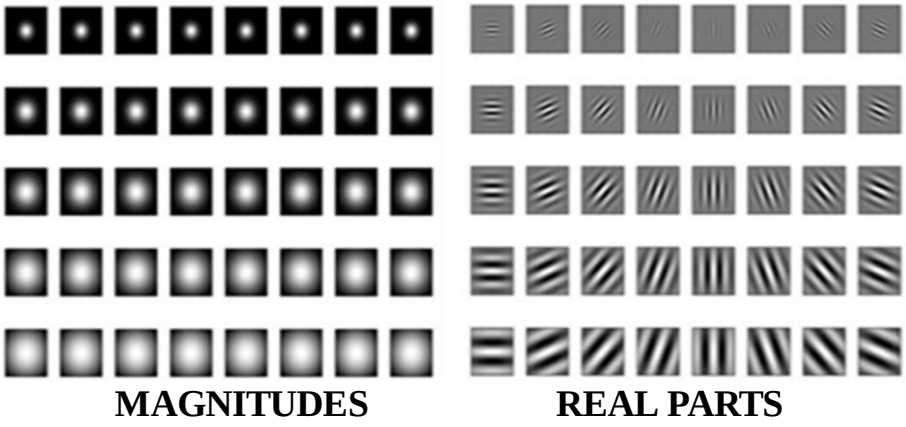

Figure 5.1 b. Magnitudes and real parts composition of the Gabor filter.

Figure 5.1(a) shows the pattern of 40 Gabor filters images that are designed by using the five scaling (spatial frequencies) and the eight orientation parameters. After applying such scaling and orientations using Gabor filters, the image resulted in 40 different images pattern. The pattern of the 40 different Gabor filters is designed so that it can represent the type of samples of the images that derive by using convolution with Gabor filters. This type of Gabor filter bank is a 5 by 8 cell array matrices type. Each matrix plays the role of a 2-D Gabor filter. Figure 5.1(b) separates the magnitudes and the composition of the real parts of the Gabor filters. A particular filter that is designed here is defined from a particular scale and a particular orientation. For a specific image, scale set is configured to capture the specific components of the frequency band. The real part represents the composition from the original image, and it acts

like the subset of the original image. Mathematically, they are calculated using their respective formulae.

Gabor filters used as the key features for texture processing local orientations and spatial frequencies. The images are filtered by a family of Gabor filters tuned to several resolutions and orientations. The filter bank is carried out with eight orientations and five scales, this yields a total of 40 filters that cover the frequency domain in multi-resolution decomposition. A Gabor filter bank is the BP regularly spaced filter set that varies in orientation and center frequency. The number of scales and orientations of the Gabor filter bank increases that add to the system's complexity, its computational time and an increase will not result in the classifier accuracy. Gabor filters are extracting the local spatial frequencies, which provide structural features of the information in the image. Gabor filters extracting the texture features based on localized spatial frequency information efficiently.

Algorithm:-

Step 1:- Initialize the variable to store the original CT and MR images.

Step 2:- The Image conversation and image enhancement are done.

Step 3:- Enhancement CLAHE algorithm is used to get better visualization with the tumor for the image.

Step 4:- The ROI extracted from the complete enhanced images.

Step 5:- A suitable size enhanced part as the input variable for the parameter values.

Step 6:- From all the images, the same size portion is extracted.

Step 7:- The scaling and orientation values parameters are calculated by using the Gabor filters as stated in eq. (5.1).

Step 8:- The various classes of the tumor are designed to detect and classify the liver tumor cancer.

Step 9:- The classification is performed using various classifiers, Adaboost, Support Vector machines (SVM), Neural network (NN), r-Part, Generalized linear model (GLM), Random forest (RF) to check their classifier rate variation and K-fold cross-validation (CV) is also performed to compare the performance of various classifiers.

5.2. IMAGE PROCESSING WORK:

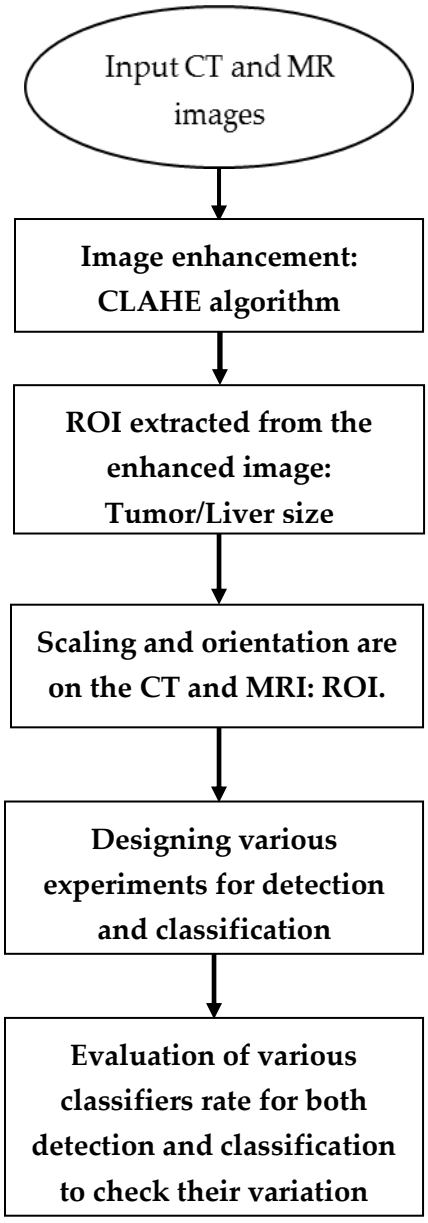

Figure 5.2. The complete overview of the work in the form of a flowchart.

Figure 5.2 represents the flow of research work. Clinically acquired CT and MR images of the normal and abnormal liver are pre-processed to enhance the diagnostic information present in the images. The CLAHE algorithm is a suitable enhancement method, and the enhanced images have a clear visualization for the tumor present in the liver. The ROI portion is segmented from an appropriate region in the tumor portion. This ROI has 25 X 20 pixels in size. The ROI, five

scales and eight orientations applying to the images using Gabor filters parameters. That results in 40 Gabor filters for image processing work. The various experiments have been designed to check the detection and classification variation rate on all the input images. The classification is done on the designed experiments to classify the images into a pre-defined category. Various classifiers are used to detect and classify the tumors and compare their classifiers rates in all the designed experiments [102, 103].

5.3. EXPERIMENTATIONS

There are various combinations designed so that we can define a set of images to detect and classify a tumor on CT images, MR images and in the combination of both of them. There are various types of data images on the CT images to check the presence of a tumor and classify that type of disease. Similarly, for the MR images, there are various types of data images results to check the presence of a tumor and classify that type of disease. There is a combination of both of these CT and MR images to check the presence of a tumor, using this combination, we can check how there is variation in tumor detection with their comparison. This work out in tumor detection using a large combination of different types of data images and yield in a result that inclusion of different class images in tumor diseases will change the detection rate of a tumor in particular class images.

Experiment 6:-1957 abnormal images of CT and MR and 2609 normal images of CT and MR. They are classified to detect the presence of a tumor on them. These are the combinations of the CT and MR images data to detect the presence of a tumor overall in all the CT and MR images.

Experiment 7:- 1054 abnormal images and 2274 normal images of MR. They are classified to detect the presence of a tumor on them. To check the presence of a tumor on the MR images to check their tumor detection rate on them.

Experiment 8:- 844 abnormal images of CT and 395 normal images of CT. They are classified to detect the presence of a tumor on them. To check the presence of a tumor on the CT images to check their tumor detection rate on them.

Experiment 9:- 600 HCC images and 513 MET images of MR. The diseases are classified on these MR images that have a tumor to classify the type of the diseases on them.

Experiment 10:- 361 HCC images and 483 MET images of CT. The diseases are classified on these CT images that have a tumor to classify the type of diseases on them.

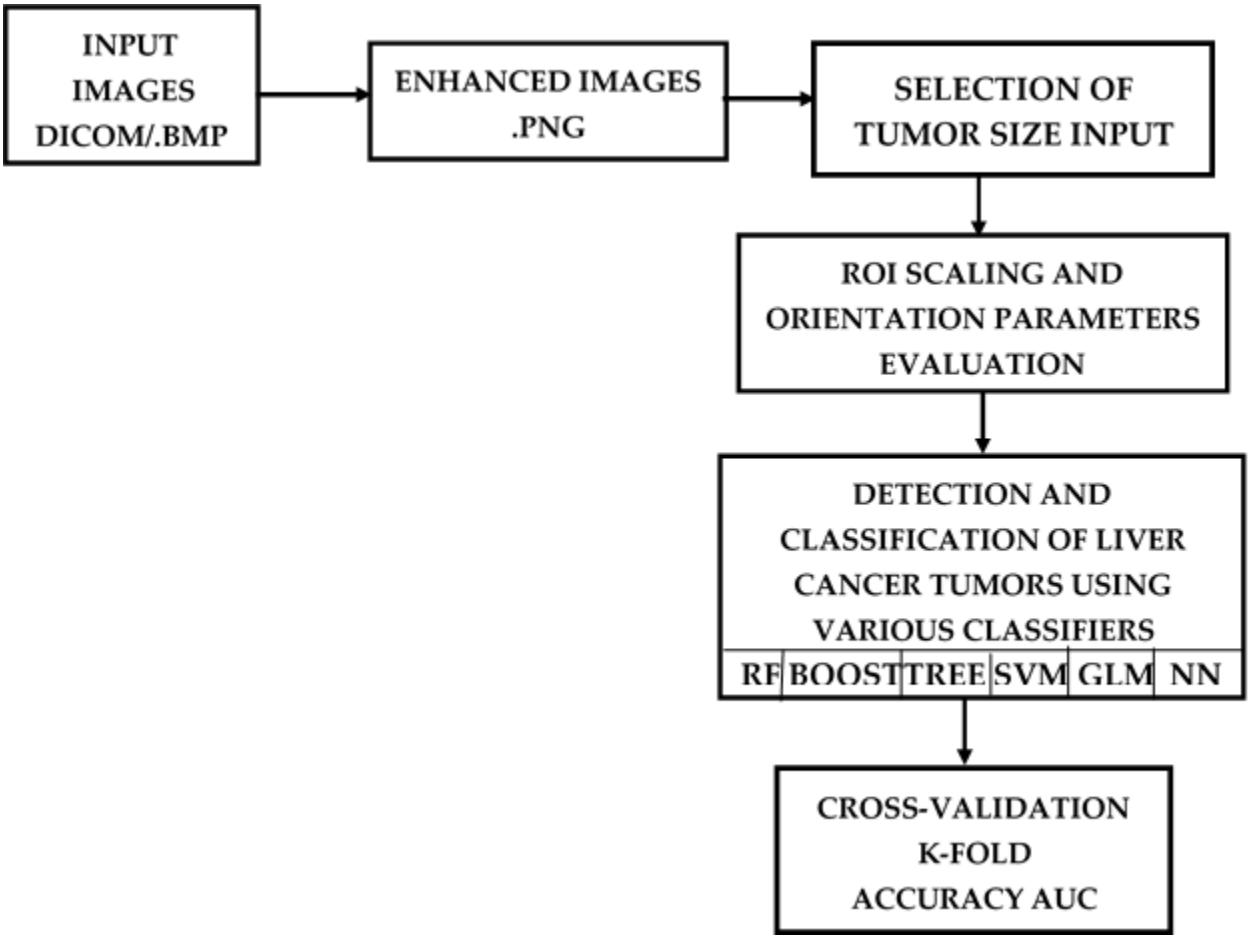

Figure 5.3. A block diagram representing the stages of work processing.

Figure 5.3 represents the block diagram related to the details of the stages of the work. For the first input stage, there is an input image of the original patient collected from the hospitals in the form of the DICOM image. The DICOM image is converted to the .bmp image to do the image processing work. These are converted into the enhanced images results. From the enhanced images, there is ROI extraction, on that ROI, scaling and orientation parameters evaluation is done using the Gabor filter designs. There are various classifiers to detect the tumor and classify the tumor, and to compare their result to get the best response among them. The various types of classifiers are Decision Tree, Adaptive Boosting (AdaBoost), Random Forest (RF), Support Vector Machine (SVM), Generalized Linear Model (GLM) and Neural Network

(NN). These classifiers are used to check their accuracy for the detection rate and the classifier rate variation and find the best results.

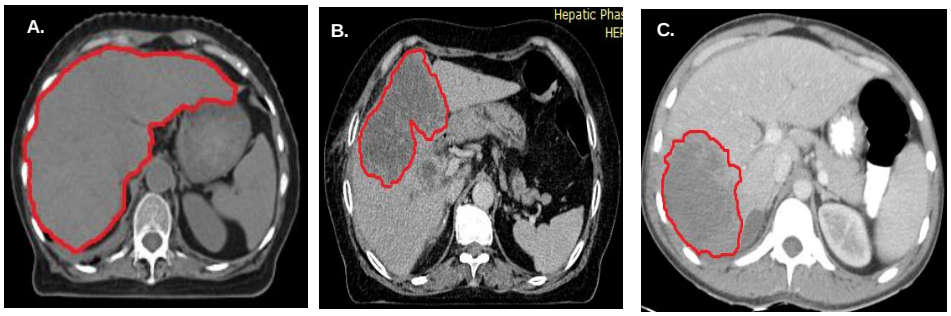

Figure 5.4. RED marked region on the CT liver section or the liver sub-section tumor part A. CT Normal liver region marked. B. CT HCC marked of the liver portion region. C. CT MET marked of the liver portion region.

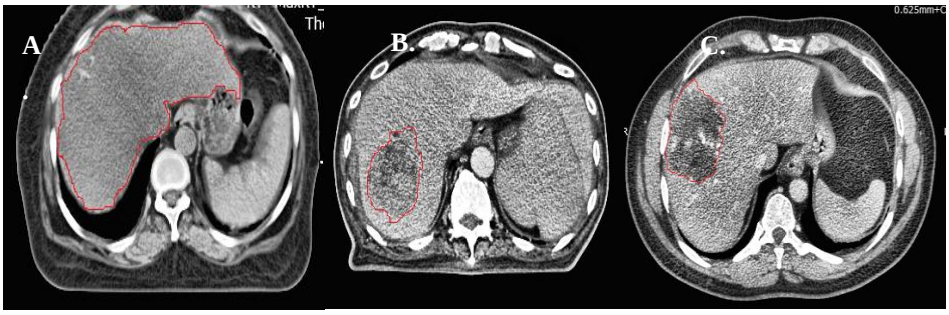

Figure 5.5. RED marked the region as the liver section or the liver sub-section tumor part in the CLAHE CT enhanced images. A. CLAHE enhanced CT Normal liver region marked. B. CT HCC marked of the CLAHE enhanced liver portion region. C. CT MET marked of the CLAHE enhanced liver portion region.

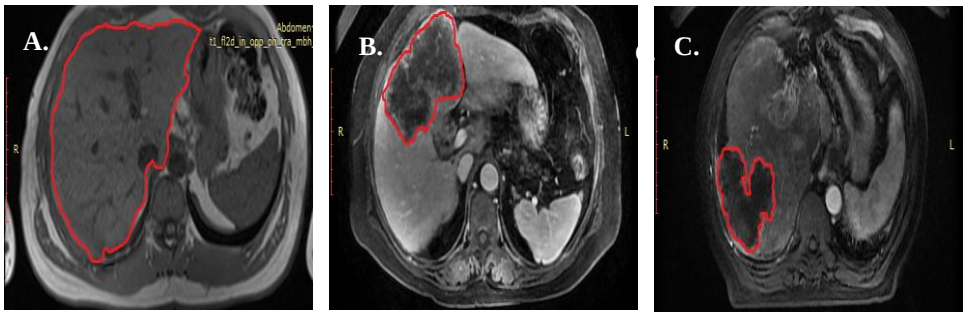

Figure 5.6. RED marked the region as the liver section or the liver sub-section tumor part A. MR Normal liver region marked. B. MR HCC marked of the liver portion region. C. MR MET marked of the liver portion region.

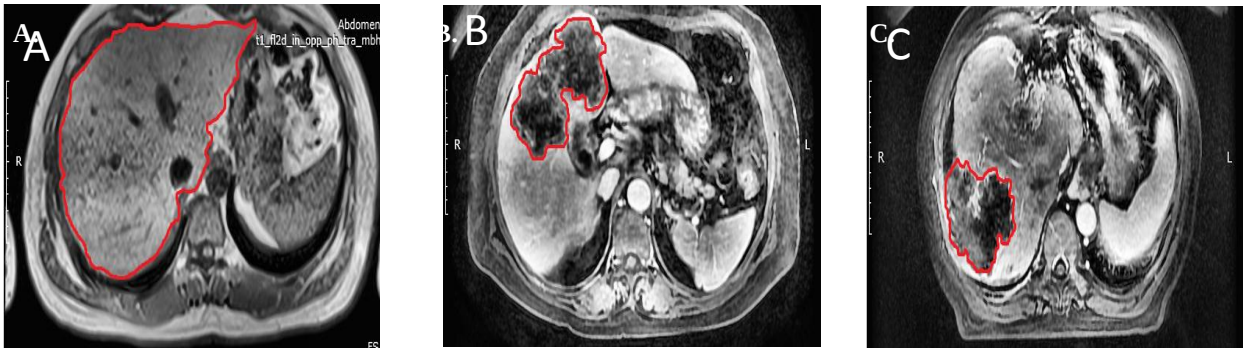

Figure 5.7. RED marked the region as the liver section or the liver sub-section tumor part in the CLAHE MR enhanced images. A. CLAHE enhanced MR Normal liver region marked. B. MR HCC marked of the CLAHE enhanced liver portion region. C. MR MET marked of the CLAHE enhanced liver portion region.

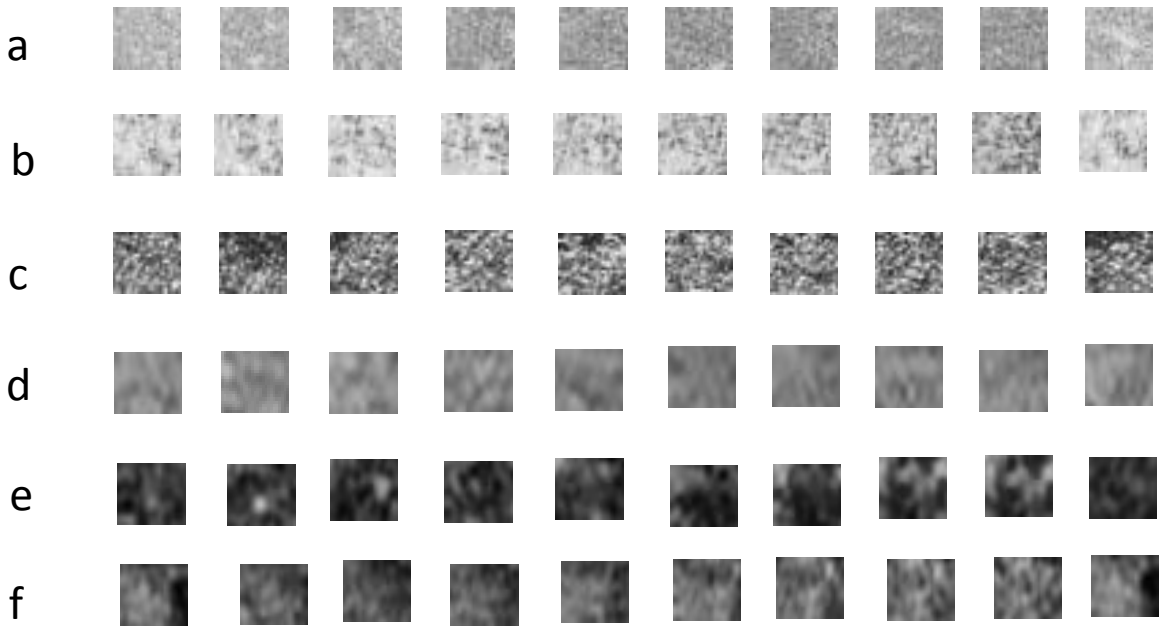

Figure 5.8. 10 ROI samples a. Normal CT liver b. CT HCC liver c. CT MET liver d. Normal MR liver e. MR HCC liver f. MR MET liver.

Figure 5.4 represents the three original CT images of the patients. In the first image, the red marked is the ROI portion, the complete liver portion of the normal liver. In the second image, the red marked is the complete tumor portion of the HCC in the liver region. In the last images, the red marked is the complete tumor portion of the MET in the liver region. These are

the images taken from a particular series with a suitable size of the normal liver and the tumor portion present in the liver. Similarly, Figure 5.5 represents the three sets of the CLAHE enhanced CT original images to get a different look at our area of interest. In the second and the last figure of the tumor we get a clear look with the tumor from the other region in the liver portion of the complete image. Figure 5.6 represents the three original MR images of the patients. In the first image, the red marked is the ROI portion, the complete liver portion of the normal liver. In the second image, the red marked is the complete tumor portion of the HCC in the liver region. In the last images, the red marked is the complete tumor portion of the MET in the liver region. These are the types of a particular sample of the images taken from the series that have a suitable size of the normal liver and the tumor portion present in the liver. Similarly, Figure 5.7 represents the three sets of the CLAHE enhanced images of the original MR images to get a different look at our area of interest. In the second and the last figure of the tumor we get a clear look at the tumor from the other region in the liver portion of the complete image. Figure 5.8 represents the 10 samples of the ROI extracted from the enhanced normal liver and the tumor portion of both HCC and MET for all the types of CT and MR images.

5.4. Concluding Remarks

Study 3 has been discussed, related to all the CT and MR images for the experiments 6-10 using Gabor filters. The five scales and eight Orientation parameters are used to design the 40 different Gabor filters. Experiment 6 is about to consider all the CT and MR images combination to detect the tumor. It has the largest database among all the experiments to detect the tumor. Experiment 7 is about the detection of liver tumor cancer using MR images. Experiment 8 is about the detection of liver tumor cancer using the CT images. Experiment 9 is to classify the liver tumor using MR images. Experiment 10 is to classify the liver tumor using CT images. These experiments allow checking the experiment for the detection and classification using different medical domain CT and MR images and combining both.

Chapter 6

SEGMENTATION AND REGISTRATION

6.1. SEGMENTATION INTRODUCTION

The segmentation of images is utilized to place and determine objects and boundaries (lines, curves, etc.) in images. Normally, the main goal of dividing an image into subparts is based on some specific features. Features could be based on certain boundaries, contour, color, intensity or texture pattern, geometric shape or any other pattern. It generates an easier way to address and indicate an image. The image segmentation process comprises grouping parts of an image into units that are homogeneous with respect to one or more characteristics. The outcome of image segmentation is a set of segments that collectively cover the whole image, or a set of contours extracted from the image [106-108].

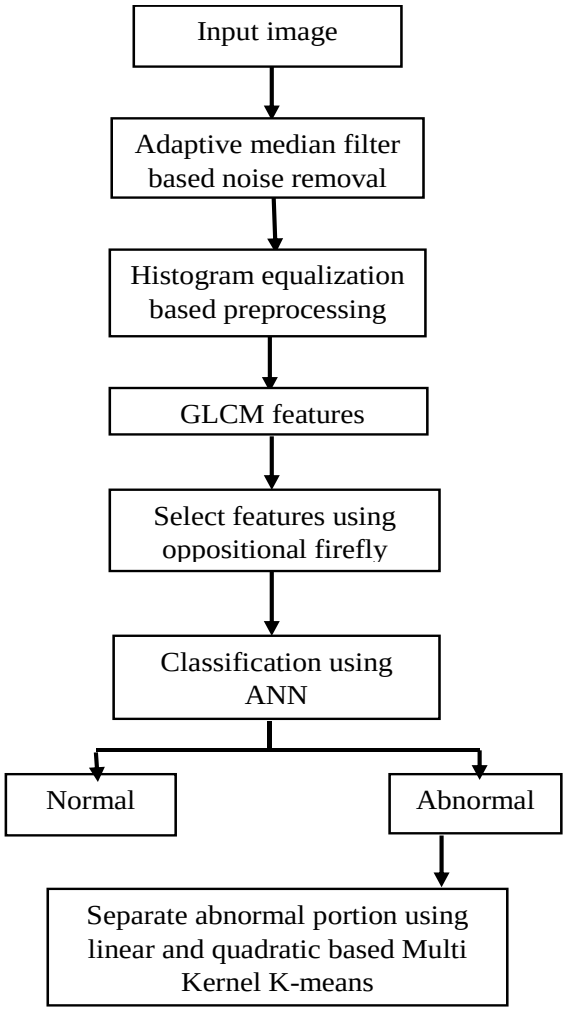

Figure 6.1. CT and MRI liver tumor classification and segmentation.

A noise removal process to remove the noise from the original CT and the MR images by using an adaptive median filter. It improves the image quality that improves the accuracy rate of the segmentation results. CLAHE used to enhance the contrast of the liver images. This preprocessing rectifying the data for irregularities and undesirable atmospheric noise removal of liver image [109]. After the pre-processing, there is calculation of GLCM features. The features are selected using oppositional firefly that seeks global optimization. It identifies food source from a wide range of fragrances floating all around and flies toward the corresponding place. The selected features are applied to the ANN classifier to classify the image as normal or abnormal. After that, the images are clustered using the optimal kernel K-means (OKK-means) clustering technique. The classification is to be performed with the aid of OKK-means clustering technique [110, 111].

6.2. ANN classifier

ANN is an interconnected group of nodes, simplification of neurons in a brain. ANN classifier allows each node, an artificial neuron. The layer that receives external data is the input layer as the input results in the form of the results after feature selection. The layer that produces the ultimate result is the output layer, to classify that is normal or abnormal. In between them are zero or more hidden layers. Between two layers, multiple connection patterns are possible.

6.3. Opposition Fruit Fly algorithm (OFA)

OFA is used for the feature selection method that simulates the foraging behavior of fruit flies. It seeking global optimization, it identifies food source from a wide range of fragrances floating all around and flies towards the corresponding place. After reaching close towards the food, it discover food or go to that particular place with its delicate vision. Food sources are referred by the optima and the methodology of foraging is reproduced by means of the iteratively seeking for the optima in the OFA [112, 113].

6.4. Multi Kernel K-means (MK K-means) Clustering

This algorithm allows the clustering with the multi class that allows the hybrid kernel K-means clustering algorithm. Kernel K-means clustering algorithm that maps data points from the input space to a feature space through a nonlinear performance and minimizes the cluster error in feature spaces. MK K-means clustering aims to optimally combine a group of pre-specified kernels to improve clustering performance [114-116]. This could result in selecting

mutually redundant kernels and affect the diversity of in- formation sources utilized for clustering [117, 118]. A lot of kernels are used such as radial basis function (RBF) kernel, linear kernel and quadratic kernel.

The individual kernel function formulas equation:

Gaussian RBF: $$k(p,q) = \exp(\frac{-\|p-q\|^2}{2\sigma^2}) \quad (6.1)$$

Linear kernel function:

$$K_1(p,q) = p^T q + c \quad (6.2)$$

Quadratic kernel function:

$$K_2(p,q) = 1 - \frac{\|p-q\|^2}{\|p-q\|^2+c} \quad (6.3)$$

The hybrid kernel K-means algorithm under kernelization of the metric approach is an iterative two-step algorithm that gives a partition P={P_1,…., P_K} of X into K clusters and their corresponding cluster centroids $Y_k \in R^P (K=1,\ldots\ldots, K)$ which minimizes the objective function;

$$W=\sum_{k=1}^{K}\sum_{x_i\in P_k}\|\varphi(x_i)-\varphi(y_k)\|^2 \quad (6.4)$$

$$=\sum_{k=1}^{K}\sum_{x_i\in P_k}\{K_{MK}(x_i,x_i)-2K_{MK}(x_i,y_k)+K_{MK}(y_k,y_k)\} \quad (6.5)$$

Where K_{MK} represents the hybrid kernel. Here, K_1 is the linear kernel and K_2 is the quadratic kernel.

$$K_{MK}(p, q) = K_1(p, q) + K_2(p, q) \quad (6.6)$$

The kernel-based objective function is represented below:

$$W=\sum_{k=1}^{K}\sum_{x_i=P_k}(1-K_{MK}(x_i,y_k)) \quad (6.7)$$

The choice of optimal method for segmentation

A lot of clustering algorithms are used for segmentation. Among them, one of the most popular clustering algorithms is the K-means algorithm, where groups are identified by minimizing the clustering error defined as the sum of the squared Euclidean distances between each data set point and the corresponding cluster center. This algorithm suffers from two serious limitations. First, the solution depends heavily on the initial positions of the cluster centers, resulting in poor

minima, and second, it can only find linearly separable clusters. To overcome the problem, the kernel K-means clustering algorithm is implemented. Kernel K-means is an extension of the standard K-means, an algorithm that maps data points from the input space to a feature space through a nonlinear transformation and minimizes the clustering error in feature space. Thus, non-linearly separated clusters in the input space are obtained, overcoming the second limitation of K-means. To improve the proposed segmentation accuracy, we introduced the hybrid kernel K-means clustering algorithm. Nowadays a lot of kernels are used such as radial basis function kernel, linear kernel and quadratic kernel. Among them, in this proposed work, we hybridize the linear and quadratic kernels. This proposed multi-kernel K-means cluster algorithm is termed as OKK-means cluster algorithm in this work. In the algorithm, once the centroid is updated for every cluster, the next step is to calculate the distance between the centroid and the data point. Each data point is assigned to a cluster center whose distance is minimum. This process is repeated until the updated centroid of each cluster is similar in consecutive iterations.

6.5. REGISTRATION INTRODUCTION

Registration is an essential preprocessing step, merging useful information from two or more images into a single, more informative image that will assist both the surgeons and the radiologist type for their planning and monitoring of the therapy. Registration is the process to match the images that captured in different conditions, different phases, have a difference of delay and have different specifications, of the same patient. Image registration attempts to find the best spatial correlation between two or more images (reference and sensed) of the same scene that was captured in a single / multi-view format at different time frames, or with similar/different modalities [119, 120]. Medical image registration between different images or different modalities is very effective for comprehensive and precious diagnosis and treatment. CT images registered spatially by using the mutual image (MI). Maximization of mutual information (MMI) using the images of different organs. Visualization of the registration results on the large classes shown the excellence of the MMI registration. Its impact on each local deformation within its region of support. Relatively large regions in the registration desirable for the local MI estimate. Registration algorithms directly vary with a strong correlation between the images being used as the inputs [121]. For the multi-phase liver images, that have the tumor portion the liver registration may be useful to get the MI among them. A liver image registration

algorithm initially converted the images with similarity into the vessel probability (from seed position to the neighboring voxels probability) images that yield maximization with the normalized cross-correlation value [122]. Similarly, measure results in maximum range for the closely aligned images, depend mostly on intensity values. With their similarity measures, that quantifies an average distance between their correspondence surfaces [123].

This is the registration of the multi-phase CT images of the same patient. The multi phases are the arterial phase, venous phase, and different delayed phases. These phases' registration helps out with the MI from the images from that phase. With this experimentation, the radiologist should allow getting more different phases data to get more and more information with the data records. Combining multi-phase CT image information from the different classes of phase will improve the information acquired. This is the development of an algorithm for multi-phase CT images registration to extract more information from the images for the early diagnosis of liver cancer based on arterial phase, venous phase and the delayed phases. These different phases have experimented with the two images as the inputs from the different series.

The registration technique is the optimization technique in which the parameters represented by the floating images are iteratively transformed with respect to the reference image that maximized the similarity measures.

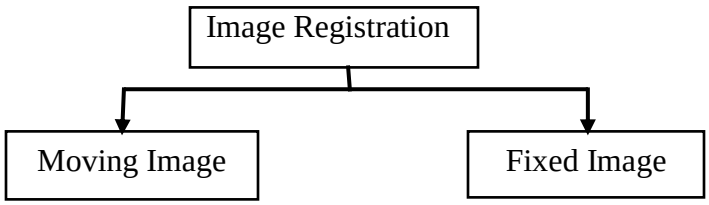

Figure 6.2. Basic block diagram to do the image registration process.

One image could be approximated for the registration in terms of the other image by applying various algorithms. The output registered image analysis, the patient having multiple images by some geometrical correspondence or known registration between them.

The position of the fiducial markers determined by an active pointer associated with the s patial tracking system. The images placed with their centers coincide and are aligned with the cor responding images and have the same orientation. Two images with the same dimensions are required for image registration, having the same width and thickness level. For the reference image, the image is preferred that has just one scan, or in case of both images that have delayed, the images that have less delayed time should be the reference image. Radiologists visualize the registration standard using anatomical landmarks. The extracted features are locations with respect to medical axis points. Each image location has image coordinates and vessel orientations and widths to meet the desired input information. The following algorithm provides a complete way to perform this function or task.

Algorithm

- **a.** All the slices present in the sequence are of the same patient.
- **b.** The two images are selected with all the same dimensions (height and the width) in different specifications and the delayed phase.
- **c.** For a fixed image and moving image, images are used to measure their features that register images.
- **d.** Calculation of the features with the detected and the matched values.
- **e.** The resulted images are designed with the difference of the two images using different colors.
- **f.** The resulted output images have the findings for the difference between the color and the same part with the normal intensity.
- **g.** The images having the large tumor and the liver size are useful results with their detected and the matched values.

Extraction of features may introduce new geometrical errors, require additional computation time and may be specific to the modality or application, making automation more difficult. In this study, the features computed with the registrations are:

6.5.1. Maximally stable extreme regions (MSER)

MSER used as the type of blob detection and that is the region detected in the images. From two images it finds the correspondence between image elements of different viewpoints. MSER defined as the region detector to improve performance in matching image elements.

$$\Psi(R_i^g) = (\left|R_i^{g-\Delta}\right| - \left|R_i^{g+\Delta}\right|)/|R_i^g| \qquad (6.8)$$

Stability, Ψ of the region, R_i is the connected region, R_i^g is the region detected by applying a threshold on a gray value g, Δ is the stability factor, $R_i^{g-\Delta}$and $R_i^{g+\Delta}$ are the extremal regions located above and under the region R_i^g.

6.5.2. Speeded up robust Features (SURF)

SURF calculated with a large value that has the most coincidence and a large number of matching's with the intensity levels in the images. This defines the feature information with the pixel intensity distribution, with the points of interest in the neighborhood. A short descriptor could be more robust. SURF uses a blob detector based on the Hessian matrix to find points of interest. The determinant of the Hessian matrix is used as a measure of local change around the point and points are chosen where this determinant is maximal. SURF also uses the determinant of the Hessian for selecting the scale. Given a point p=(x, y) in an image I, the Hessian matrix H (p, σ) at point p and scale σ, is:

$$\text{Hessian Matrix, } H(p,\sigma) = \begin{bmatrix} L_{xx}(p,\sigma) & L_{xy}(p,\sigma) \\ L_{yx}(p,\sigma) & L_{yy}(p,\sigma) \end{bmatrix} \qquad (6.9)$$

where $L_{xx}(p,\sigma)$ etc. is the convolution of the second-order derivative of Gaussian with the image *I(x, y)* at the point *p*.

The following table is the data table of the multi-phases

Table 6.1. The phase number details with their specifications that are used as the input images with the experiments.

Multi Phases	**Description**
1.	Triple phase CT
2.	Arterial phase
3.	Venous phase

4.	Delayed
5.	Delayed 10 Min.

The experiments are designed, with the selection of the images from the multi-phases, one as the fixed image and the second image as the moving image. The series in different phases, with delayed or more delayed phases used as the moving image. The experiments are designed in such a way that we have a total number of 10 experiments from the five multi-phase series.

Table 6.2. The detailed table of the experiments with the description of the fixed image and the moving image.

Experiment No.	Fixed Image	Moving Image
1	Triple phase CT	Arterial phase
2	Triple phase CT	Venous phase
3	Triple phase CT	Delayed
4	Triple phase CT	Delayed 10 Min.
5	Arterial phase	Venous phase
6	Arterial phase	Delayed
7	Arterial phase	Delayed 10 Min.
8	Venous phase	Delayed
9	Venous phase	Delayed 10 Min.
10	Delayed	Delayed 10 Min.

The MSER and SURF features are calculated from the image registration process, with projective transformation, that is done to convert a 3-D image to the 2-D image as a perspective distortion and the two sets of values as the identified values and one set of value as the matched value for all the registration results in both the features. The post-processing has done using rotation as non-rigid transformation using 100 iterations, three pyramid levels, and 1.0 smoothing. The number of iterations value is the number of iterations on each pyramid level. The pyramid level value represents the number of Gaussian pyramid reduction levels. The maximum number of pyramid levels depends on the size of each dimension in the images. The smoothing

value is the standard deviation of Gaussian smoothing and remains the same at each pyramid level in the range [0.5, 3]. Larger values result in smoother output displacement fields. Smaller values result in more localized deformation in the output displacement field. The corresponding registration images are helpful in providing useful information with the large tumor size and the large liver size.

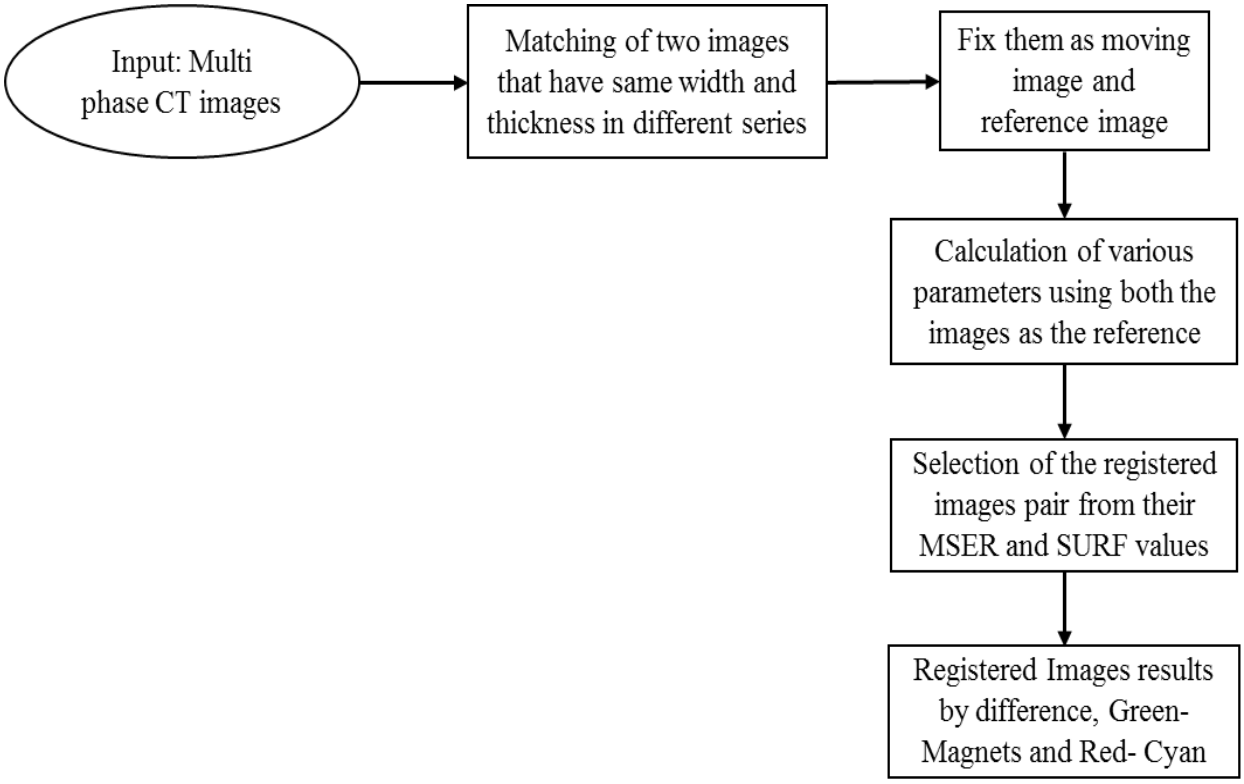

Figure 6.5. The flowchart representation of the complete processing with the experiments.

6.6. Concluding Remarks

The segmentation and registration work has been discussed. For the segmentation, the CT and MR images segmented into several regions. The classifier used to classify those parts into suitable regions. The feature selection used to do the optimum seeking and clustering to combine and improve the clustering results. For the registration, the multi-phase CT images used as the input. The features are extracted, with the combined image registered. The registered images are in different combinations, with some post processing work.

Chapter 7

RESULTS AND DISCUSSIONS

The results are calculated from the extracted features, application of feature selections, and applying various classifiers. The results are expressed by the various types of performance measures:-

7.1. Performance measures

7.1.1. False-positive rate (FPR): It is the ratio of the wrongly categorized negative sample as positive (false positive) to the total number of actual negative samples (irrespective of classification)

$$\text{FPR}=\frac{FP}{FP+TN} \tag{7.1}$$

7.1.2. False negative rate (FNR): It is the ratio of the wrongly categorized positive sample as negative (false negative) to the total number of actual positive samples (irrespective of classification)

$$\text{FNR}=\frac{FN}{FN+TP} \tag{7.2}$$

7.1.3. Positive predictive value (PPV): The probability of having the state/disease of the subject interest with a positive result (B+|T+). It is the proportion of the patients with positive test results in the total subjects from the positive results.

$$\text{PPV}=\frac{TP}{TP+FP} \tag{7.3}$$

7.1.4. Negative predictive value (NPV): The probability of not having a disease with the subject has a negative test result (B-|T-). It is the proportion of subjects without the disease with a negative test result in the total subjects from the negative results.

$$\text{NPV}=\frac{TN}{TN+FN} \tag{7.4}$$

7.1.5. Sensitivity: The sensitivity measure is the proportion of the actual positives that are accurately recognized. It correlates with the testing capacity to recognize positive results.

$$\text{Sensitivity}=\frac{TP}{TP+FN} \tag{7.5}$$

7.1.6. Specificity: The specificity measure is the extent of the negatives that are properly recognized. It correlates with the testing capacity to recognize negative results.

$$\text{Specificity}=\frac{TN}{TN+FP} \tag{7.6}$$

7.1.7. Accuracy: It is the ratio of the total number of TP and TN to the total number of data.

$$\text{Accuracy}=\frac{TN+TP}{TN+TP+FN+FP} \tag{7.7}$$

7.1.8. Precision: It is similar to the positive predictive value:

$$\text{Precision}=\frac{TP}{TP+FP} \tag{7.8}$$

where,

TP: True positive, **TN:** True negative, **FP:** False positive, **FN:** False negative

The TP, TN, FP, and FN for the segmentation of normal and abnormal for liver MRI and CT scan image is specified in Table 7.1.

Table 7.1 Truth table for the experimental outcome.

Experimental outcome	**Condition is determined by the standard of truth**	
	Positive	**Negative**
Positive	TP	FP

Negative	FN	TN

7.1.9. Area Under Curve (AUC):

The AUC is the measure of the ability of a classifier to distinguish between classes. It's of excellent quality if its value is near one. The higher the AUC, the better the performance of the model at distinguishing between the positive and negative classes [127]. The present work is carried out in different parts of the CT and MR image processing, so their results are described here:-

7.2. Pre-processing

For the pre-processing, two enhancement algorithms CLAHE and CVHE have been discussed. The GLCM features have been extracted using both the enhancement algorithm. The CLAHE algorithm have a better performance in comparison of CVHE algorithm.

The choice of optimal method for enhancement has been done after performing evaluation of enhancement methods using both subjective and objective criteria. On the basis of literature review and experimental run-on various enhancement methods, two enhancement methods, viz., CLAHE and CVHE, were chosen. A set of CT/MR images after enhancement by these two methods were shown to radiologist to provide their expert opinion. He provided subjective score, 1-5 for each enhanced image. The score ‘1’ indicate the lowest side in providing the improved textural contrast on enhanced images in comparison to original one, whereas ‘5’ indicate the highest side. This subjective evaluation was in favour of CLAHE enhancement method.

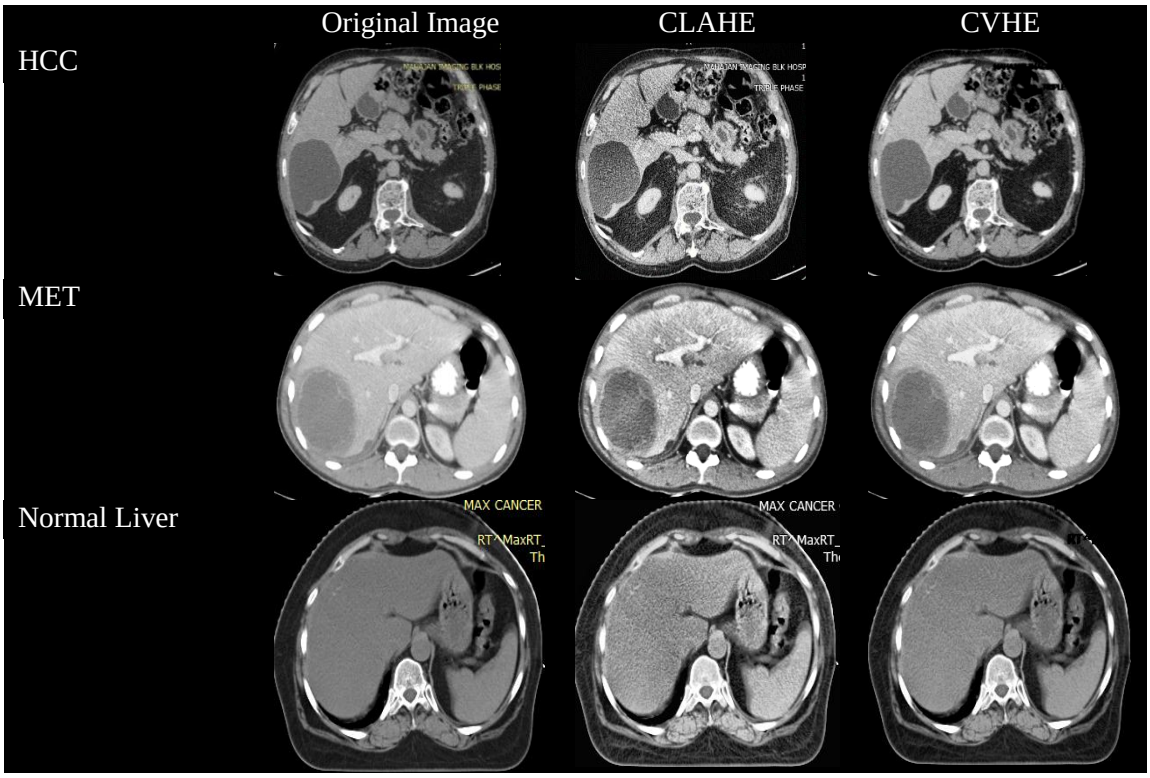

Figure 7.1: The sample images of the original image, CLAHE enhanced and CVHE enhanced for the HCC, MET and the normal liver.

In the objective criterion, 12 second order textural features using Gray level co-occurrence matrix were evaluated on enhanced images from both the methods. It can be clearly seen with the box-plots of contrast and correlation features among normal, HCC and MET ROIs provide higher discrimination using CLAHE enhancement method than that of CVHE. Therefore, CLAHE method has been chosen for enhancement of images having better score with both the subjective and objective criteria.

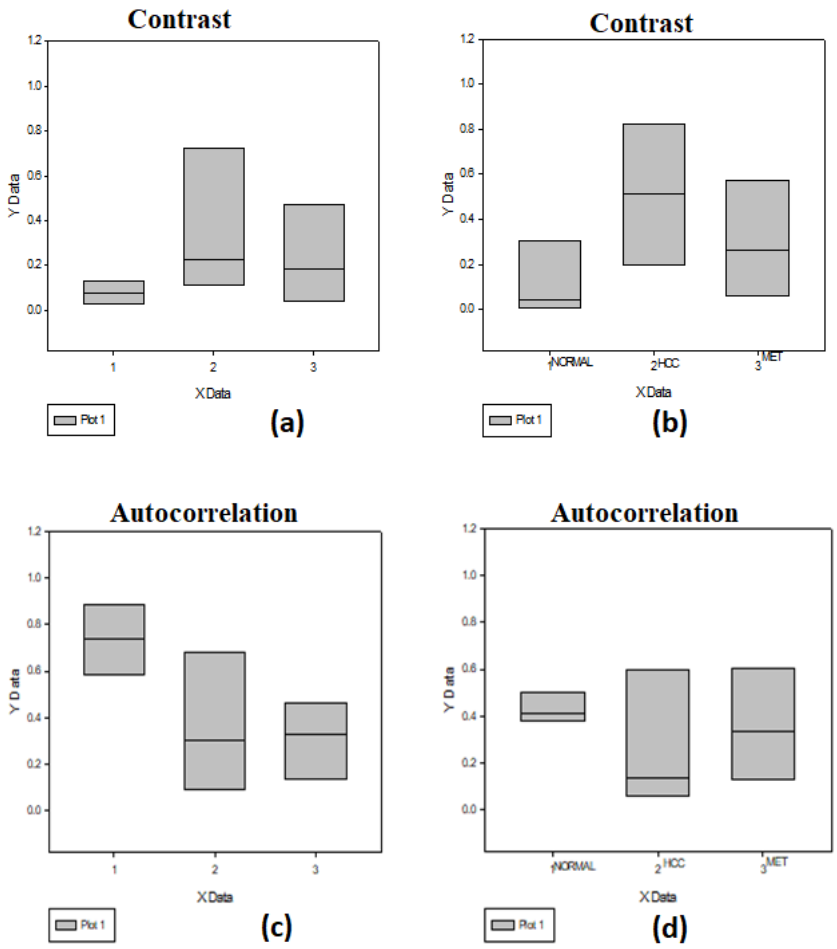

Figure 7.2 (a –d) the box plot results comparison of CLAHE and CVHE enhancement algorithm. The box plot represents a comparison of Normal liver, the HCC and the MET using the CLAHE and CVHE algorithm, respectively. The range of a particular parameter is compared between both the algorithms.

Figure 7.2 (a-d) represents a clear difference of the range of the normal liver, HCC and the MET results in terms of contrast and auto-correlation, respectively. These results have a box with each record. The uppermost layer represents the 100 percentile records, the middle layer represents the 50 percentile records, and the last layer represents the lowest level of the percentile.

7.2. STUDY 1

CT image processing

The CT image processing experimentation has two parts: one to check the classifier rate of IROI features and the other with the ratio features. For the classification, in Experiment-1, all

the extracted features were included, 97% accuracy, 94.3% sensitivity, and 100% specificity is obtained. In Experiment-2 for the classification, only ratio features were included, the classifier obtained 84% accuracy, sensitivity, and specificity each. In Experiment 1 if we consider, the feature extracted from FOS, GTDM, and GLCM, the obtained 94.5% maximum accuracy, 91.2% maximum sensitivity, and 97.8% maximum specificity. For experiment 2 using the ratio features extracted from FOS, GTDM, and GLCM, the classifier obtained 83% maximum accuracy, 82.4% maximum sensitivity, and 83.7% maximum specificity.

GA has been utilized as a feature selector, on IROI extracted features. It selects 20, 15, 10, 5 IROI features for experiments 3A, 3B, 3C, 3D, and the maximum accuracy is 96.5%, the maximum sensitivity 95.1%, and the maximum specificity of 97.9% is obtained. Similarly, GA has been applied on ratio features it selected 20, 15,10,5 ratios for the experiments 4A, 4B, 4C, 4D the maximum accuracy 79%, the maximum sensitivity 80.9%, and the maximum specificity of 77.4% is obtained. For experiments 3A and 4A, the best 20 features are selected. For experiments 3B and 4B, the best 15 features are selected. For experiments 3C and 4C, the best 10 features are selected. For experiments 3D and 4D, the best 5 features are selected.

From the IROI classification experiments results, the overall classifier rate that contains all the features yields the highest classifier accuracy rate. The sub experiments accuracy varying from 88%-94.5%, sensitivity varying from 79.3%-91.2%, and specificity varying from 91.3%-97.8%. 88% classifier accuracy, 85.2% sensitivity, 91.3% specificity is obtained from GTDM extracted features, and 94.5% accuracy, 91.2% sensitivity, and 97.8% specificity are obtained from FOS extracted features. The other types of GLCM extracted features have a classifier accuracy of 90%, a sensitivity of 79.3%, and a specificity of 97.6%. Using GA as feature selection, there is a maximum variation of 1% accuracy, 0.9% sensitivity, and 2.9% specificity from all the sub-experiments as mentioned in Table 7.2.

For the ratio features, the overall classifier rate yields the maximum classification 84% accuracy. GTDM ratios has classification 72% accuracy, 73.4% sensitivity and 70.8% specificity. GLCM ratios has classification 76% accuracy, 75% sensitivity and 77.1% specificity. FOS has classification 83% accuracy, sensitivity 82.4% and 83.7% specificity. For various sub-experiments, the classification accuracy varies from 72%-83%, sensitivity varies from 73.4%-82.4% and specificity varies from 70.8%-83.7%. Using GA as feature selection, there is a

variation of 5.5% accuracy, 7.7% sensitivity, and 4.6% specificity with all the sub-experiments as mentioned in Table 7.2.

For the IROI, the maximum number of features yields better accuracy in comparison to all the other sub-experiments, in all the experiment containing the maximum numbers of features has more classifier rate. For the ratio features, the classification accuracy yields less in comparison to the IROI feature value. But in these experiments also, the maximum classifier accuracy yield overall contains features. In the GA feature selection ratio features, the classification accuracy is decreasing linearly as the numbers of features are decreasing as mentioned in Table 7.2.

Table 7.2 Experiment with features description sensitivity and specificity results

Experiment No./ Features	**Sensitivity (%)**	**Specificity(%)**	**Accuracy (%)**
1.	94.3	100	97
1(FOS)	91.2	97.8	94.5
1(GTDM)	85.2	91.3	88
1(GLCM)	79.3	97.6	90
2	84	84	84
2(FOS)	82.4	83.7	83
2(GTDM)	73.4	70.8	72
2(GLCM)	75	77.1	76
3(20)	94.2	97.9	96
3(15)	95.1	97.9	96.5
3(10)	94.3	98.9	96.5
3(5)	95.1	96	95.5
4(20)	80.9	77.4	79
4(15)	80.9	74.8	77.5
4(10)	76.6	73.6	75

4(5)	74.2	72.8	73.5

The validation experiment is performed on the testing data set. The IROI value experiments perform a consistent performance classification rate. For all IROI feature values experiment 1 and 3, yield satisfactory results with overall and by feature selected experiments as shown in Figure 7.2 A and Figure 7.2 C. In experiment 1, all the features in experimentation resulted in the highest classification accuracy. For all sub-experiments of Experiment-3, there is a small deviation in the classification accuracy among the selected features. The accuracy and sensitivity have a constant level with the variation in the number of features. The specificity decreases linearly with the number of features varying from 15 to 5. The five-fold Cross-Validation (CV) has also been performed to verify the robustness of the features classifier, it varies with 1%-1.2% overall.

Figure 7.3. Validation of IROI feature values result for the classification accuracy, sensitivity, and specificity for experiments **A.** Experiment 1, 1(FOS), 1(GTDM), 1(GLCM) **B.** Experiment 2, 2(FOS), 2(GTDM), 2(GLCM) **C.** Experiment 3A, 3B, 3C, 3D. **D.** Experiment 4A, 4B, 4C, 4D.

The validation of experiments 2 and 4 were also performed with the testing data. The ratio features have better results performance in direct classification. The highest accuracy is obtained with all the features. The accuracy, sensitivity, and specificity have the same variation, as shown in Figure 7.3 B and Figure 7.3 D. Using GA as feature selection experiments, the testing yields better results with more number of selected features. The ratio features using GA decreases linearly with the number of features in accuracy and sensitivity. The five-fold CV has

also been performed to verify the robustness of the features classifiers, it varies with 1% overall**.** Ratio features values testing data also performed well results on feature tested values.

7.3. STUDY 2

EXPERIMENT 5

This work is associated with the classification of liver cancer diseases with their category, which is primary cancer and secondary cancer. That allows us to get the details of the liver cancer disease classes' information regarding the type of diseases concerning their origin. It helps in diagnosing the type of cancerous diseases according to their classes. The further classification of the type of liver cancer disease allows assisting the radiologist to provide the diagnosis information details with their classes. This present work allows us to get a new approach in the liver disease classification categories and forgetting the classification results with detection and classification, by using multi classifiers ensemble process to improve the classification results.

This work aims to identify and classify tumors in a specific category. Improved images result in the clear appearance of a tumor with varying degrees of intensity as their identification. The identification mark is a continuation of the sections that help in the detection of the tumor to save the time of the radiologists and to obtain information on the size of the tumor by visualizing only those images. Tumors are classified as primary and secondary by class; the radiologist helps with early information on the type of tumor. Before starting treatment, doctors save valuable time and start treatment earlier after obtaining valuable information about the tumor.

To detect the tumor, there is a classification between normal and abnormal CT images with non-tumor and tumor portion regions. There are a total of six classifiers to test the accuracy rate variation for the detection of the tumor in the CT images. The following two tables represent the results of the classifier to detect the tumor and classify the tumor class in the percentage accuracy rate and the change of the rate of AUC for the same in detection and classification using the same six classifiers.

Tables 7.3 show the performance of classifiers for the classification of the tumors and the variation of the values of the AUC. Figure 7.4 shows the validation of the detection accuracy, classification accuracy, and the AUC value of the classification. Figure 7.5 shows the k-cross-

validation of the ensemble model. The variation in classification accuracy with 87.91%, 87.33%, 88.98%, 86.67%, and 85.58% for the different fold values. There is a total variation of 3.4% with the maximum and minimum accuracy results, which allows checking the robustness of the proposed model.

Tables 7.3 shows the performance of classifiers for the classification of the tumors and the variation of the values of the AUC.

The choice of optimal method for Classification

Initially for the detection and classification of liver cancers, six different classifiers were chosen. These classifiers were AdaBoost, support vector machine, neural network, R part decision tree, generalized linear model and random forest. The evaluation of these classifier in the detection (normal and abnormal liver) and classification (HCC and MET) of the tumors has been done in terms of classification accuracy and ROC as show in the table below:

Table 7.3 Classifiers accuracy percentage and AUC of all the classifiers to detect and classify the tumor.

Classifiers Type	**Detection** (normal and abnormal liver)		**Classification** (HCC and MET)	
	Accuracy (%)	**AUC**	**Accuracy (%)**	**AUC**
Decision Tree	98.66	0.99	79.53	0.87
Adaboost	99.19	1	84.65	0.95
RF	98.66	1	86.22	0.98
SVM	100	1	87.01	0.94
GLM	98.66	1	87.01	0.96
NNET	98.39	0.99	76.38	0.77
Ensemble	100	1	88.98	0.99

The ensemble of all the classifiers allows to get a better classifier rate in comparison of all of them individually.

We are getting close to 100% using individual classifiers in the experimentation for detection of liver cancer diseases only, not for the classification of liver cancer. The classification accuracy of the individual classifiers is less as compare to ensemble mode for liver cancer classification. Thus ensemble classifier performs better in both the cases of disease detection as well as classification.

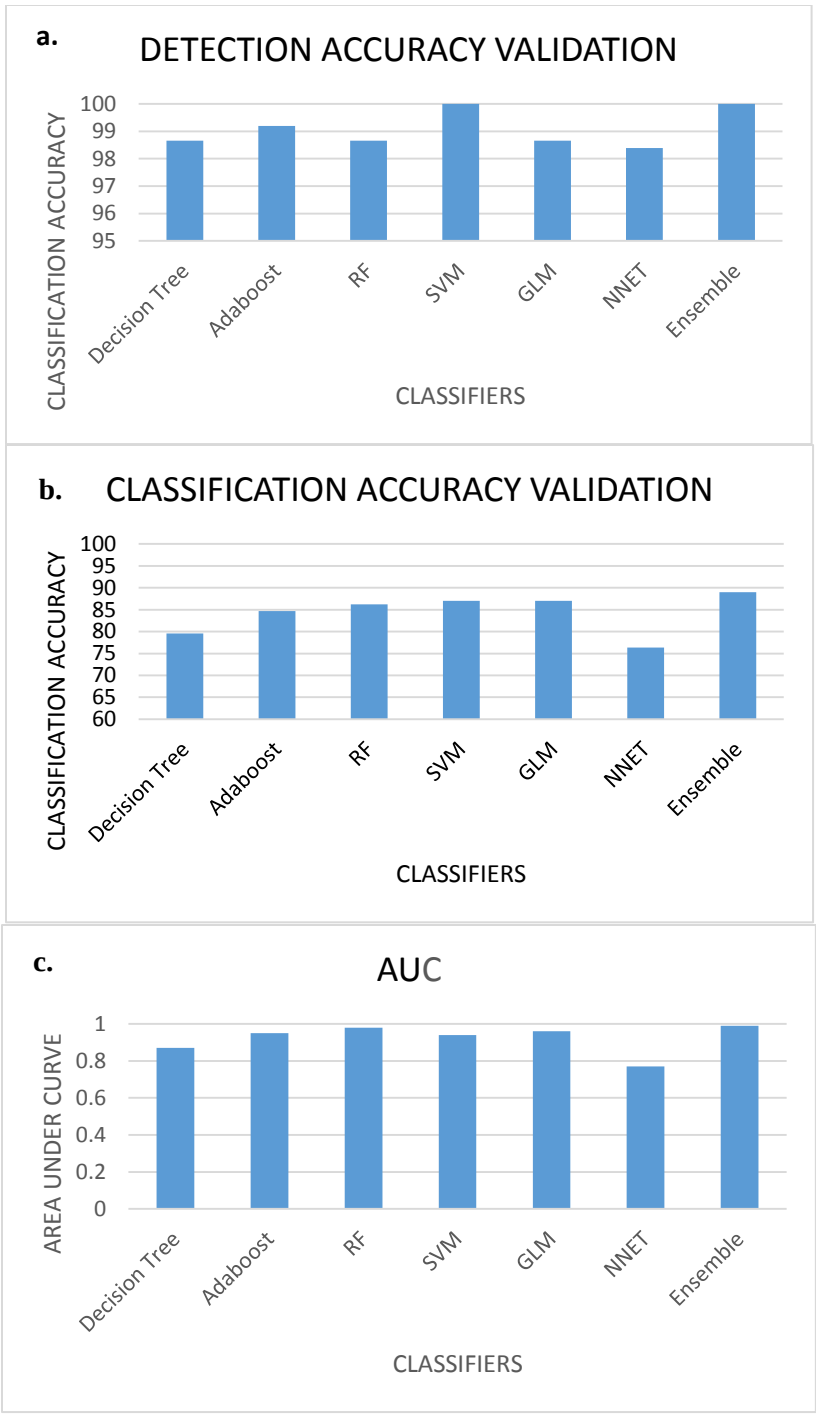

Figure 7.4 a. For detection. b. For classification. c. AUC value. Validation of the ROI evaluated feature to check their accuracy rates and the variation of AUC in tumor classification using six classifiers.

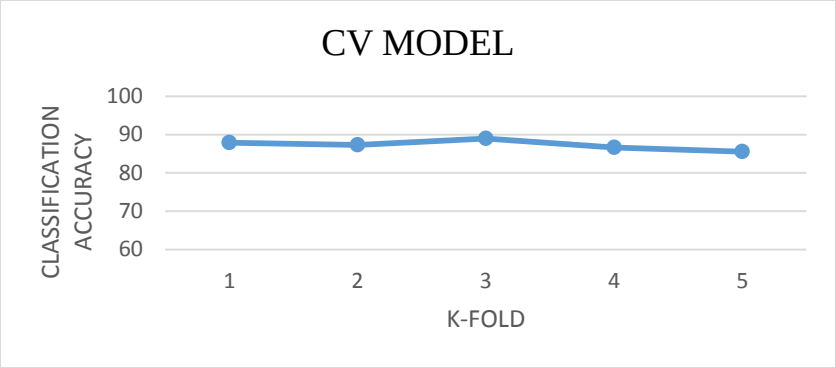

Figure 7.5 k-Fold cross-validation (CV) to check the accuracy variation with the model for the classification of liver cancer diseases.

7.4. STUDY 3

CT and MR image processing using Gabor Filter

The Gabor filter parameters are calculated using scaling and orientation parameters. The scale and orientation parameters are designed, with the group classes of scaling and orientation of the images varying differently.

Table7.4 Evaluation of various performance measures using different classifiers in various experiments.

Experiment No.	Classification	Accuracy	AUC	Sensitivity/ Specificity	Precision
6. 1957 abnormal images of CT and MR 2609 normal images of CT and MR	Decision tree	72.34	0.72	0.7/0.75	0.63
	Ada Boost	79.2	0.77	0.78/0.76	0.63
	RF	80.29	0.78	0.78/0.79	0.69
	SVM	79.64	0.8	0.82/0.77	0.64
	GLM	74.89	0.74	0.76/0.74	0.58
7. 1054 abnormal images of MR 2274 normal images of MR	Decision tree	77.08	0.5	0.5/0.5	0.30
	Ada Boost	80.58	0.79	0.78/0.81	0.6
	RF	81.48	0.8	0.79/0.83	0.64
	SVM	81.58	0.84	0.82/0.85	0.62
	GLM	79.58	0.76	0.72/0.8	0.6

8. 844 abnormal images of CT 395 normal images of CT	Decision tree	90.05	0.89	0.82/0.96	0.92
	Ada Boost	94.89	0.96	0.92/1	1
	Random forest	94.62	0.96	0.92/0.99	0.98
	SVM	97.31	0.99	0.98/1	1
	GLM	90.32	0.9	0.85/0.95	0.89
9. 600 HCC images of MR 513 MET images of MR	Decision tree	69.29	0.74	0.71/0.76	0.86
	Ada Boost	72.05	0.72	0.77/0.69	0.74
	RF	72.05	0.71	0.76/0.67	0.73
	SVM	75.2	0.73	0.72/0.74	0.84
	GLM	68.9	0.67	0.69/0.66	0.78
	NN	70.87	0.67	0.71/0.64	0.74
10. 361 HCC images of CT 483 MET images of CT	Decision tree	67.67	0.71	0.73/0.7	0.72
	Ada Boost	74.85	0.71	0.71/0.72	0.8
	RF	72.16	0.73	0.74/0.72	0.78
	SVM	71.16	0.7	0.7/0.71	0.8
	GLM	69.16	0.7	0.71/0.7	0.78
	NN	70.36	0.76	0.75/0.78	0.86

Table 7.4 shows the calculated values of the different performance measures using various classifiers in all the experiments. The various performance measures are accuracy, AUC, sensitivity/specificity ratio, and precision. The experimentations are done in such a manner that in the form of tumor detection for the entire CT images, the MR images, and the combination of both of them. The two experiments are designed to classify the type of tumor for the CT images and the MR images. In these two experiments, there is one more classifier used as NN to check their classifier rate for more variation. Table 7.4 represents the classifier rate of the testing data which is selected as 30% of the total data. The total data is divided into 70% training data and 30% testing data. The testing data is selected to test the data. The accuracy is calculated to check the correctness of the classifier. The values presented are the percentage accuracy, that how

much percentage is there that is correctly diagnosed. The resulted values of accuracy have more accuracy in tumor detection in comparison to tumor classification because of more tumor intensity variation. The sensitivity/specificity ratio is the ratio of testing capacity that identifies the positive results that identify the negative results. The ratio of the actual positives correctly identified classifiers results in the identification of the negative results. The precision value is the positive predictive value. Its maximum value is 1, the value that comes is nearer to one is more relevant to the desired problem. It takes all the retrieved records, those outcomes according to the problem. It is the ratio of the correct result values to all the returned result outcomes.

The designed 40 images from the Gabor filters should have the appropriate scaling and orientation ratings. That calculated values are processed to the various classifiers to detect the tumor and to classify that in a specific category for a particular experiment. The number of classifiers used here is to compare the detector and the classifier rate and to check their variation. There are various performance measures: accuracy, sensitivity, specificity, AUC, and Precision. For the performance of the model, a large number of comparisons have been done using K-fold cross-validation (CV). The CV has been done for all the five/six classifiers to check their detector/classifier rate. It may be possible that this is repeating five times to check their robustness for the best classifier. The CV has been done for accuracy and the AUC, as these performance measures represent a unique identification with the results.

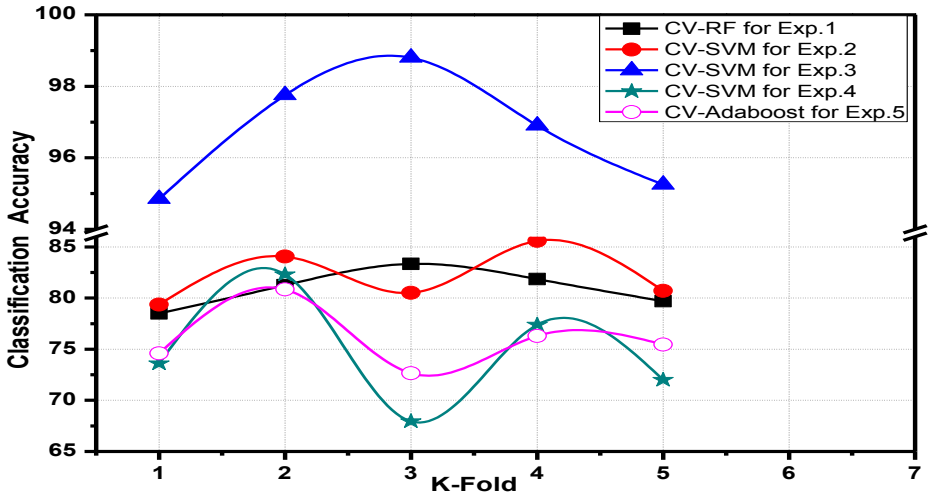

Figure 7.6 (a)

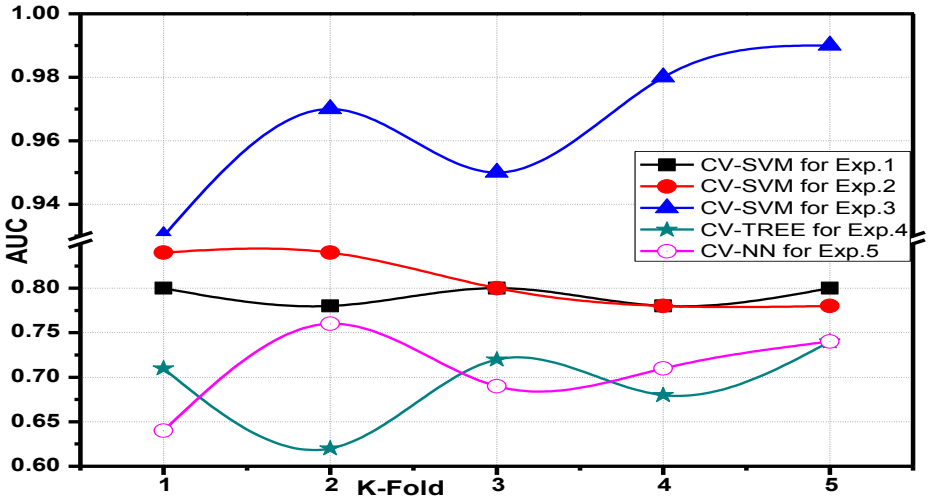

Figure 7.6 (b)

Figure 7.6 K-Fold cross-validation (CV) of the experiments that result in best classification accuracy and AUC.

The CV has been done for the accuracy and the AUC to check their consistency level of results with the best classifier results. For the classification accuracy as shown in figure 7.6 (a), in experiment 1, the classifier rate is RF, in this tumor detector rate varies from 78.5%-83.35%. The RF detector accuracy rate in the first case is 78.5%, in the second case, it increases to 81.25%, in the third case it increases to 83.35%, in the fourth case, it decreases to 81.85%, and in the last case, it decreases to 79.7%. In this accuracy, the highest classifier rate for this particular classifier to detect the tumor is 83.35%. In experiment 2, the classifier rate is SVM, in this tumor detector rate varies from 79.35%-85.6%. The SVM detector accuracy rate in the first case is 79.35%, in the second case it increases to 84.05%, in the third case it decreases to 80.5%, in the fourth case, it increases to 85.6%, and in the last case, it decreases to 80.7%. In this accuracy, the highest classifier rate for this particular classifier to detect the tumor is 85.6%. In experiment 3, the classifier rate is SVM, in this tumor detector rate varies from 94.85%-98.8%. The SVM detector accuracy rate in the first case is 94.85%, in the second case it increases to 97.75%, in the third case it decreases to 98.8%, in the fourth case, it decreases to 96.9%, and in the last case, it decreases to 95.25%. In this accuracy, the highest classifier rate for this particular classifier to detect the tumor is 98.8%. In experiment 4, the classifier rate is SVM, in this tumor detector rate varies from 67.95%-82.3%. The SVM classifier accuracy rate in the first case is 73.6%, in the second case it increases to 82.3%, in the third case it decreases to 67.95%, in the fourth case, it

increases to 77.4%, and in the last case, it decreases to 72%. In this accuracy, the highest classifier rate for this particular classifier to classify the tumor is 82.3%. In experiment 5, the classifier is AdaBoost, in this tumor detector rate varies from 72.65%-80.85%. The AdaBoost classifier accuracy rate in the first case is 74.6%, in the second case it increases to 80.85%, in the third case it decreases to 72.65%, in the fourth case, it increases to 76.3%, and in the last case, it decreases to 75.45%. In this accuracy, the highest classifier rate for this particular classifier to classify the tumor is 80.85%. Overall, all the experiments, with the best classifiers work on fivefold result in consistency levels. In experiment 3, overall the SVM classifier results have better results with 98.8% have the best classifier rate.

For the AUC as shown in Figure 7.6 (b), in experiment 2, the classifier rate is SVM, in this tumor AUC varies from 0.78-0.8. The SVM classifier AUC in the first case is 0.8, in the second case it decreases to 0.78, in the third case it increases to 0.8, in the fourth case, it decreases to 0.78, and in the last case, it increases to 0.8. In this AUC, the highest for this particular classifier to detect the tumor is 0.8. In experiment 2, the classifier rate is SVM, in this tumor detector, AUC varies from 0.78-0.84. The SVM classifier AUC in the first case is 0.84, in the second case it remains the same to 0.84, in the third case it decreases to 0.8, in the fourth case, it increases to 0.78, and in the last case, and it remains the same to 0.78. In this AUC, the highest for this particular classifier to detect the tumor is 0.84. In experiment 3, the classifier rate is SVM, in this tumor detector, AUC varies from 0.93-0.99. The SVM classifier AUC in the first case is 0.93, in the second case it increases to 0.97, in the third case it decreases to 0.95, in the fourth case, it increases to 0.98, and in the last case, and it increases to 0.99. In this AUC, the highest for this particular classifier to detect the tumor is 0.99. In experiment 4, the classifier rate is TREE, in this tumor classifier, AUC varies from 0.62-0.74. The TREE classifier AUC in the first case is 0.71, in the second case it remains the same to 0.62, in the third case it decreases to 0.72, in the fourth case, it increases to 0.68, and in the last case, and it remains the same to 0.74. In this AUC, the highest for this particular classifier to classify the tumor is 0.74. In experiment 5, the classifier rate is NN, in this tumor classifier AUC varies from 0.64-0.76. The NN classifier AUC in the first case is 0.64, in the second case it remains the same to 0.76, in the third case it decreases to 0.69, in the fourth case, it increases to 0.71, and in the last case, and it remains the same to 0.74. In this AUC, the highest for this particular classifier to classify the tumor is 0.76.

Overall, all the experiments, with the best classifiers work on fivefold result in consistency levels. In experiment 3, overall the SVM classifier results have better results with 0.99 as the best AUC value.

7.5. SEGMENTATION

The performance analysis of the proposed method will be carried using the K-cross fold validation method. We compare our proposed OKK-means research results to the existing Regularized Distance Level-set (RDL). Our proposed medical image segmentation research achieves performance measures of 0.8775, 0.9891 and 0.9775 for sensitivity, specificity and accuracy, respectively. Here, we have given overall measures for 10 images that outperform the result of existing RDL method as shown in graphs below:

Table 7.5 Proposed evaluation measures for medical image segmentation

Cases (patient images)	Sensitivity	Specificity	Accuracy
Patient 1	0.88945	0.987777	0.979739
Patient 2	0.886302	0.987206	0.979024
Patient 3	0.914788	0.990442	0.984148
Patient 4	0.924253	0.98494	0.98017
Patient 5	0.888646	0.992594	0.983821
Patient 6	0.726558	0.991662	0.967301
Patient 7	0.775607	0.991761	0.971234
Patient 8	0.896298	0.986927	0.978419
Patient 9	0.831022	0.987508	0.973717
Patient 10	0.842956	0.990614	0.977451

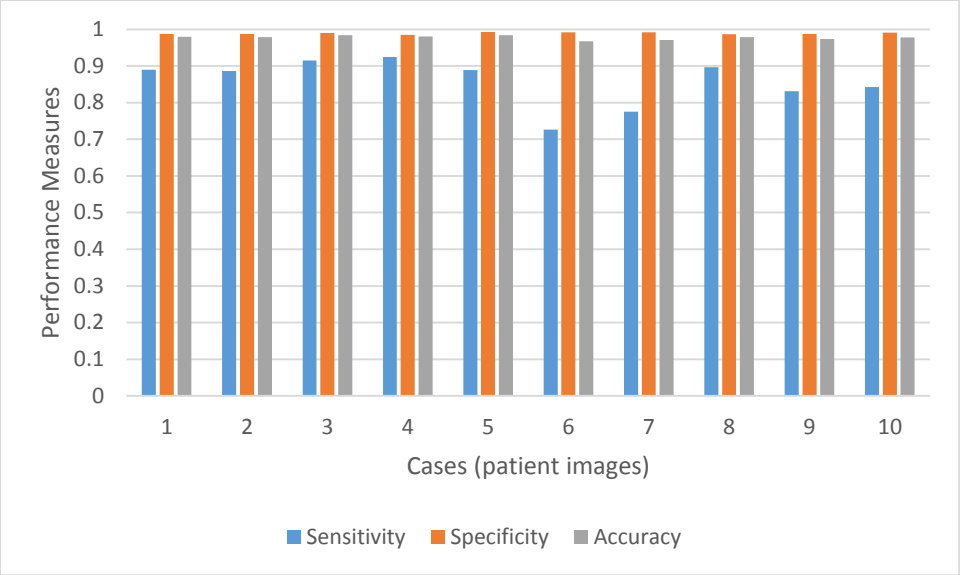

Figure 7.7 Graphical representation of proposed measures for medical image classification.

Figure 7.8 and 7.9 show proposed medical image segmentation research achieves performance measures of 0.8875, 0.9891, 0.010, and 0.1424 for PPV, NPV, FPR, and FNR, respectively. The table 7.7 shows the performance measures of our proposed research. The graphical representation of the proposed PPV and NPV is given in Figure 7.8, and FPR and FNR are given in Figure 7.10.

Table 7.6 Proposed research evaluation measures for PPV, NPV, FPR, and FNR.

Cases (patient images)	PPV	NPV	FPR	FNR
Patient 1	0.866276	0.990135	0.012223	0.11055
Patient 2	0.859408	0.98994	0.012794	0.113698
Patient 3	0.896752	0.992253	0.009558	0.085212
Patient 4	0.839612	0.993483	0.01506	0.075747
Patient 5	0.917087	0.989765	0.007406	0.111354

Patient 6	0.898138	0.972855	0.008338	0.273442
Patient 7	0.908071	0.97681	0.008239	0.224393
Patient 8	0.876596	0.989231	0.013073	0.103702
Patient 9	0.865395	0.983732	0.012492	0.168978
Patient 10	0.897853	0.984722	0.009386	0.157044

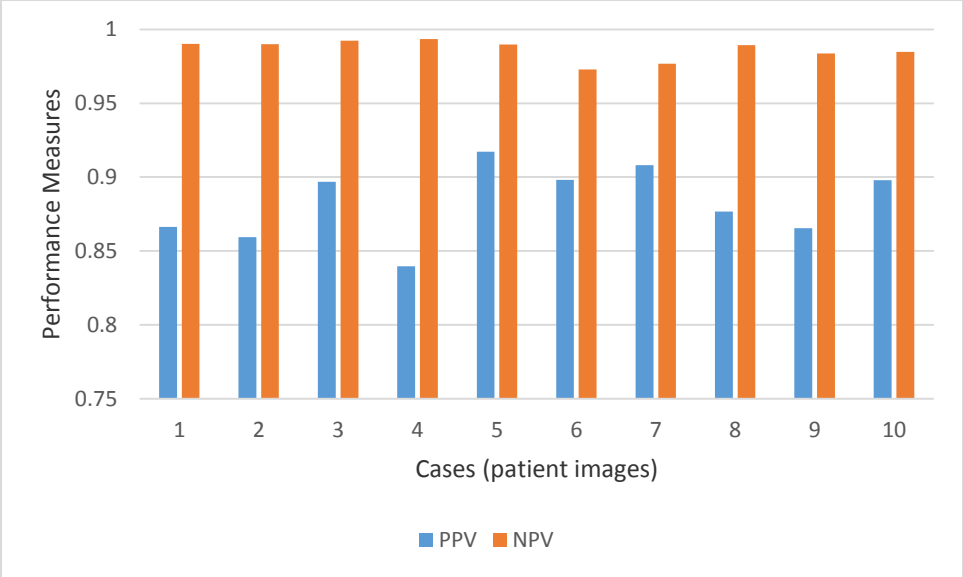

Figure 7.8 Graphical representation of proposed PPV and NPV for medical image classification.

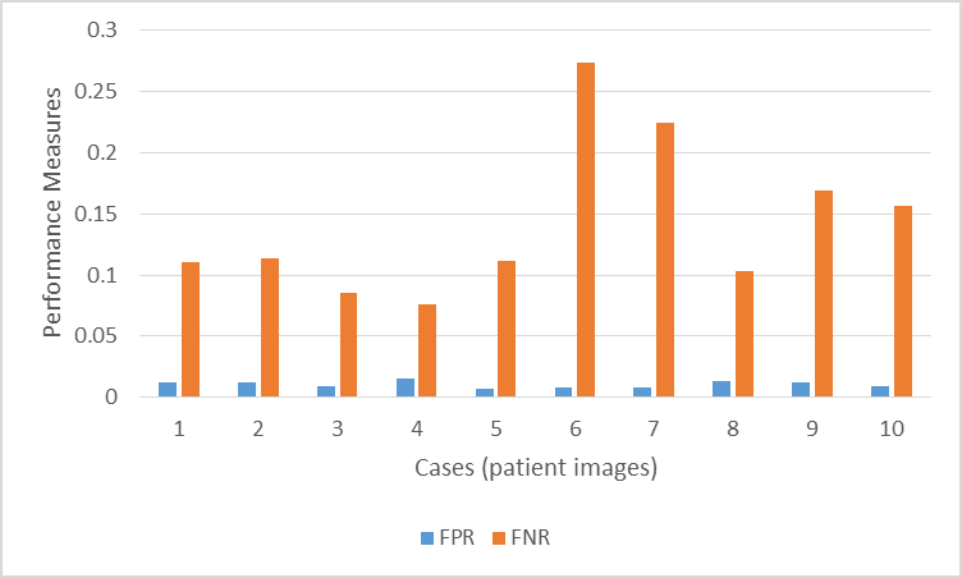

Figure 7.9 Graphical representation of proposed FPR and FNR evaluation measures.

The classification sensitivity from Table 7.8 and its corresponding graph in Figure 7.9. The low values offer a way to raise the classification sensitivity. The sensitivity of our proposed OKK-means technique is 0.8875. When we compare our proposed OKK-means research results to the existing regularized distance level set (RDL), our proposed kernel K-means achieves better results. The sensitivity value of our proposed system is 0.8575; when we compare these results to the existing RDL which achieved a sensitivity of 0.4756, the sensitivity of the existing RDL is low.

Table 7.7 Comparison of proposed and existing sensitivity measures.

Cases (patient images)	**Proposed K-Means**	**Existing RDL**
Patient 1	0.88945	0.843253
Patient 2	0.886302	0.456524
Patient 3	0.914788	0.644543
Patient 4	0.924253	0.469768

Patient 5	0.888646	0.705276
Patient 6	0.726558	0.757151
Patient 7	0.775607	0.727323
Patient 8	0.896298	0.767882
Patient 9	0.831022	0.011589
Patient 10	0.842956	0.475611

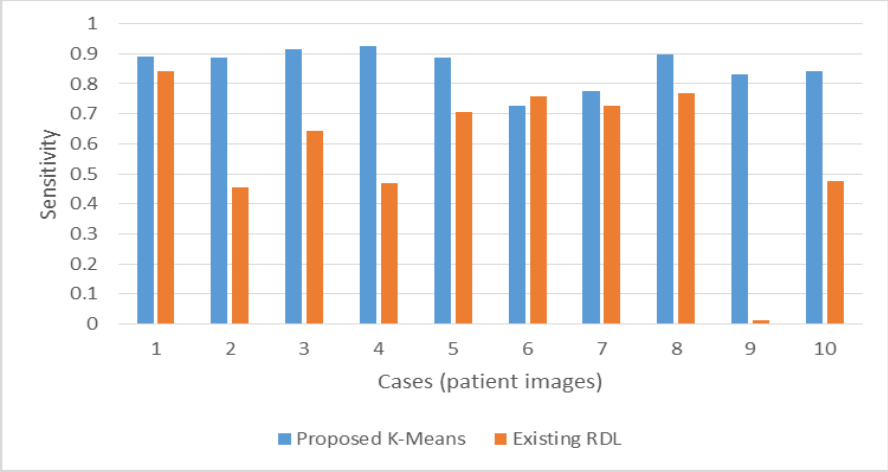

Figure 7.10 Graphical representation of proposed and existing sensitivity measures.

The classification specificity from Table 7.8 and its corresponding graph in Figure 7.10. The low values offer a way to raise the classification specificity. The specificity of our proposed OKK-means technique is 0.9904. We compare our proposed OKK-means research results to the existing RDL which achieved a specificity of 0.9891, the specificity of the existing RDL is low.

Table 7.8 Comparison of proposed and existing specificity measures.

Cases (patient images)	Proposed K-Means	Existing RDL
Patient 1	0.993142	0.987777
Patient 2	0.995127	0.987206
Patient 3	0.992229	0.990442
Patient 4	0.992388	0.98494
Patient 5	0.992834	0.992594
Patient 6	0.990818	0.991662
Patient 7	0.992679	0.991761
Patient 8	0.966975	0.986927
Patient 9	0.996104	0.987508
Patient 10	0.992472	0.990614

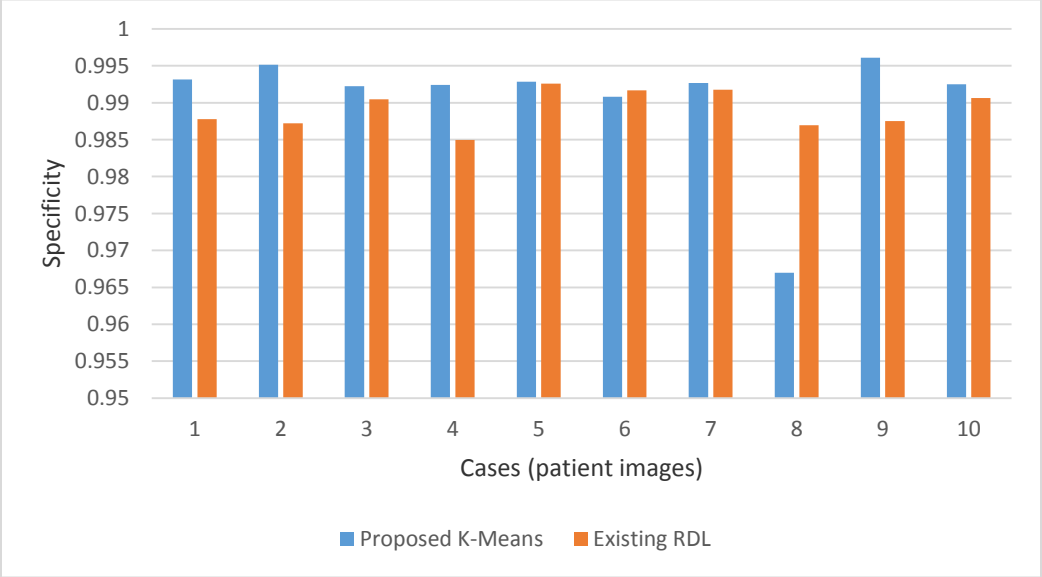

Figure 7.11 Graphical representation of proposed and existing specificity measures.

The classification accuracy from Table 7.9 and its corresponding graph in Figure 7.12. The low values offer a way to raise the classification accuracy. The accuracy of our proposed OKK-means technique is 0.9776. We compare our proposed OKK-means research results to the existing RDL, our proposed kernel K-means achieve better results. The existing RDL which achieved an accuracy of 0.9556, the accuracy of the existing RDL is low.

Table 7.9 Comparison of proposed and existing accuracy measures.

Cases (patient images)	**Proposed K-Means**	**Existing RDL**
Patient 1	0.979739	0.980889
Patient 2	0.979024	0.951455
Patient 3	0.984148	0.963303
Patient 4	0.98017	0.951313
Patient 5	0.983821	0.968564
Patient 6	0.967301	0.969346
Patient 7	0.971234	0.967479
Patient 8	0.978419	0.948284
Patient 9	0.973717	0.909342
Patient 10	0.977451	0.946397

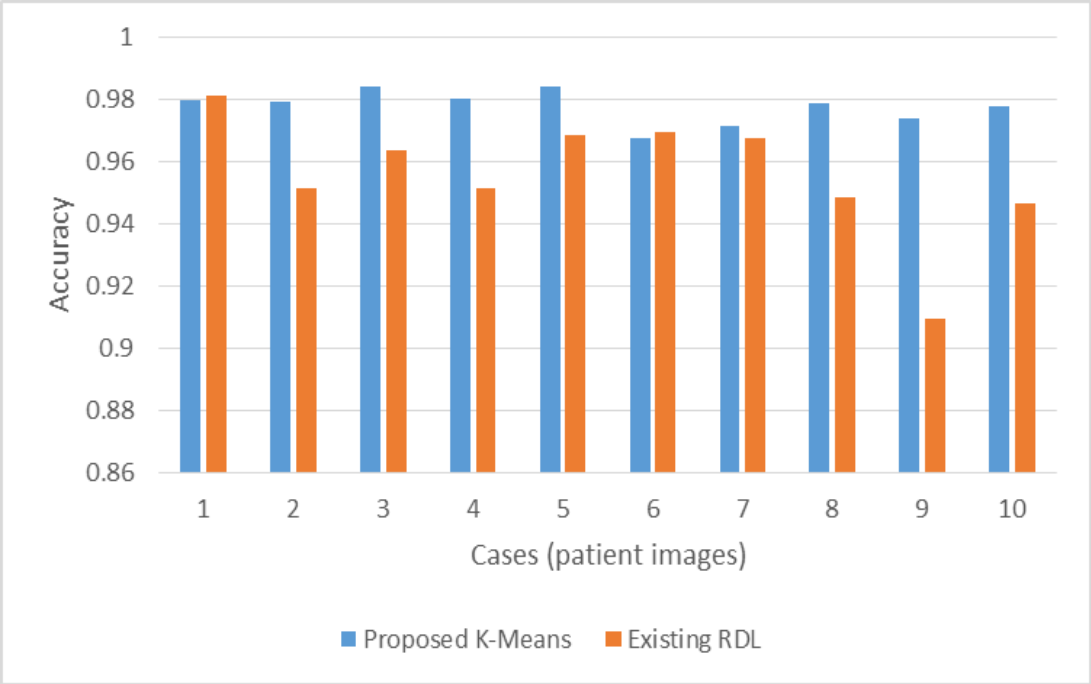

Figure 7.12 Graphical representation of proposed and existing accuracy measures.

The output result of the tumor portion using the segmentation is represented in Figure 7.13. The tumor region is representing in the second figure of both the images. These two examples are the CT and MR images sample of the segmentation output. The details of all the output segmentation results are shown in Appendix A.

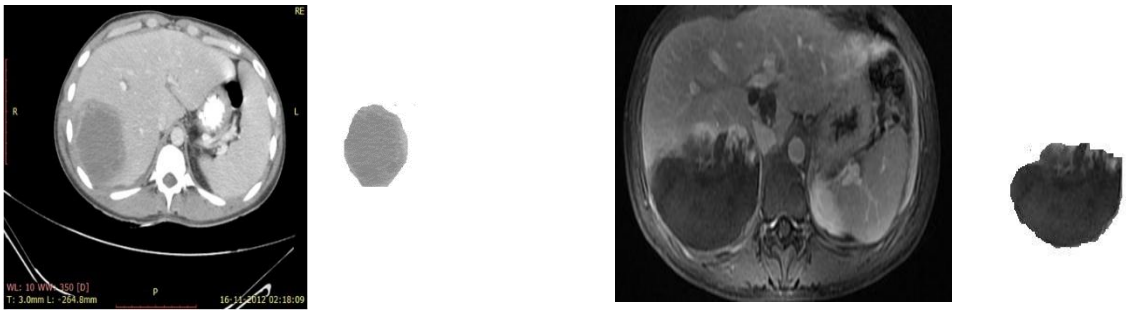

Figure 7.13 Two example images of our database and corresponding segmented tumor portion applying the proposed segmentation method for the CT image and the MR image.

7.6. REGISTRATION

Feature-based registration, the extracted features are MSER and SURF features.

Table 7.10 The minimum, maximum and the average value for all the experiments with the MSER and the SURF features.

Features/ Experiments	MSER			SURF		
	Minimum	Maximum	Average	Minimum	Maximum	Average
1	.679/.8	.789/.881	.7175/.8267	.682/.799	.796/.875	.7184/.8251
2	.672/.767	.755/.852	.6999/.7981	.673/.767	.755/.852	.6988/.7978
3	.601/.735	.705/.85	.6374/.7869	.603/.736	.702/.851	.6394/.7861
4	.573/.76	.653/.815	.5961/.7726	.573/.76	.653/.814	.5961/.7726
5	.701/.781	.789/.866	.7276/.8059	.701/.778	.788/.861	.7282/.8054
6	.593/.728	.705/.86	.6283/.7843	.595/.733	.702/.859	.6287/.7842
7	.567/.757	.634/.804	.5857/.7679	.568/.756	.634/.804	.586/.7679
8	.595/.69	.718/.862	.6324/.7637	.579/.689	.722/.861	.637/.7621
9	.571/.75	.625/.787	.5871/.7633	.571/.75	.625/.788	.5874/.763
10	.572/.698	.631/.81	.5919/.7401	.57/.698	.631/.81	.5918/.7401

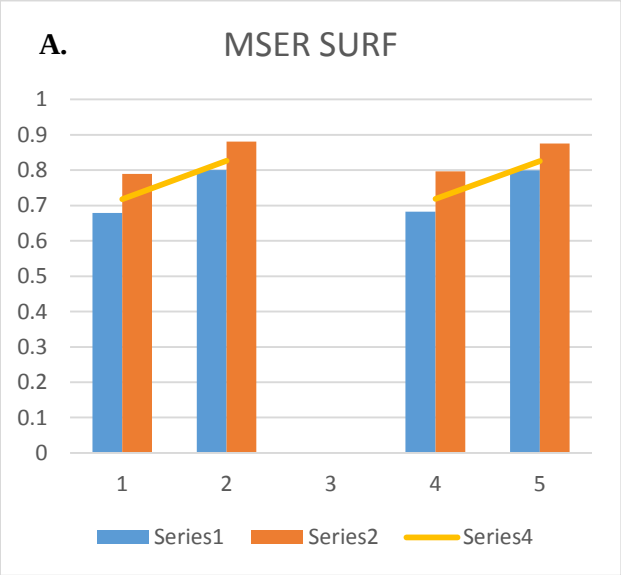

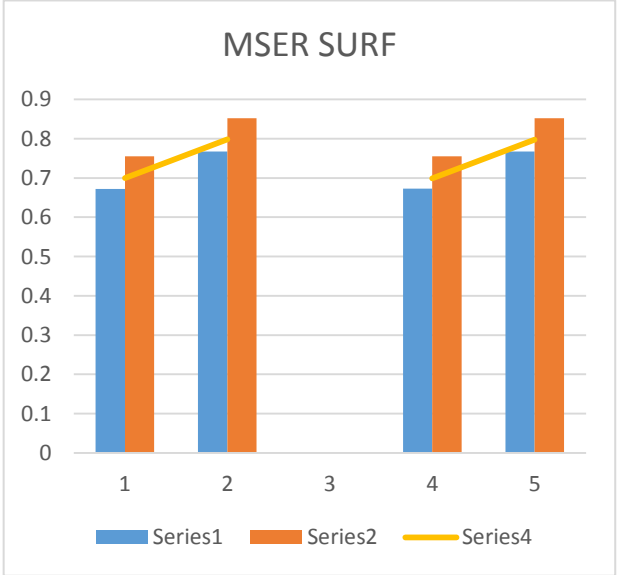

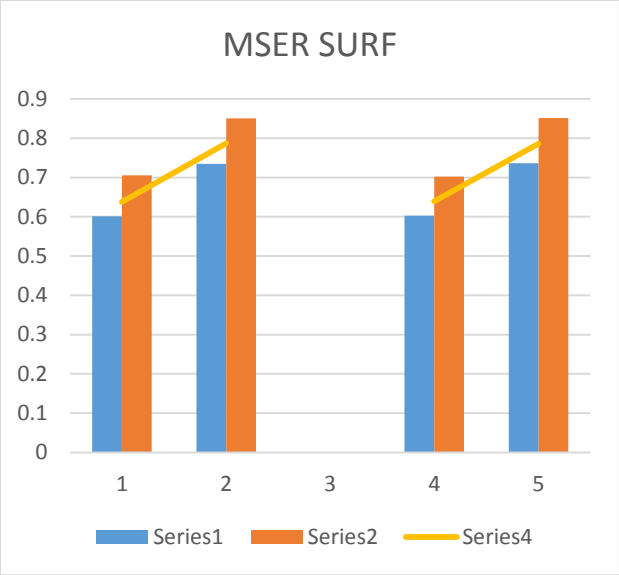
MSER SURF
0.9
0.8
0.7
0.6
0.5
0.4
0.3
0.2
0.1
0
1
2
3
4
5
Series1
Series2
Series4

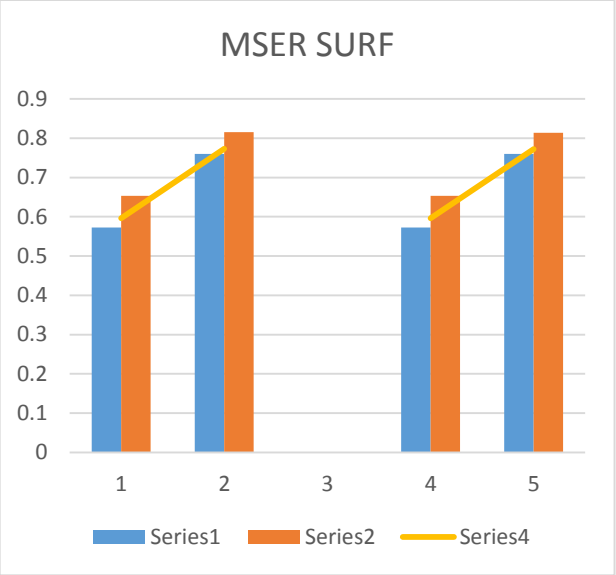
MSER SURF
0.9
0.8
0.7
0.6
0.5
0.4
0.3
0.2
0.1
0
1
2
3
4
5
Series1
Series2
Series4

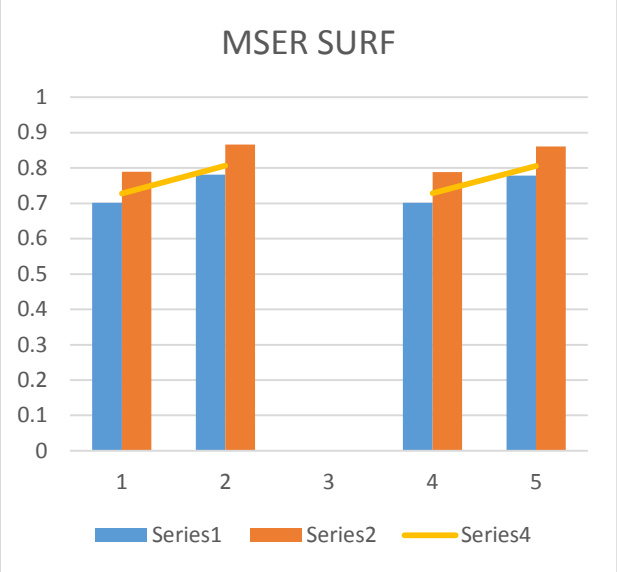
MSER SURF
1
0.9
0.8
0.7
0.6
0.5
0.4
0.3
0.2
0.1
0
1
2
3
4
5
Series1
Series2
Series4

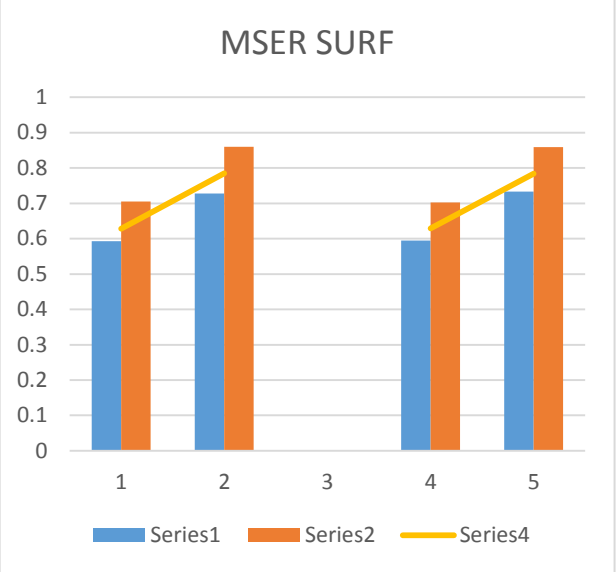
MSER SURF
1
0.9
0.8
0.7
0.6
0.5
0.4
0.3
0.2
0.1
0
1
2
3
4
5
Series1
Series2
Series4

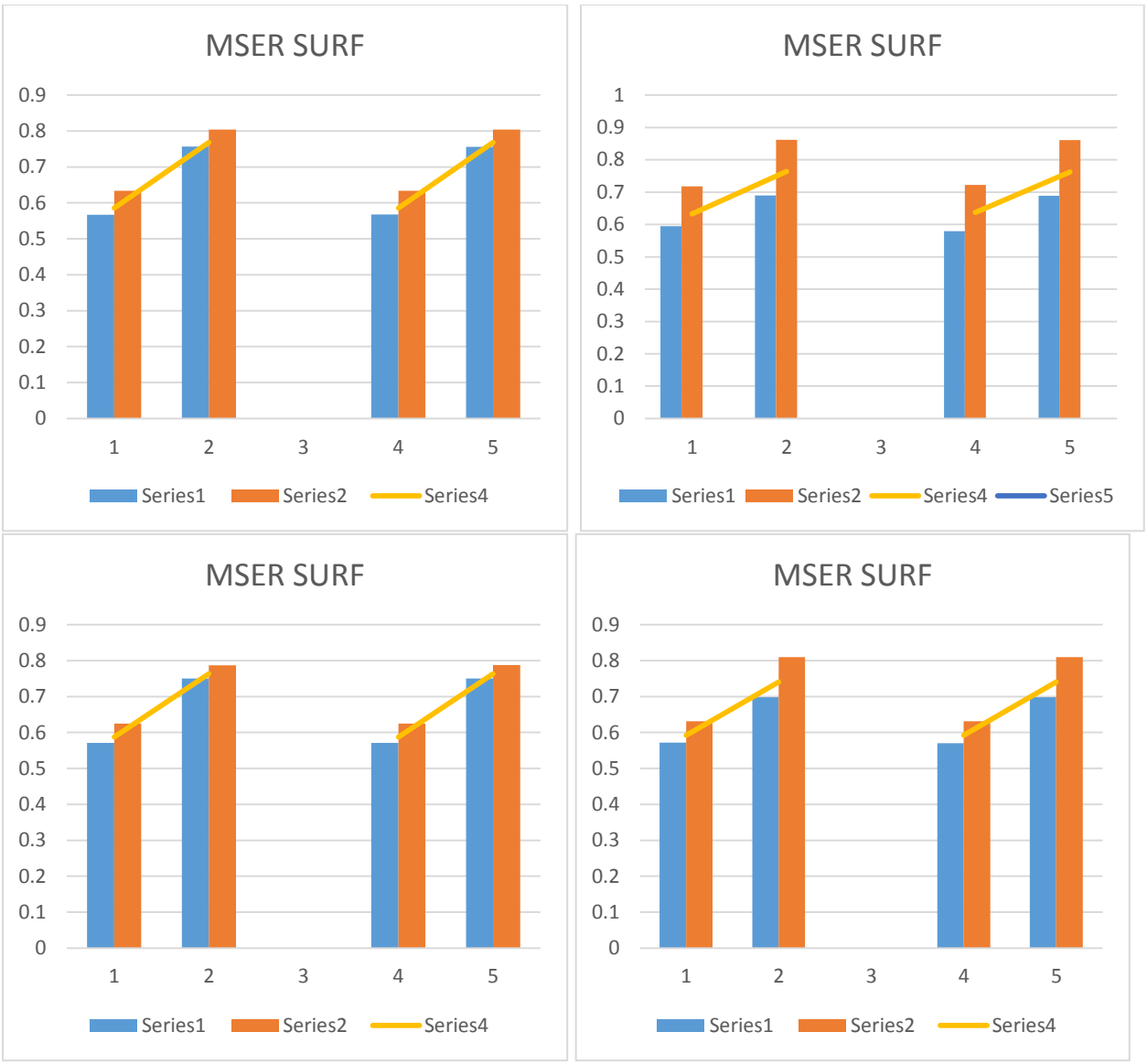

Figure 7.14 The graphical output form of the MSER and the SURF, with the feature output value, varies between 0 and 1. In both of these graphs records, both MSER and SURF parameters representations, that allow comparison in both of them. These records are representing all the phases' experiments for registration. A. The registered image with both the phases, Triple phase CT and arterial phase. B. The registered image with the Triple phase CT and venous phase. C. The registered image with the Triple phase CT and the delayed. D. The registered image with both the Triple phase CT and the delayed 10 min. E. The registered image with both the arterial phase and the venous phase. F. The registered image with the arterial phase and the delayed. G. The registered image with the arterial phase and the delayed 10 min. H. The registered image with the venous phase and the delayed. I. The registered image with the venous phase and the delayed 10 min. J. The registered image with the delayed phase and the delayed 10 min. phase.

Series 1 represents the minimum value, series 2 represents the maximum value, and series 4 represents the average value. Two records 1 and 2 are for the MSER and the two 4 and 5 are for the SURF features. The features results values have a difference because of the different classes of phases shown in Figure 7.14. These are the output of all the ten experiments done for the registration.

Table 7.11 The minimum, maximum, and average values for all the experiments with the detected values and the matches' value.

Observations/ Experiments	**Detected Values**			**Matches Values**		
	Minimum	**Maximum**	**Average**	**Minimum**	**Maximum**	**Average**
1	**736/1054**	**915/1223**	**813.0488/ 1157.878**	**180/616**	**233/713**	**202.6341/ 658.439**
2	**736/1054**	**915/1223**	**813.0488/ 1157.878**	**176/588**	**220/656**	**196/ 625.5366**
3	**736/1054**	**915/1223**	**813.0488/ 1157.878**	**162/518**	**218/638**	**185.878/ 578.9024**
4	**736/1105**	**915/1223**	**813.8889/ 1166.417**	**165/471**	**203/547**	**182.6111/ 510.2222**
5	**755/1113**	**930/1281**	**843.75/ 1202.333**	**185/649**	**235/760**	**208.8542/ 706.4583**
6	**755/1113**	**901/1281**	**841.9149/ 1201.447**	**169/546**	**224/674**	**194.5532/ 605.383**
7	**755/1113**	**963/1281**	**855.3878/ 1198.63**	**158/546**	**201/760**	**175.8571/ 656.8069**
8	**802/1141**	**993/1347**	**891.0638/ 1273.149**	**165/553**	**240/709**	**195.766/ 631.7021**
9	**802/1208**	**1021/1347**	**895.3023/ 1284.605**	**166/489**	**199/566**	**180.3721/ 531.2093**
10	**770/1067**	**967/1277**	**863.6667/**	**164/459**	**214/597**	**186.6429/**

			1187.548			**528.5476**

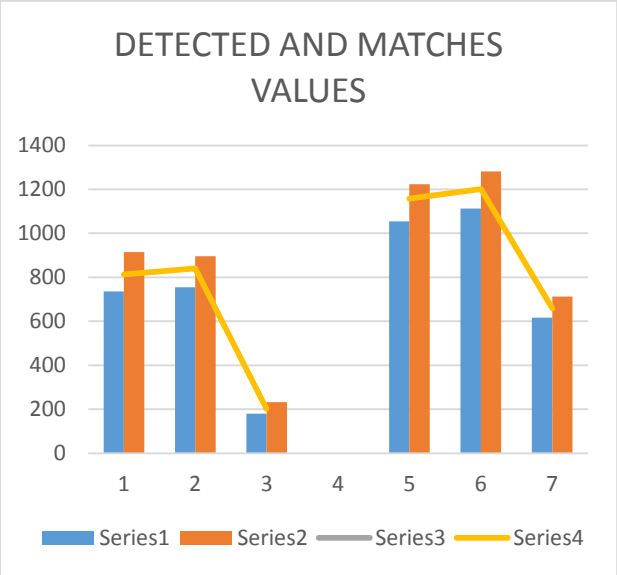

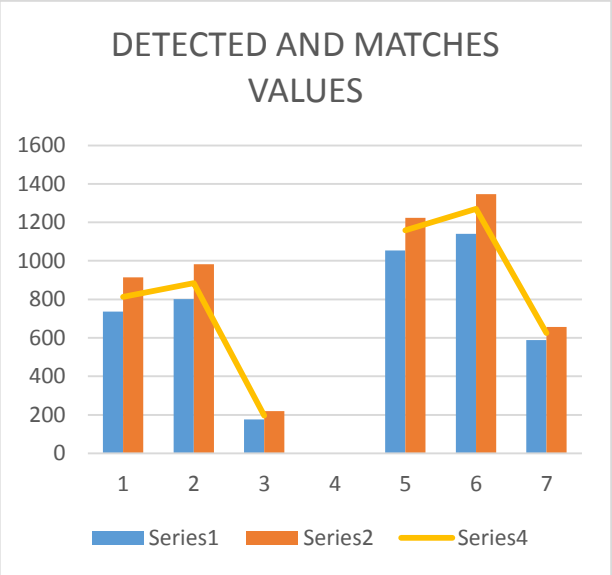

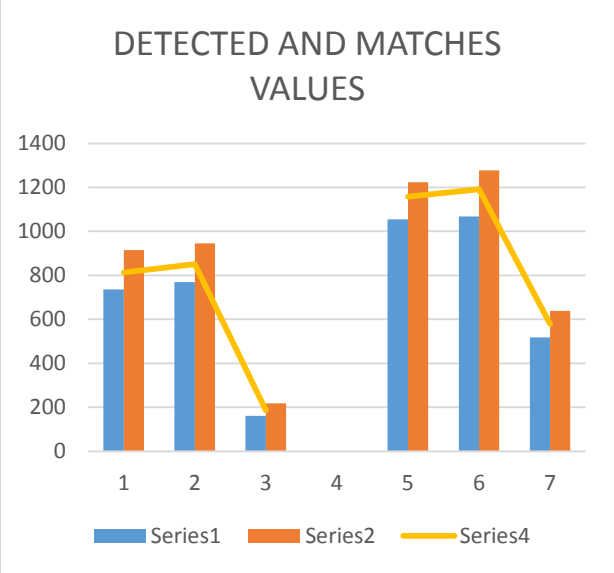

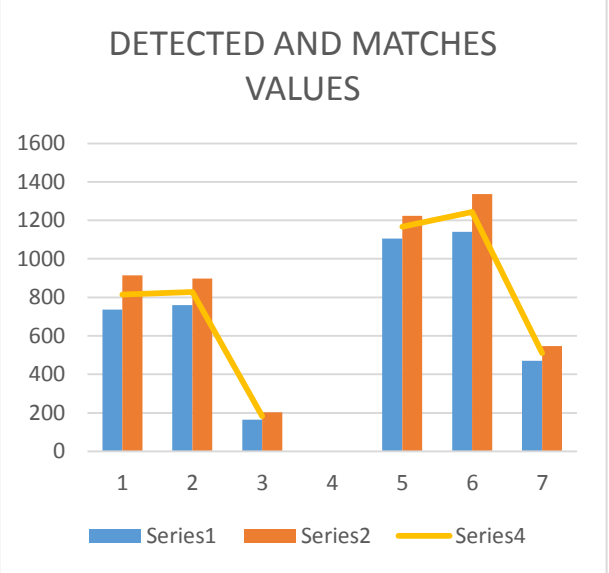

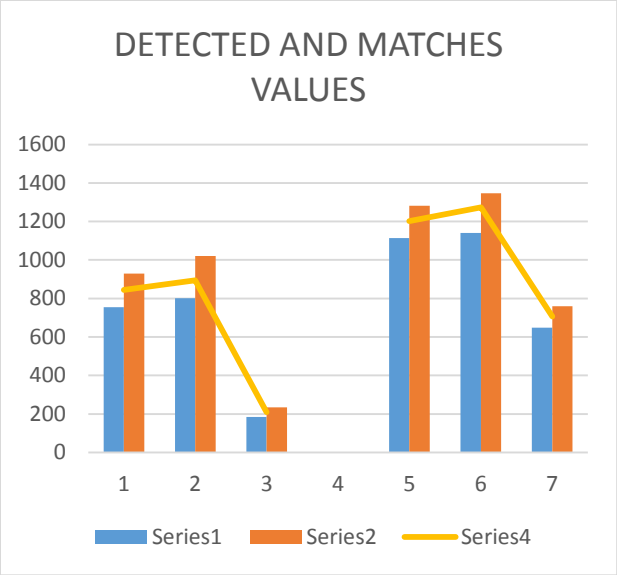
DETECTED AND MATCHES VALUES
1600
1400
1200
1000
800
600
400
200
0
1
2
3
4
5
6
7
Series1
Series2
Series4

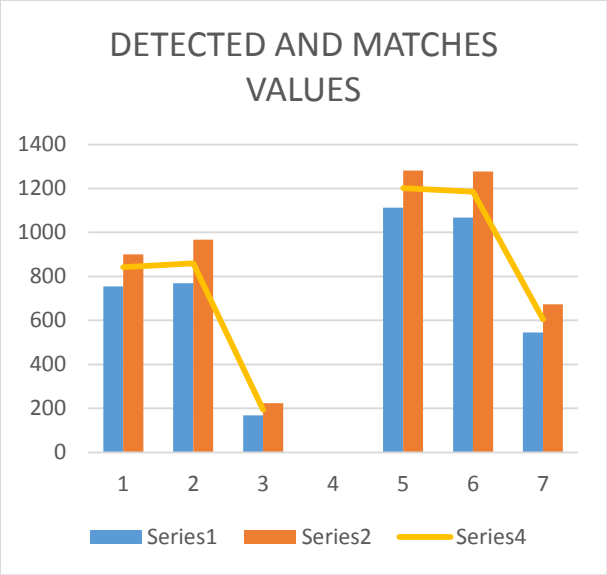
DETECTED AND MATCHES VALUES
1400
1200
1000
800
600
400
200
0
1
2
3
4
5
6
7
Series1
Series2
Series4

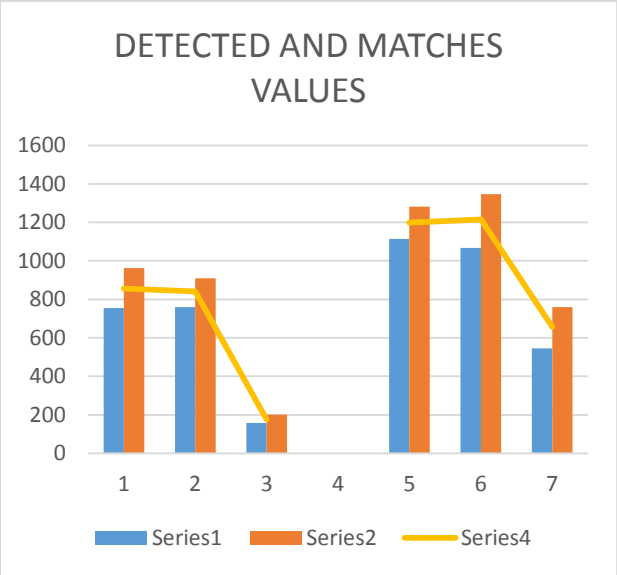
DETECTED AND MATCHES VALUES
1600
1400
1200
1000
800
600
400
200
0
1
2
3
4
5
6
7
Series1
Series2
Series4

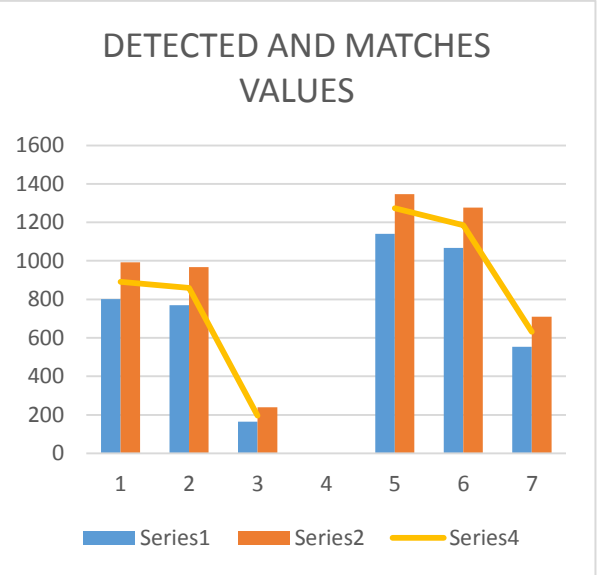
DETECTED AND MATCHES VALUES
1600
1400
1200
1000
800
600
400
200
0
1
2
3
4
5
6
7
Series1
Series2
Series4

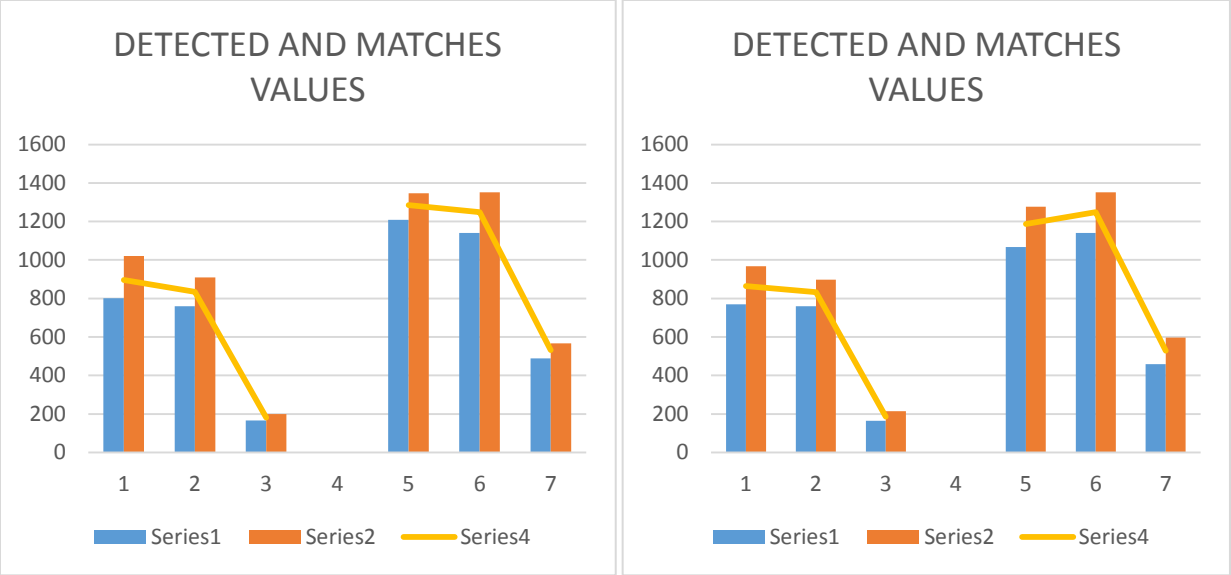

Figure 7.15 The second part is the number of the detected and the matches' values among the input of the registered images, with the MSER and the SURF calculated features. A. The registered image with both the phases, Triple phase CT and arterial phase. B. The registered image with the Triple phase CT and venous phase. C. The registered image with the Triple phase CT and the delayed. D. The registered image with both the Triple phase CT and the delayed 10 min. E. The registered image with both the arterial phase and the venous phase. F. The registered image with the arterial phase and the delayed. G. The registered image with the arterial phase and the delayed 10 min. H. The registered image with the venous phase and the delayed. I. The registered image with the venous phase and the delayed 10 min. J. The registered image with the delayed phase and the delayed 10 min. phase.

Series 1 represents the minimum value, series 2 represents the maximum value, and series 4 represents the average value. Records 1, 2, and 3 are for the detected values and the records 5, 6, and 7 are for the matches' values. The detected and the matches' values have a difference because of the different classes of phases because of the different classes of phases shown in Figure 7.15. These are the output of the detected and the matches' values with all the ten experiments done for the registration.

The output result of the registered image is shown in Figure 7.16. This is a result of the registered image for a fixed image and a moving image. This example is of the same input images, two different output registered image from the same series. The details of all the output registered images are shown in Appendix B.

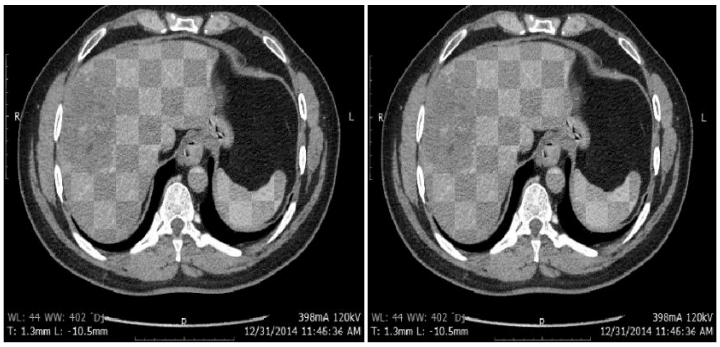

(a) **(b)**

Figure 7.16 The two example images showing registration results with the arterial and the venous phase as the fixed image and the moving image.

Image registration in this work has been done with multi-phase CT images. These images are of the same patients with different phases and delayed phases. CT images with different orientations and phases make a particular contribution to the patient's individual organ and function. Multi-phase CT images play a key role in patient assessment and treatment planning in liver. Therefore, the proposed registration solutions enable the combined use of information from multimodal imaging and provide an excellent basis for patient assessment and primary planning for liver tumor.

7.7. Experimental Environment

The experimentations are done using the softwares MATLAB (2018a-MathWorks) and Image J Processing Toolbox. The images are carried out as the input image. The input image as the raw image form takes the less time for the execution in comparison of the enhanced image input form. The image with different classes of intensity present takes more time for the execution.

7.8. Concluding Remarks

The liver cancer detection and classification is done and its performance is improved by the ensemble model. The segmentation is effectively done using OKK-means clustering algorithm. For the registration, there is a finding of the correspondence of feature spheres in two images. The quality matches values allowing the radiologist to correlate the different phases in the tumor large size liver using both the calculated features in all the other experiments. Multi-phase image registration results aid in diagnostic interpretation.

Chapter 8

CONCLUSIONS

This chapter summarizes the conclusions drawn from the experiments that have been performed in the process of the diagnosis of the liver cancer diseases. The experimentations were performed to diagnose the liver cancer diseases, HCC and MET, using CT and MR images. The conclusions are drawn from this research work, feature extraction and classification, Segmentation and Registration are described here. The last section described the future scope of this research work.

8.1. FEATURE EXTRACTION AND CLASSIFICATION

- The image enhancement was done on the images as the pre-processing step, which improve their visualization to get a clear look for the tumor. The image enhancement was done using CLAHE and CVHE algorithms. Both of these have a HE, which resulted in the regions matches their surrounding areas. The enhancement was done to improve the contrast, remove the noise and get a different clear look with the tumor present in the liver portion of the image.
- The IROI and SROI are extracted from the enhanced images, and the features are evaluated to design a CAD, with the IROI features and the ratio features, the ratio of the IROI and the SROI features. The IROI features detect cancer among the normal liver and the tumor liver, and further, it classifies the different classes of liver cancer diseases. The ratio features of the IROI and the SROI were used to classify the tumor class with 84% accuracy. The sub-experiments using IROI and the feature selection experiments have robustness performance with their classifier rate.
- Feature selection, the selection of the features done by two patterns, automatic and manual type of feature selection. The manual feature selection is made to select the group of features in the order of the best classifier rate. Automatic selection of features using GA algorithm, which generates automatically the selected features with the order of preference of the features. These feature selections allowed to check the variation of the classifier rate in a particular feature class, group of features and designing the best features classes for a better classifier rate. The manual selection of features, resulted in a

better classifier rate for the more number of features that are tested. An automatic selection of features, ranked the different classes of features optimally, resulted in the best classifier rate feature to allow various types of testing to check with a classifier rate.

- The classification was done using various classifiers, Adaboost, GLM, NN, SVM, R-part decision tree and RF. The classification was used to detect the tumor, using the normal and tumor liver region. Further, to classify the tumor, as the HCC and the MET diseases are classified using classification. There are various classifiers used to compare the experiments' performance and get the best classifier result. That allows yielding the best result among all. An ensemble classifier model for the combination of all the classifiers in the experiments, that's results allowed to improve the classier rate in comparison of the best classifier rate.
- Gabor filters five scales and eight orientations, cover the spatial frequency domain, to detect and classify liver cancer diseases in various experimentations. This Gabor filter work, done on a large number of CT and MR images. K-fold CV has been done to check the robustness of the classifier results in a large image database. The key results from the overall experimentation, the CT images have the best predictor rate of 97.31% accuracy, 98% sensitivity and 100% specificity. The other results to predict and classify the tumor results vary within the range of 30% lower accuracy. On the best classification rate in each experiment, 5-fold CV was performed.

In this work, the primary class liver cancer as HCC and the secondary class liver cancer as MET classified using various experimentations, to detect the tumor, to check the tumor variation with the patient records, and to comment upon their size, with the analyzes of different phases tumors, which allow extracting the useful information with the tumor present in the liver. Different Classifiers performance ensemble to improve the classification accuracy among all the classifiers. That ensemble performance has been checked using various performance measures. These works allow to check the robustness of the classifiers model and analyze the tumor variation with a particular image. The optimized Gabor filter scaling and orientation on both the CT and MR images for the detection and the classification of the liver cancer. The frequency domain, multi-resolution decomposition detect and classify using the combination of CT and

MR, CT and MR individually utilizing a group of classifiers and check their performance measures, with the CV to check their robustness.

8.2. SEGMENTATION

An Efficient segmentation and classification technique, three phases are pre-processing, segmentation and classification. The segmentation is effectively done using the OKK-means clustering algorithm on the Liver images of CT and MRI. This proposed work obtained 97.75% accuracy when compared to the existing algorithm RDL obtained 95.5% only. For the segmentation, an efficient segmentation has been done using OKK-means clustering algorithm that segmented results allow for the classification of the tumor using feature selection with better results.

It allows to create a liver abnormality detection, its performance analyzed with various persons normal and abnormal images. This technique resulted better in terms of accuracy, sensitivity and specificity in comparison to the existing RDL algorithm. The classification performance with the aid of the OKK-means clustering technique.

8.3. REGISTRATION

For the multi-phase CT images registration, the image registration is done to get the MI between two different phases of the same patient and get valuable information about a particular phase. This registration also includes some particular class delayed phase. The registered images works allow to get the best result with the maximization of the detected and the matched values of the two selected images as the part of the multi-phase. The registered output images have the different forms, checkerboard and different color combinations as the combination of two phase's image. The output registered images, have a correspondence finding spheres in two images. The calculated output parameter allowing the radiologist to correlate the different phases in the tumor large size liver.

The classifier rate of the different liver cancers yields satisfactory results to assist the experienced radiologists. The overall satisfactory results help the radiologist with the group of different combinations of a large amount of the data. The optimized Gabor filter scaling and the orientation allow the radiologist to comment on the tumor and its level class before diagnosis.

CT, MR images and their combination before treatment allows deciding the liver diagnosis. The segmentation allows better response with the existing algorithm, with the segmentation and its classification results, its early detection of liver tumor helps the patients to cure rapidly. The multi-phase CT image registration allows getting the MI from the two images to see them better visualization combination of the two phases. Registration work allows the radiologist to assist the delayed phases and other classes of phase and correlate the images with useful information.

8.4. FUTURE SCOPE

The characterization of the multi class's performance improve by using more feature selections techniques for the ensemble classifier work. The classifier rate improves by using the feature selection technique, which yields a better individual classifier rate. The optimization settings of the scaling and orientation parameters using Gabor filters CT and MR images common function to check some similarities and dissimilarities with the present work. By the variation in the dimensions of the original images, the extracted parameters have the variation with tumor size, which help in determine the tumor size and to comment on the level of the tumor present in the images.

For the segmentation, we can classify the severity of the tumor concerning the lesion size. Early detection of the tumor in the liver will help to cure the patient at an early stage.

For the image registration, the image registration is possible with more desired phases, and this type of registration work may also be possible to work with MRI or ultrasonic type different images.

REFERENCES

[1] American cancer society n.d.

[2] Jian Hua Liu, Jain Wei Wang, "Research on Contour correction in Medical CT Image segmentation" Journal of Computers, Vol.7(3), 2012.

[3] Virmani J, Kumar V, Kalra N, Khandelwal N. PCA-SVM based CAD system for focal liver lesions using B-mode ultrasound images. Def Sci J ;63:478–86, 2013.

[4] Hui W, Yong Y, Hongjun W, Guanzhong G, A modified optical flow method for registration of 4D CT data of Hepatocellular carcinoma Patients IEEE. International conference on virtual environments Human-computer interfaces and measurement systems, pp.21-25, 2012.

[5] Gordillo N, Montseny E, Sobrevilla P. State of the art survey on MRI brain tumor segmentation. Magn Reson Imaging; 31:1426–38, 2013.

[6] http://www.wcrf.org/int/cancer-facts-figures/data-specific-cancers/liver-cancer-statistics n.d.

[7] http://globocan.iarc.fr/old/FactSheets/cancers/liver-new.asp. n.d.

[8] Sahani D.V., Kalva S.P., "Imaging the liver", the oncologist, vol. 9, pp. 385-397, 2004.

[9] Seletchi E. D., Duliu O. G., 'Image processing and data analysis in Computed tomography' Presented paper at 7th International Balkan workshop on applied physics, pp. 667-675, 2006.

[10] T. Tajima, X. Zhang, Kitagawa T., Kanematsub M., Zhoua X., Hara T., Fujita H., Yokoyamab R., Kondob H., Hoshib H., Nawanoc S., Shinozaki K., "CAD of HCC on multiphase CT images" Medical imaging, vol. 6514, editors 65142(1-10), 2007.

[11] Hsu W.T., Yeh J.R., Chang Y.C., Lo M.T., Lin Y.H. 'A computer-aided for image processing of computed tomography in Hepatocellular carcinoma', International Conference on Bioinformatics and biomedicine workshops, IEEE, 2011.

[12] Kim K-B, Kim C.W., Kim G.H., "Area extraction of the liver and Hepatocellular carcinoma in CT scans" Journal of Digital imaging, vol.21(1), pp. 89-103, 2008.

[13] Das A., Das P., Panda S.S., Sabut S., "Detection of Liver cancer using modified Fuzzy Clustering and Decision Tree Classifier in CT images", Pattern Recognition and Image Analysis, Vol. 29(2), pp. 201–211, 2019.

[14] Freiman M. Edrei Y., Gross E., Joskowicz L., Abramovitch R., 'Liver metastases early detection using fMRI based statistical model', 5th IEEE international symposium on biomedical imaging, pp. 584-587, 2008.

[15] K. Deep, M. Thakur: "A Real Coded Multi Parent Genetic Algorithm for Function Optimization", Journal of Hybrid Computing Research, Vol. 1(2), pp. 67 – 83, 2008.

[16] Chen EL, Chung PC, Chen CL, Tsai HM, Chang CI. An automatic diagnostic system for CT liver image classification. IEEE Trans Biomed Eng;45:pp.783–94, 1998.

[17] Gletsos M, Mougiakakou SG, Matsopoulos GK, Nikita KS, Nikita AS, Kelekis D. Classification of hepatic lesions from CT images using texture features and neural networks. Conf. Proc. 23rd Annu. Int. Conf. IEEE Eng. Med. Biol. Soc., vol. 3, pp. 2748–51, 2001.

[18] Valavanis IK, Mougiakakou SG, Nikita A, Nikita KS. Evaluation of texture features in hepatic tissue characterization from non-enhanced CT images. Annu. Int. Conf. IEEE Eng. Med. Biol. - Proc., Lyon, France:, pp. 3741–4, 2007.

[19] Rajendran P., Madheswaran M. 'Hybrid medical image classification using association rule mining with decision tree algorithm' Journal of computing, Vol: 2(1) 127-136, 2010.

[20] Padma A., Sukanesh R. 'Automatic classification and segmentation of brain tumor in CT images using optimal dominant gray level run length texture features' International journal of advanced computer science and applications, Vol:2(10), 2011.
[21] Gunasundari G., Ananthi M.S. 'Comparison and evaluation of methods for liver tumor classification from CT datasets' International journal of computer applications, Vol: 39(18), 2012.
[22] Umamaheshwari J, Radhamani G. Quadratic Program Optimization using Support Vector Machine for CT Brain Image Classification. Int J Comput Sci Issues;9:305–10, 2012.
[23] Leena N.V.: 'Automatic brain tumor medical image classification using hyperbolic Hopfield neural network' Journal of chemical and Pharmaceutical Research, Vol: 7(2):190-199, 2015.
[24] Veeramuthu A, Meenakshi S. An Efficient Approach for Medical Image Classification using Association Rules. Int J Comput Appl 2014;90:1–6, 2014.
[25] Veeramuthu A, Meenakshi S, Tejaswi YD. An efficient and fast brain CT image classification using hybrid technique. ARPN J Eng Appl Sci;10:2004–10, 2015.
[26] Alahmer H., Ahmed A. 'Computer-Aided classification of Liver lesions from CT Images Based on Multiple ROI' International conference on medical imaging understanding and analysis, pp. 80-86, 2016.
[27] Perumal S, Velmurugan T. Lung cancer detection and classification on CT scan images using enhanced artificial bee colony optimization. Int J Eng Technol;7:74, 2018.
[28] Özyurt F, Tuncer T, Avci E, Koç M, Serhatlioğlu İ. A Novel Liver Image Classification Method Using Perceptual Hash-Based Convolutional Neural Network. Arab J Sci Eng;44:3173–82, 2019.
[29] Bhatnagar D, Tiwari AK, Vijayarajan V, Krishnamoorthy A. Classification of normal and abnormal images of lung cancer. IOP Conf. Ser. Mater. Sci. Eng., vol. 263, 2017.
[30] Punia R, Singh S. Automatic Detection of Liver in CT images using Optimal Feature based Neural Network. Int J Comput Appl;76:53–60, 2013.
[31] Khachane M.Y.: 'Fuzzy based CT scan brain image classification' International journal of latest research in science and technology, vol: 4 (6) 71-74, 2015.
[32] Bhuvaneswari C, Aruna P, Loganathan D. Classification of Lung Diseases by Image Processing Techniques Using Computed Tomography Images. Int J Adv Comput Res;4:87–93, 2014.
[33] Rajathi G.I., Jiji G.W., 'Chronic liver disease classification using hybrid whale optimization with simulated annealing and ensemble classifier', 11, 33;Symmetry 2019.
[34] Ye J., Sun Y., Wang S., Gu L., Qian L., Xu J. 'Multi-phase CT image based hepatic lesion diagnosis by SVM', 2nd International conference on Biomedical engineering and informatics IEEE, 2009.
[35] Zhang, X., Furukawa, T., Zhou, X., Hara, T., Kanematsu, M., Fujita, H. 'Detection of metastatic liver tumor in multi-phase CT images by using a spherical gray-level differentiation searching filter' In Medical Imaging: Computer-Aided Diagnosis (Vol. 7963, p. 79632K), 2011.
[36] Stoitsis J, Valavanis I, Mougiakakou SG, Golemati S, Nikita A, Nikita KS. Computer aided diagnosis based on medical image processing and artificial intelligence methods. Nucl Instruments Methods Phys Res Sect A Accel Spectrometers, Detect Assoc Equip;569:591–5, 2006.
[37] Zhang X, Fujita H, Qin T, Kanematsu M. CAD on liver using CT and MRI. Med. Imaging Informatics, Beijing, China: 2007.

[38] Kayaalti Ö, Aksebzeci BH, Karahan IÖ, Deniz K, Öztürk M, Yilmaz B, et al. Staging of the liver fibrosis from CT images using texture features. 7th Int. Symp. Heal. Informatics Bioinformatics, HIBIT 2012, Nevsehir, Turkey: 2012, pp. 47–52, 2012.
[39] Ali A.H., Hadi E.M., Mazhir S.N. 'Diagnosis of Liver tumor from CT images using Unsupervised classification with geometrical and statistical features' International journal of advanced research in computer science and software engineering, Vol:5(3), 2015.
[40] Anthimopoulos M., Christodoulidis S., Ebner L., Christe A., Mougiakakou, 'Lung pattern classification for interstitial lung diseases using a deep convolutional neural network' IEEE Transactions on medical imaging 35(5), 2016.
[41] Bogomasov K., Himmelspach L., Klassen G., Tatusch M., Conrad S., 'Feature based approach for severity scoring of lung tuberculosis from CT images' vol-2125, Image CLEF 2018.
[42] Yu NC, Chaudhari V, Raman SS, Lassman C, Tong MT, Busuttil RW, Lu DSK, "CT and MRI improve detection of HCC, Compared with Ultrasound Alone, in Patients with Cirrhosis", Clinical Gastroenterology and Hepatology, vol. 9 , pp.161-167, 2011.
[43] Sadeghi M, Memarzadehzavareh F, Abedzadehzavareh M, "Applying Gabor wavelet in Image processing for defect detection on steel plates" International journal of advanced biotechnology and research, ISSN 0976-2612, Vol:7(4), pp. 253-258, 2016.
[44] Sahoolizadeh H., Sarikhanimoghadam D., Dehghani H., "Face Detection using Gabor Wavelets and Neural Networks," World Academy of Science, Engineering and Technology 45, 2008.
[45] Vyas V.S., Rege P., "Graphics, Vision and Image Processing (GVIP) journal, Vol: 6(1), 2006.
[46] Acra S., Campadelli P., Lanzarotti R., "A face recognition system based on automatically determined facial fiducial points" Pattern Recognition 39(3):432-443, 2006
[47] Thiang, Lim R., Guntoro A. T., "Car Recognition Using Gabor Filter Feature Extraction" Asia-Pacific Conference on Circuits and Systems, IEEE explore 2003.
[48] Monero P., Bernardino A., Victor J.S., "Gabor parameter selection for local feature detection" 2nd Iberian conference on pattern recognition and image analysis, 2005.
[49] Sabri M., Feiguth P., "A new Gabor filter based kernel for texture classification with SVM" International Conference on Image Analysis and Recognition, 2004.
[50] Fasel I.R., Barlett M.S., Movellan J.R., "A comparison of Gabor filters methods for automatic detection of facial landmarks" Proceedings of the 5th IEEE international conference on automatic face and Gesture Recognition, IEEE 2002.
[51] Clausi D.A., Deng H., "Fusion of Gabor filter and co-occurrence probability features for texture recognition" 16th International Conference on Vision Interface, 2003.
[52] Chen L., Lu G., Zhang D., "Effects of different Gabor filter parameters on Image Retrieval by Texture" 10th International Multimedia Modelling Conference Proceedings, 2004.
[53] Ahmadian A., Mostafa A., Abolhassani M.D., Riahi Alam N., "A method for texture classification of ultrasonic liver images based on Gabor filters" ICSP'04 Proceedings, IEEE 2004.
[54] Monti S., Palma G., Ragucci M., Mannelli L., Mancini M., Prinster A., "Optimization of Tagged MRI for Quantification of Liver Stiffness Using Computer Simulated Data, 2014.
[55] Rajagopal R., Subbiah P., "Computer Aided Detection of Liver Tumor using SVM Classifier, International journal of advanced research in electrical, Electronics & Instrumentation, Vol: 3(6), 2014.

[56] Echegaray S., Gevaert O., Shah R., Kamaya A., Louie J., Kothary N., Napel S., "Core samples for radiomics features that are insensitive to tumor segmentation: method and pilot study using CT images of hepatocellular carcinoma, Journal of medical imaging 2(4), SPIE 2015.
[57] Li Z., Mao Y., Huang W., Li H., Zhu J., Li W., Li B., Texture-based classification of different single liver lesion based on SPAIR T2W MRI images, BMC medical imaging, 2017.
[58] Patil R. V., Sannakki S.S., Rajpurohit V.S., "A Survey on Classification of Liver Diseases using Image Processing and Data Mining Techniques, International Journal of computer sciences and Engineering, Vol:5(3), 2017.
[59] Pasternack R.M., Qian Z., Zheng J.Y., Metaxas D.N., White E., Boustany N.N., Measurement of subcellular texture by optical Gabor-like filtering with a digital micromirror device, PMC 2010.
[60] Parvathy S., Thamil J. S., "Classification and analysis of Ultrasound Liver images" International Journal of Engineering research and technology" Conference proceedings 2014.
[61] Mohammed S.S., Abdel-galil T.K., salama M.M.A., El-saadany E.F., Kamel M., " Prostate cancer diagnosis based on Gabor filter texture segmentation of ultrasound image, Canadian Conference on Electrical and Computer Engineering. Toward a Caring and Humane Technology, IEEE 2003.
[62] Rana S., Jain S., Virmani J., "Classification of kidney lesions using Gabor Wavelet texture features" International Conference on Computing for Sustainable Global Development in Proceedings IEEE 2016.
[63] Pasternack R.M., Rabin B., Zheng J.Y., Boustany N.N., "Quantifying subcellular dynamics in apoptotic cells with two-dimensional Gabor filters, Vol. 1(2) Biomedical optics express 720, 2010.
[64] Rajagopal R., Subbaiah P., "A survey on liver tumor detection and segmentation methods, ARPN Journal of engineering and applied sciences, Vol: 10(6) 2015.
[65] Bovik A.C., Clark M., Geisler W.S., "Multichannel texture analysis using localized spatial filters, IEEE Trans. Pattern Analysis Mach. Intell. 12, 55-73, 1990.
[66] Jain A.K., Farrokhnia F., "Unsupervised texture segmentation using Gabor filters, Pattern recognition 24, 1167-1186, 1991.
[67] Teuner A., Pichler O., Hosticka B.J., "Unsupervised texture segmentation of images using tuned matched Gabor filters, IEEE Trans. Image processing 4, 863-870, 1995.
[68] Bereciartua A, Picon A, Galdran A, Iriondo P. 3D active surfaces for liver segmentation in multi-sequence MRI images. Comput Methods Programs Biomed; 132:149–60, 2016.
[69] Chartrand G, Cresson T, Chav R, Gotra A, Tang A, De Guise JA. Liver segmentation on CT and MR using Laplacian mesh optimization. IEEE Trans Biomed Eng; 64:2110–21, 2017.
[70] López-Mir F, Naranjo V, Angulo J, Alcaniz M, Luna L. Liver segmentation in MRI: a fully automatic method based on stochastic partitions. Comput Methods Programs Biomed; 114:11–28, 2014.
[71] Swierczynski P, Papież BW, Schnabel JA, Macdonald C. A levelset approach to joint image segmentation and registration with application to CT lung imaging. Comput Med Imaging Graph; 65:58–68, 2018.
[72] Huang Q, Ding H, Wang X, Wang G. Fully automatic liver segmentation in CT images using modified graph cuts and feature detection. Comput Biol Med; 95:198–208, 2018.
[73] Anter AM, Hassenian AE. Computational intelligence optimization approach based on particle swarm optimizer and neutrosophic set for abdominal CT liver tumor segmentation. J Comput Sci ; 25:376–87, 2018.

[74] Masoumi H, Behrad A, Pourmina MA, Roosta A. Automatic liver segmentation in MRI images using an iterative watershed algorithm and artificial neural network. Biomed Signal Process Control; 7:429–37, 2012.
[75] Klein S, Staring M, Murphy K, Viergever M A, Pluim J P W, elastix: A Toolbox for Intensity based medical image registration. IEEE Transactions on medical imaging. 29:196-205, 2010.
[76] Stewart C V, Tsai C L, Roysam B, The dual-Bootstrap iterative closest point algorithm with application to Retinal image registration. IEEE Transactions on medical imaging. 20:1379-1394, 2010.
[77] Roche A, Malandain G, Ayache N, Unifying maximum likelihood approaches in medical image registration. inria, epidaure project. 11:71-80, 2004.
[78] Huang X, Moore J, Guiraudon G, Jones D L, Bainbridge D, Ren J, Peters T M, Dynamic 2D ultrasound and 3D CT image Registration of the Beating heart. IEEE Transactions on medical imaging. 28: 1179-1189, 2009.
[79] Aktar M N, Alam M J, Pickering M, Robust rigid registration of CT to MRI Brain Volumes using the SCV Similarity Measure. IEEE. pp. 153-156, 2014.
[80] Alam F, Rahman S U, Challenges and Solutions in Multimodal Medical Image Subregion Detection and registration. Journal of Medical imaging and radiation sciences 50 pp.24-30, 2019.
[81] Cao W, Lyu F, He Z, Cao G, He Z, Multimodal medical image registration based on Feature spheres in Geometric algebra. IEEE Access. 6: 21164-21172, 2018.
[82] Al-Ameen Z., Sulong G., Johar M.G. 'Enhancing the contrast of CT Medical images by employing a Novel image size dependent Normalization technique', International Journal of Bio-science and bio-technology, vol. 4(3) 63-68, 2012.
[83] Al-Ameen Z., Sulong G., Johar M.G. 'Employing a suitable enhancement technique as a Pre-restoration adjustment phase for CT Medical images', International Journal of Bio-science and bio-technology, vol. 5(1) 73-68, 2013.
[84] Jafar I., Ying H., "New algorithms for contrast enhancement in grayscale images based on the variational definition of histogram equalization", Integrated Computer-Aided engg. 15 1-17, 2008.
[85] Niu L, Qian M, Yang W, Meng L, Xiao Y, Wong KKL, Abbott D, Liu X, Zheng H. Surface Roughness Detection of Arteries via Texture Analysis of Ultrasound Images for Early Diagnosis of Atherosclerosis. PLoS One;8, 2013.
[86] Radhakrishnan M, Kuttiannan T. Comparative Analysis of Feature Extraction Methods for the Classification of Prostate Cancer from TRUS Medical Images. Int J Comput Sci Issues;9:171–9, 2012.
[87] Materka A., Strzelecki M. 'Texture analysis methods-A review', Technical University of Lodz, Institute of Electronics, COST B11 report, Brussels 1998.
[88] Guan X., Liang J., Qian Y., Pang J. 'A multi-view OVA model based on decision tree for multi-classification tasks' Knowledge based system 000,1-12, 2017.
[89] Schapire E. R., 'Explaining Adaboost' Department of computer science, Princeton University, 2011.
[90] Liaw A., Wiender M., 'Classification and regression by random Forest' R News, vol.2/3, ISSN 1609-3631, pp.18-22, 2002.
[91] Gnanasekhar P., Nagappan A., Sharavanan S., Saravanan O., Vinodkumar D., Elayabharathi T., Karthik G. 'Investigation on Feature extraction and classification of Medical images', World Academy of Science, Engineering and Technology, Vol: 5, 12-21, 2011.

[92] Islam M.A., Chowdhary R.I., 'Generalized linear models in analysis of repeated measures data 'Springer Singapore, pp. 31-50, 2017.
[93] Ding S., Chen L. 'Intelligent Optimization methods for high-dimensional data classification for support vector machine' intelligent information management, pp. 159-169, 2010.
[94] Lu X, Zhang S, Zha Y, Chen Y, Three dimensional non-rigid registration and fusion for image guided surgery navigation system IEEE. International conference of medical image analysis and clinical Application. 11508577, 2010.
[95] Hota H.S., Shukla S.P., Kiran G.K. 'Review of Intelligent techniques applied for classification and pre-processing of medical image data' International journal of computer sciences vol. 10(1)3, 2013.
[96] Raghu P.P., Yegnanaryana B., "Segmentation of Gabor filtered textures using deterministic relaxation, IEEE Trans. Image processing 5, 1625-1636, 1996.
[97] Namuduri K.R., Mehrotra R., Ranganathan N., "Efficient computation of Gabor filter based multiresolution responses, Pattern recognition 27, 925-938, 1994.
[98] Jain A.K., Ratha N.K., Lakshmana S., "Object detection using Gabor filters, Pattern Recognition 30, 295-309, 1997.
[99] Porat M., Zeevi Y.Y., the generalized Gabor scheme of image representation in biological and machine vision, IEEE Trans. Pattern Analysis Mach. Intell. 10, 452-468, 1988.
[100]Hamamoto Y., Uchimara S., Watanabe M., Yasuda T., Mitani Y., Tomita S., "A Gabor filter based method for recognizing handwritten numerals, Pattern recognition 31, 395-400, 1998.
[101] Dunn D., Higgins W., Wakeley J., "Texture segmentation using 2-D Gabor elementary functions, IEEE Trans. Pattern analysis Mach. Intell. 16, 130-149, 1994.
[102] Mittal D., Kumar V., Saxena S.C., Khandelwal N., Kalra N., 'Neural network based focal liver lesion diagnosis using ultrasound images' computerized medical imaging and graphics, 35 pp.315-323, 2011.
[103] Van Hulle M.M., Tollenaere T., "A modified artificial neural network for texture processing, Neural Networks 6, 7-32, 1993.
[104] Qiao Y.L., Li M., Lu Z.M., "Gabor Filter Based Text Extraction from Digital Document Images" International conference on intelligent information hiding and multimedia, 2006.
[105] Bus R., Liu Z.Q., "Feature measurement and analysis using Gabor filters" IEEE Explore 2008.
[106] Kapur T, Grimson WEL, Wells WM. Segmentation of brain tissue from magnetic resonance images. Med Image Anal; 1:109–27, 1996.
[107] Akselrod-Ballin A, Galun M, Gomori JM, Brandt A, Basri R. Prior knowledge driven multi scale segmentation of brain MRI. In: Proceedings of the 10th International Conference on Medical Image Computing and Computer-Assisted Intervention, 118–26, 2007.
[108] Atkins MS, Mackiewich BT. Fully automatic segmentation of the brain in MRI. IEEE Trans Med Imaging; 17:98–107, 1998.
[109] Rodrigues P., Vilaca J.L., Fonseca J., "An image processing for Liver tumour segmentation" IEEE EMBS, 2011.
[110] Mintz Aaron M., Raicu Daniela S., Furst Jacob D., "Liver segmentation combining Gabor filtering and traditional vector field snake, Proc. SPIE 6914, Medical Imaging 2008: Image Processing, 69141H, 2008.
[111] Joshi D., Londhe N.D., "Automatic Liver tumor detection in abdominal CT Images", IJCTEE, Vol. 3(1), 2013.

[112] Stašák J. A contribution to image semantic analysis. In: Proceedings of Electronic Computers and Informatics ECI, Košice, Poland: The University of Technology, Department of Computers and Informatics of FEI, pp. 132–4, 2004.
[113] Gupta S, Sandhu PS, Mohan N. Implementing color image segmentation using biogeography based optimization. In: Proceedings of International Conference on Computer and Communication Technologies, 167–70, 2012.
[114] Gómez O, González JA, Morales EF. Image segmentation using automatic seeded region growing and instance-based learning. In: Proceedings of the Congress on Pattern Recognition 12th Iberoamerican Conference on Progress in Pattern Recognition, Image Analysis and Application, 192–201, 2007.
[115] Wang Z, Jensen JR, Im J. An automatic region-based image segmentation algorithm for remote sensing applications. Environ Modell Softw; 25:1149–65, 2010.
[116] Demirhan A, Törü M, Güler I. Segmentation of tumor and edema along with healthy tissues of brain using wavelets and neural networks. IEEE J Biomed Health Inform; 19:1451–8, 2015.
[9]
[117] Corso JJ, Sharon E, Dube S, El-Saden S, Sinha U, Yuille A. Efficient multilevel brain tumor segmentation with integrated Bayesian model classification. IEEE Trans Med Imaging; 27:629–40, 2008.
[118] Shen S, Sandham W, Granat M, Sterr A. MRI fuzzy segmentation of brain tissue using neighborhood attraction with neural-network optimization. IEEE Trans Inf Technol Biomed; 9:459–67, 2005.
[119] Maes F, Vandermeulen D, Suetens P, Medical image registration using mutual information. Proceedings of the IEEE. 91: 1699-1722, 2003.
[120] Hutton B F, Braun M, Thurfjell L, Lau D Y H, Image registration: an essential tool for nuclear medicine. European journal of nuclear medicine. 29: 559-577, 2002.
[121] Thevenaz P, Unser M, Optimization of mutual information for multi-resolution Image registration. IEEE Transactions on image processing. 9: 2083-2099, 2000.
[122] Rohlfing T, Maurer C R, Non-rigid image registration in shaped memory multiprocessor environments with application to Brains, Breasts, and Bees. IEEE transactions on information technology in biomedicine. 7: 16-25, 2003.
[123] Kumar P, Bhalero S, Detection of tumor in liver using image segmentation and registration technique. IOSR Journal of Electronics and communication engineering p-ISSN: 2278-8735. 9 :110-115, 2014.
[124] Tsai D.M., Wu S.K., Chen M.C., "Optimal Gabor filter design for texture segmentation using stochastic optimization" Image and vision computing, Vol:19(5), pp.299-306, 2001.
[125] V L Nangai. Automatic brain tumor medical image classification using hyperbolic Hopfield neural network. J Chem Pharm Res;7:190–9, 2015.
[126] Lu J, Wang D, Shi L, Heng PA. Automatic liver segmentation in CT images based on support vector machine. Proc. - IEEE-EMBS Int. Conf. Biomed. Heal. Informatics Glob. Gd. Chall. Heal. Informatics, BHI 2012, vol. 25, China: IEEE; pp. 333–6, 2012.
[127] Nurzyńska K, Kubo M, Muramoto K. Grey Scale Texture Classification Method Comparison Considering Object and Lighting Rotation. Int J Comput Theory Eng;5:19–23, 2013.
[128] Ahirwar A. Study of Techniques used for Medical Image Segmentation and Computation of Statistical Test for Region Classification of Brain MRI. Int J Inf Technol Comput Sci

2013;5:44–53, 2013.
[128] Lee C.-C., Chen S.-H. , Hong-Ming Tsai H.-M., Chung P.-C., Chiang Y.-C., "Discrimination of liver diseases from CT images based on Gabor filters", 19th IEEE International Symposium on CBMS, pp. 203-206, 2006.
[129] C. Karthikeyan, B. Ramadoss, S. Baskar, "Segmentation algorithm for CT images using Morphological operation and artificial neural network, international journal of signal processing, image processing and pattern recognition, vol. 5(2), 2012.
[130] Mittal D., Kumar V., Saxena S.C., Khandelwal N., Kalra N., "Enhancement of the ultrasound images by modified anisotropic diffusion method", medical and biological engg. Imaging and graphics 48, 1281-1291- 323, 2011.
[131] Lu J., Wang D., Shi L., Heng P.A. 'Automatic liver segmentation in CT images based on support vector machine', IEEE-EMBS International Conference on Biomedical and Health Informatics, pp. 333-336, 2012.
[132] Nurzynska K., Kubo M., Muramoto K. 'Grey scale texture classification method comparison considering object and lighting rotation' International journal of computer theory and engineering, 5(1), 19-23,2013.
[133] S. Su, Y. Sun, "Key techniques research in computer- aided Hepatic Lesion Diagnosis system based on Multi- phase CT images", 4th International CISP, vol. 4, pp. 1921-1927, 2011.
[134] Mostafa A., Hefny H., Ghali N.I., Hassanien A.E., Schaefer G., "Evaluating the effects of image filters in CT liver CAD system", IEEE-EMBS International Conference on Biomedical and Health Informatics, pp. 448-451, 2012.
[135] Akram M.U., Khanum A., Iqbal K., "An automated system for liver CT Enhancement and segmentation", ICGST-GVIP Journal, Vol. 10(IV), 2010.
[136] Varshney L.V., "Abdominal organ segmentation in CT scan images: A survey", Applications of fuzzy set theory, Vol. 4578, pp. 520-528, 2007.
[137] Davis B.C., Foskey M., Rosenman J., Goyal L., Chang S., Joshi S., "Automatic segmentation of Intra-Treatment CT images for Adaptive radiation therapy of the prostate", MICCAI, LNCS 3749: pp. 442-450, 2005.
[138] Xiong W., Zhou J., Tian Q., Liu J.J., Qi Y., Leow W.K., Han T., Wang S.-C., "Performance benchmarking of liver CT image segmentation and volume estimation", Proc. Of SPIE Vol. 6919, 2008.
[139] J. Liu, Wang Z., Zhang R, "Liver cancer CT image segmentation methods based on watershed algorithm", International conference proceedings on computer intelligence and software proceedings, IEEE, 2009.

APPENDIX A

SEGMENTATION RESULTS

The segmented results from the CT and MR images tumor, with the original image and the segmented output image original part. The different samples are the parts of a particular series in continuation. The examples are from both the CT and MR images. The last part represents the form of a large tumor size in the liver region in comparison of the other parts.

CT Metastases	
Original image	**Segmented tumor result**
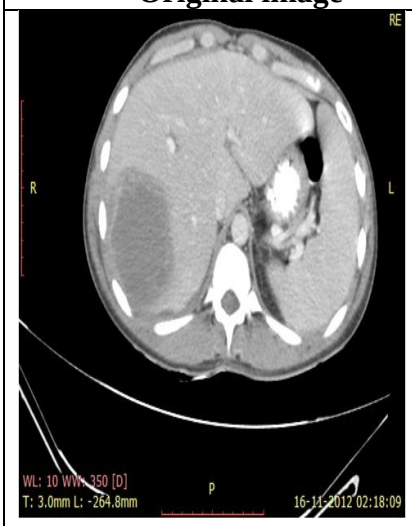	
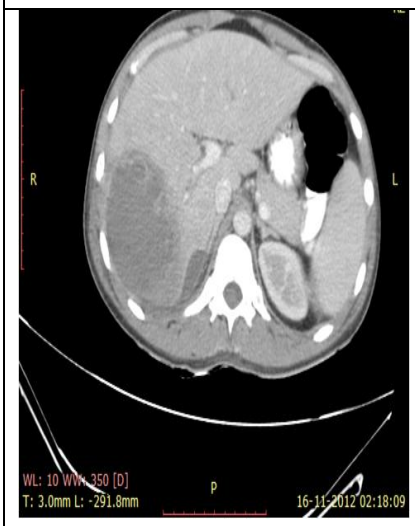	

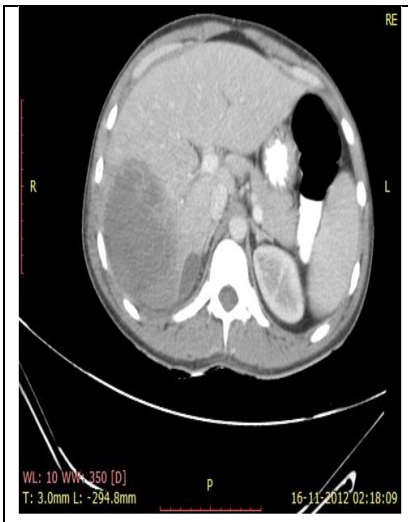
RE
R
L
WL: 10 WW: 350 [D]
T: 3.0mm L: -294.8mm
P
16-11-2012 02:18:09

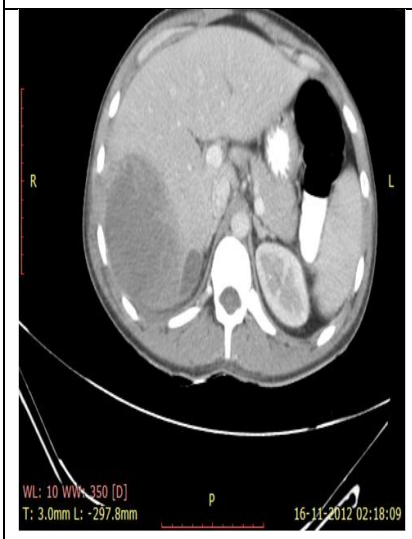
R
L
WL: 10 WW: 350 [D]
T: 3.0mm L: -297.8mm
P
16-11-2012 02:18:09

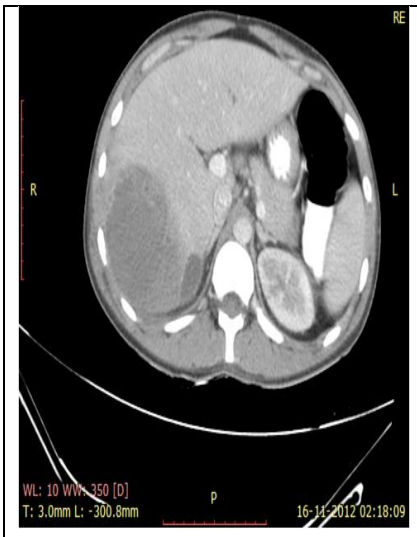 RE R L WL: 10 WW: 350 [D] T: 3.0mm L: -300.8mm P 16-11-2012 02:18:09	

MR Metastases	
Original image	**Segmented tumor result**
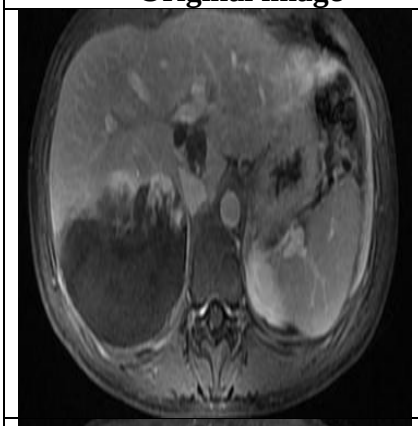	
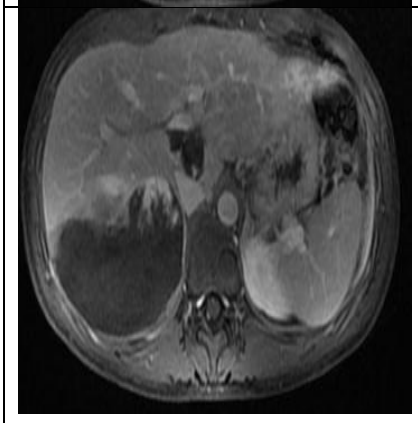	
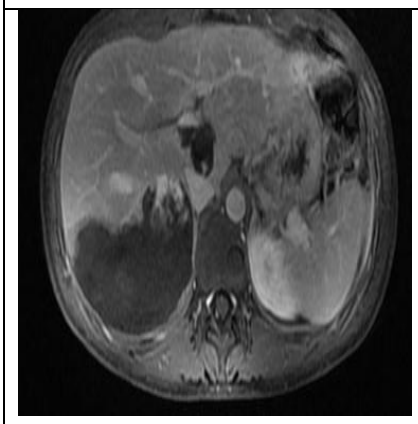	

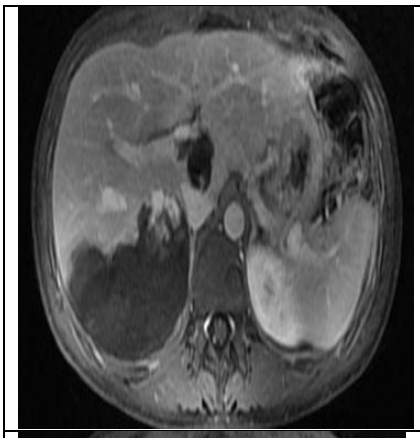	
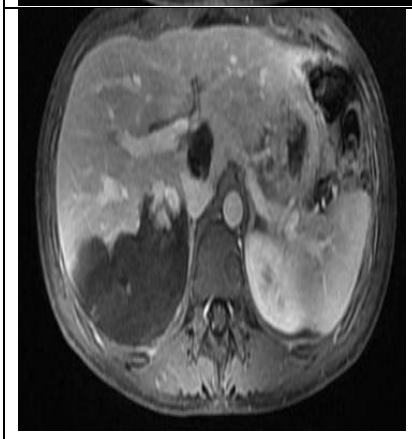	
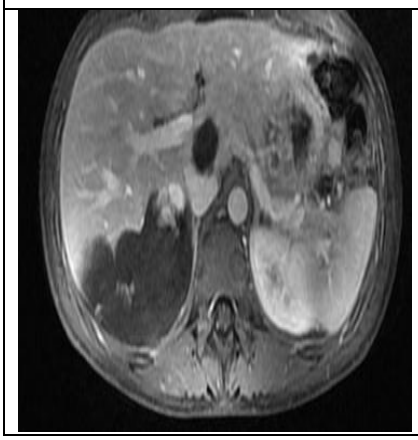	

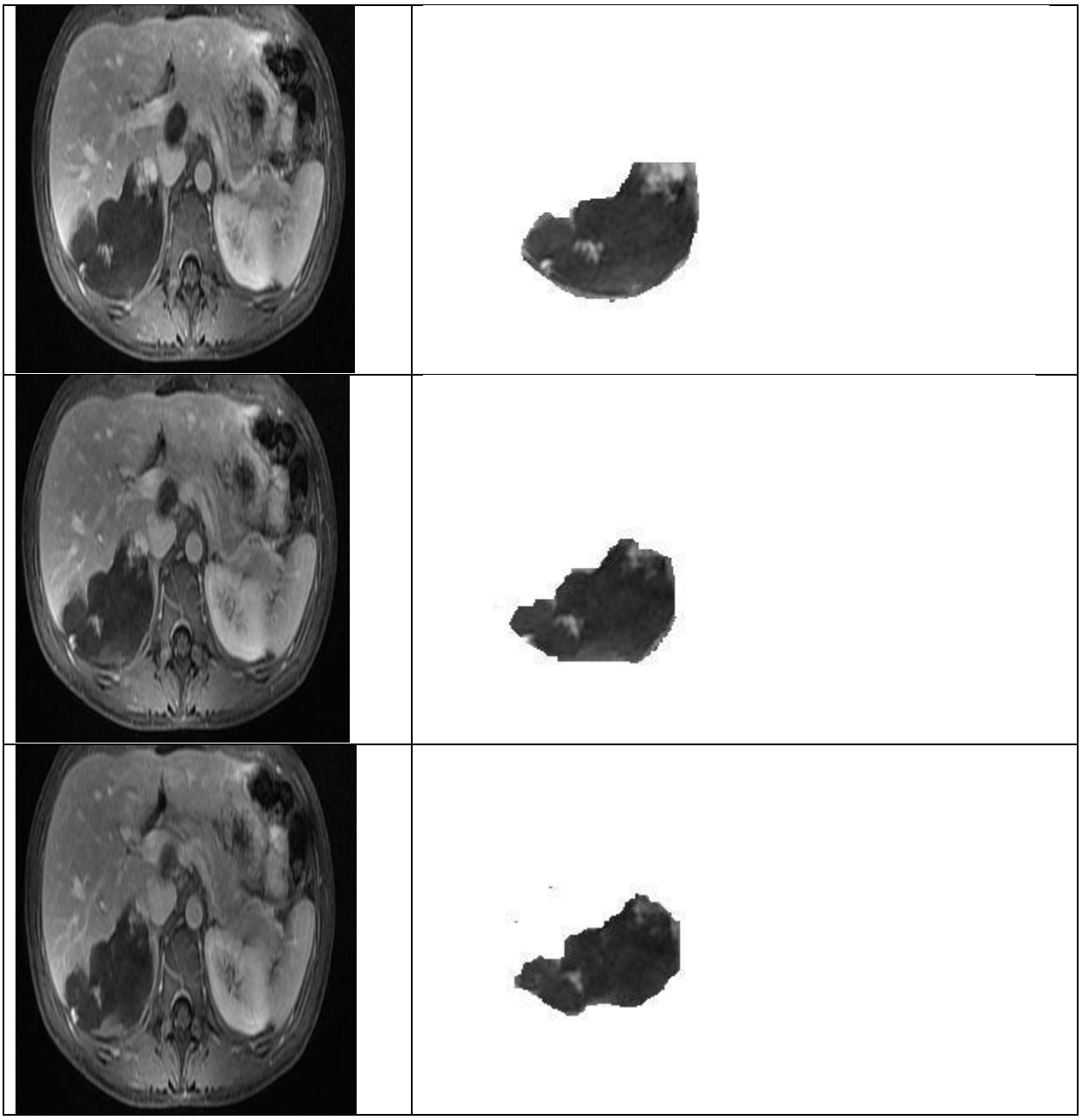

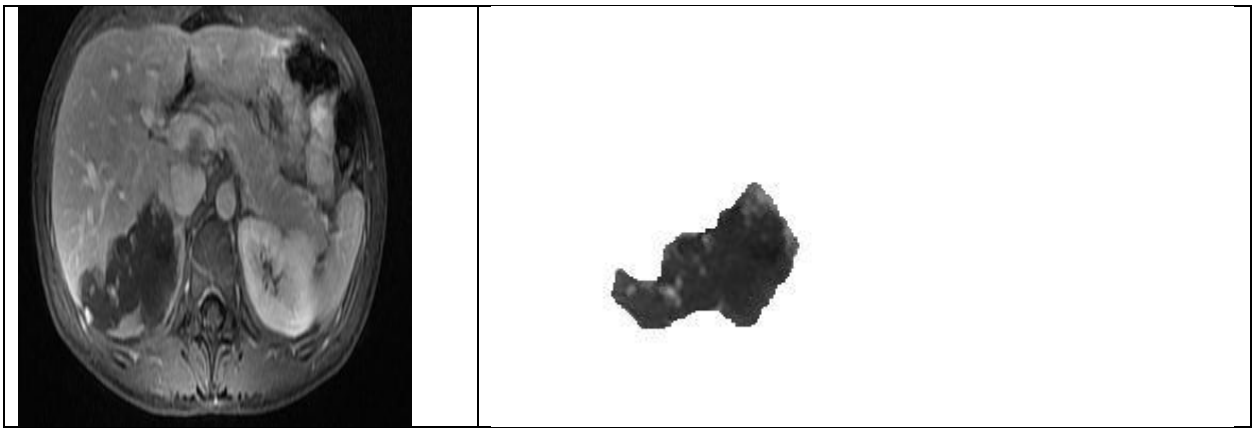

CT HCC	
Original image	**Segmented tumor result**
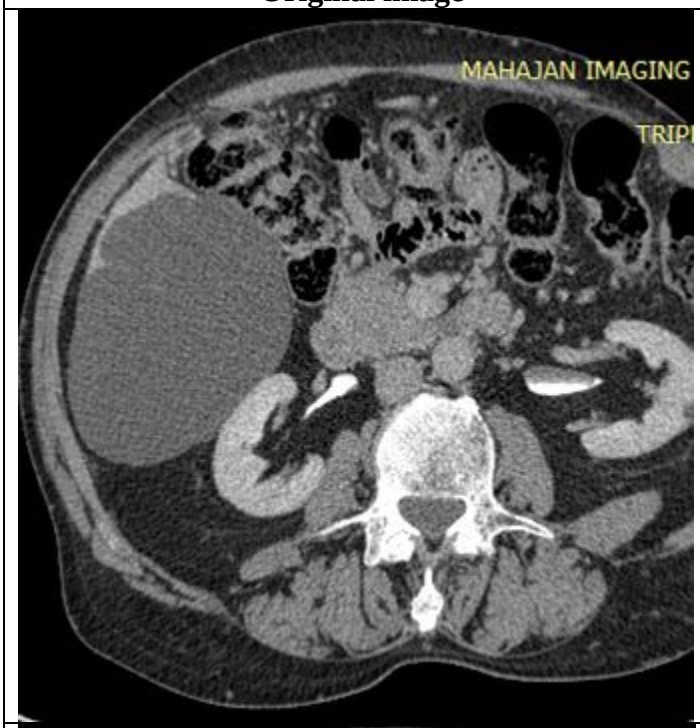	
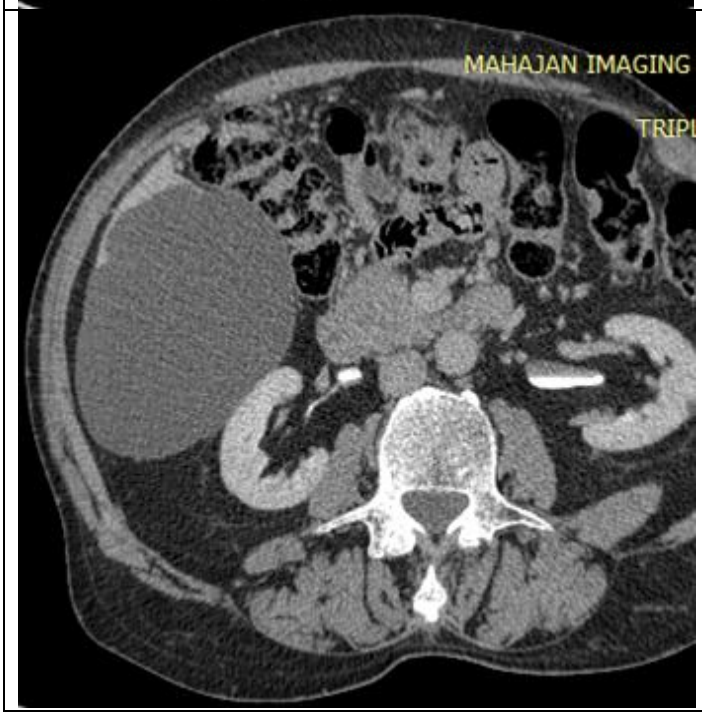	

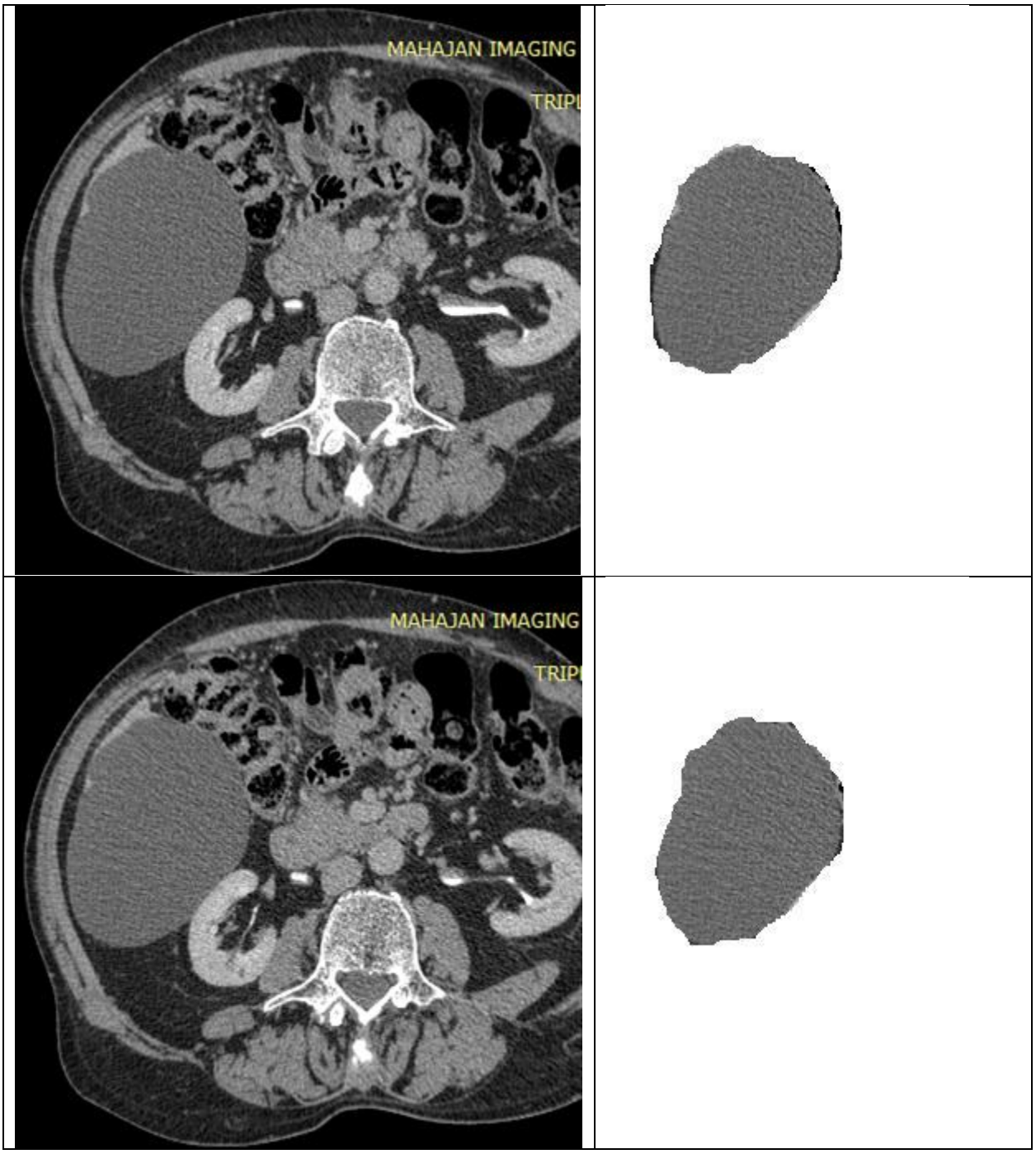
MAHAJAN IMAGING
TRIPI
MAHAJAN IMAGING
TRIPI

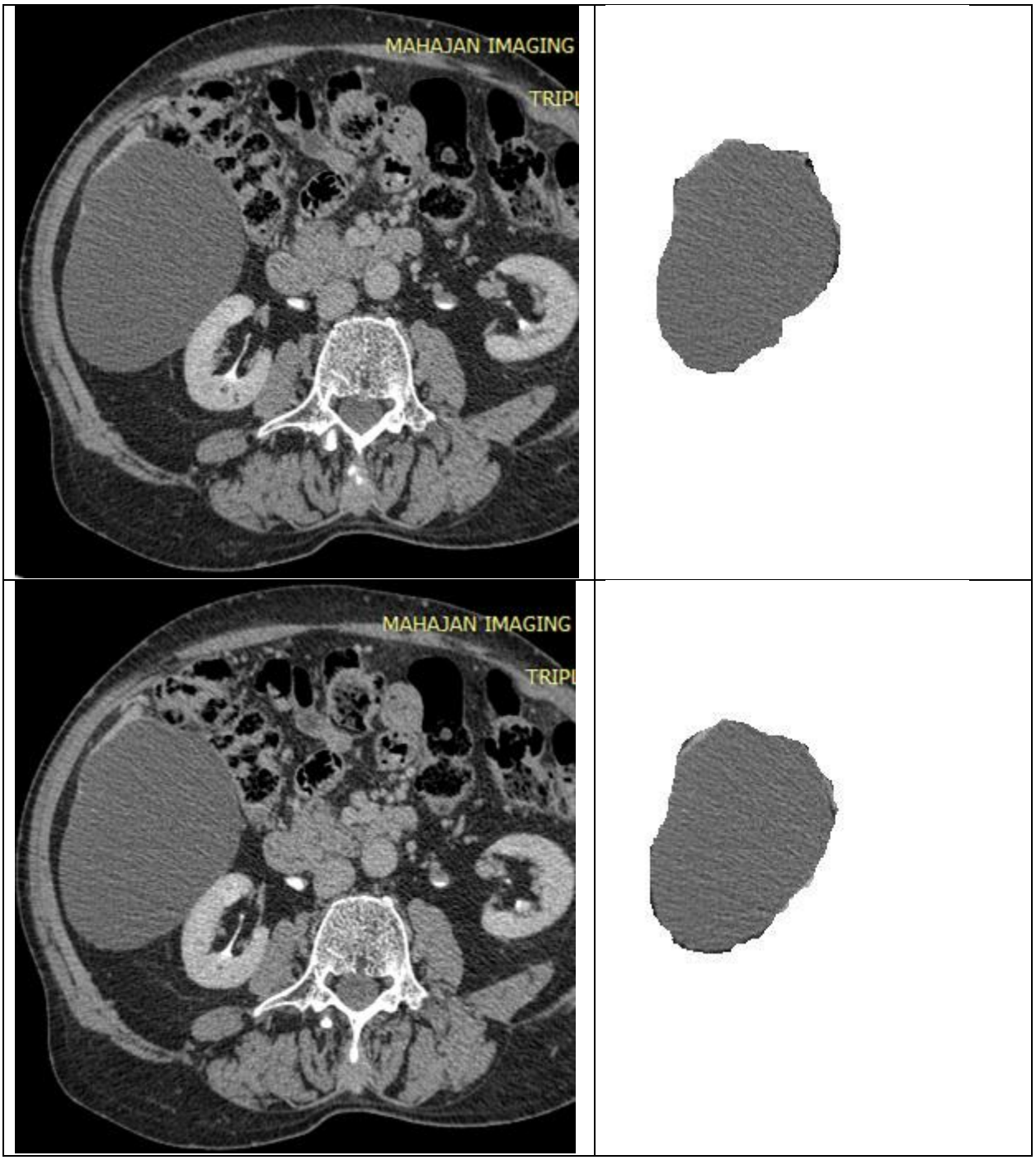
MAHAJAN IMAGING
MAHAJAN IMAGING

APPENDIX B

REGISTRATION RESULTS

The registered images results samples that are the output of the registered images with the different combinations of the fixed image and the moving image. The images presented here are the group of the three forms output registered images, with the first image as the difference checkerboard, the next is the green magenta and the last is the red cyan using the two features, MSER and the SURF. These presented samples have the largest liver region with a suitable tumor.

- The three images combination using the MSER with the Triple phase CT as the fixed image and the arterial phase as the moving image.

Checkerboard	Green-Magenta	Red-Cyan
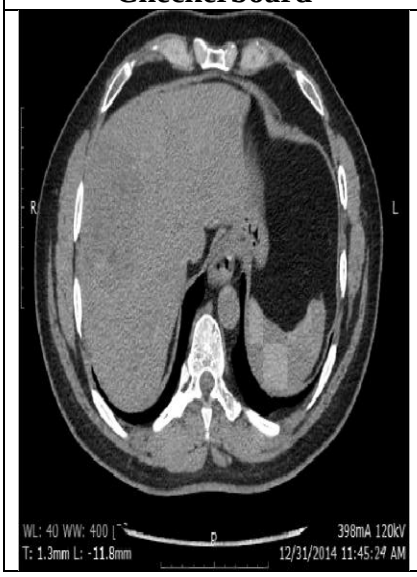	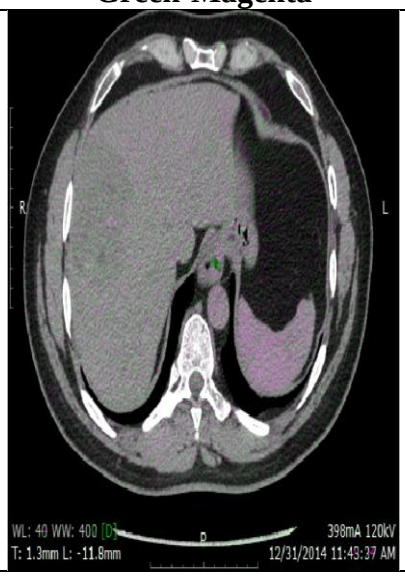	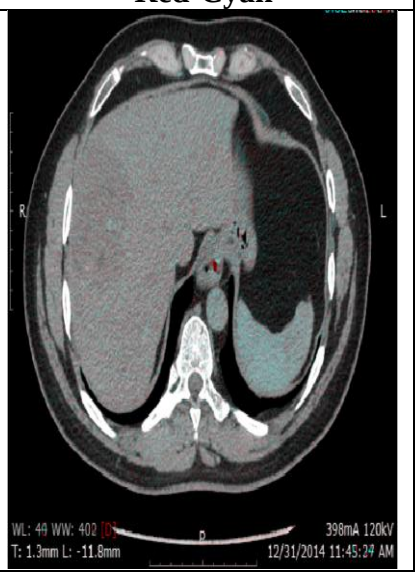

- The three images combination using the SURF with the Triple phase CT as the fixed image and the arterial phase as the moving image.

Checkerboard	Green-Magenta	Red-Cyan
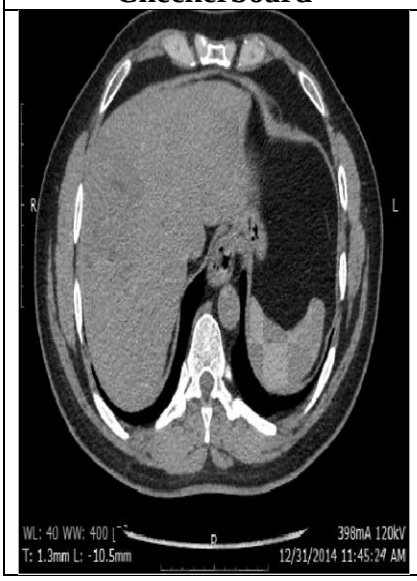	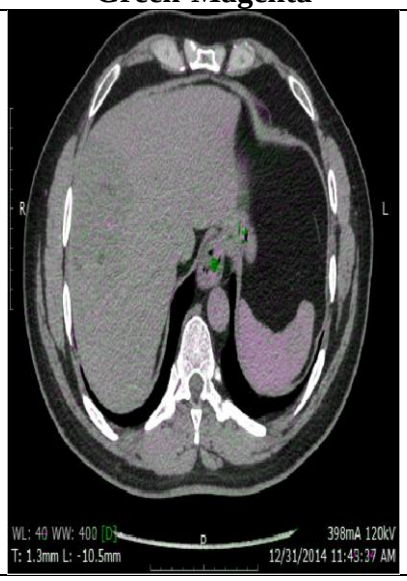	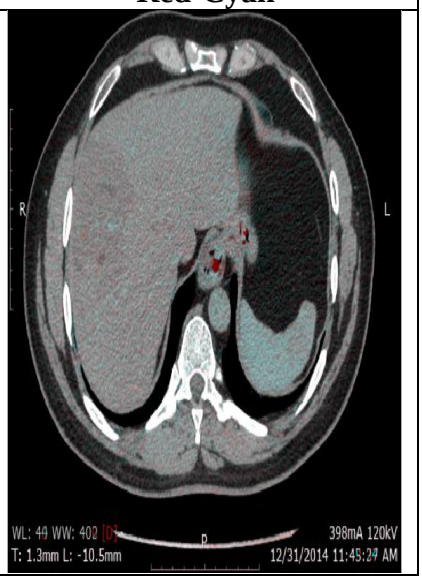

- The three images combination using the MSER with the Triple phase CT as the fixed image and the venous phase as the moving image.

Checkerboard	Green-Magenta	Red-Cyan
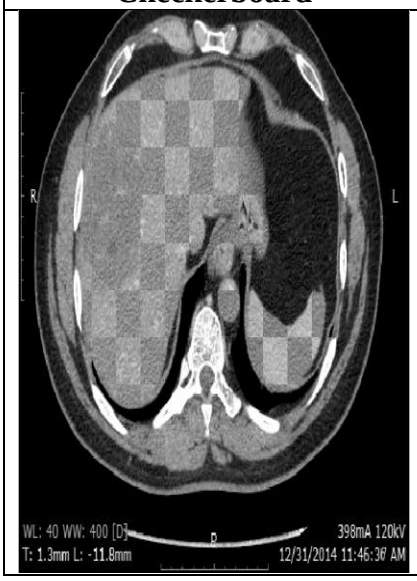	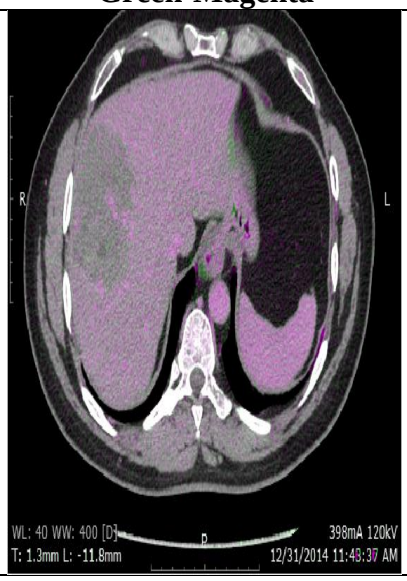	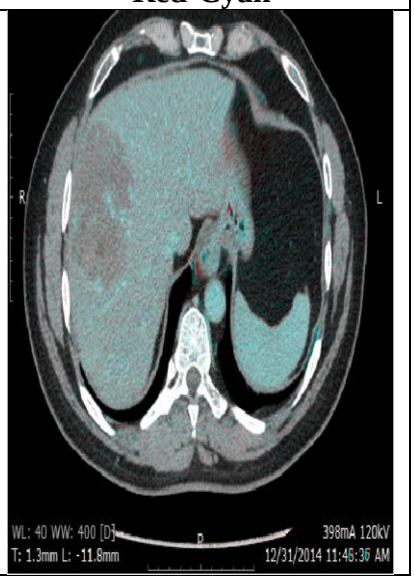

- The three images combination using the SURF with the Triple phase CT as the fixed image and the venous phase as the moving image.

Checkerboard	Green-Magenta	Red-Cyan
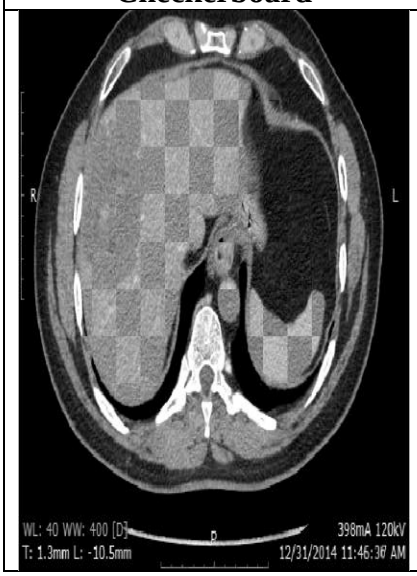	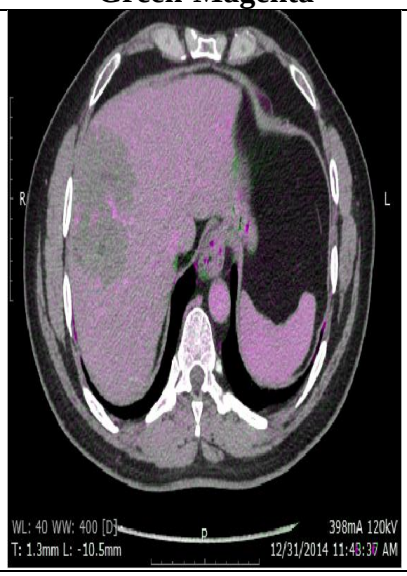	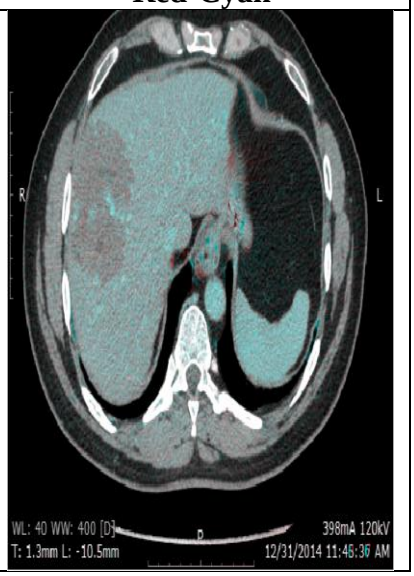

- The three images combination using the MSER with the Triple phase CT as the fixed image and the delayed phase as the moving image.

Checkerboard	Green-Magenta	Red-Cyan
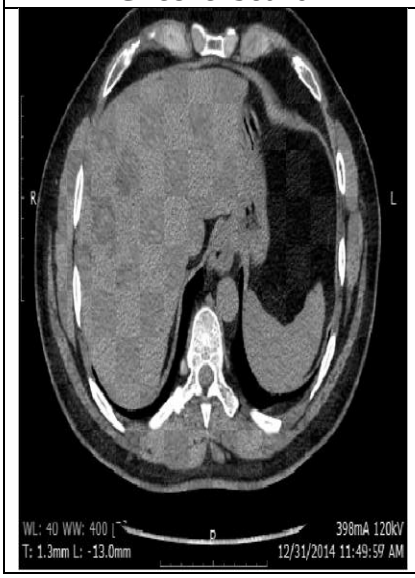	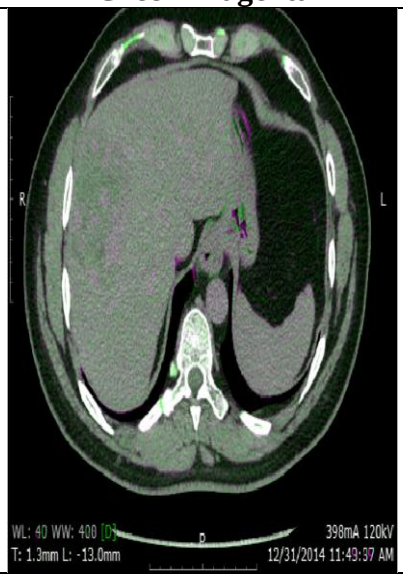	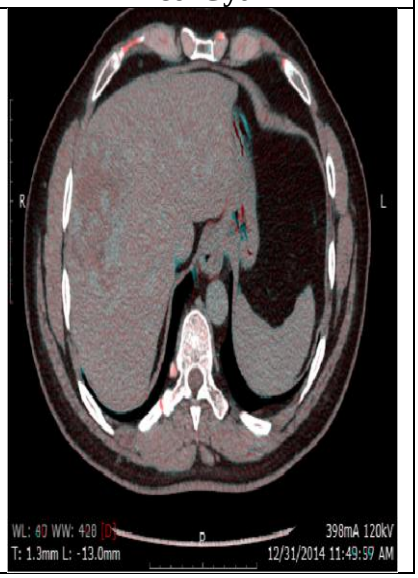

- The three images combination using the SURF with the Triple phase CT as the fixed image and the delayed phase as the moving image.

Checkerboard	Green-Magenta	Red-Cyan
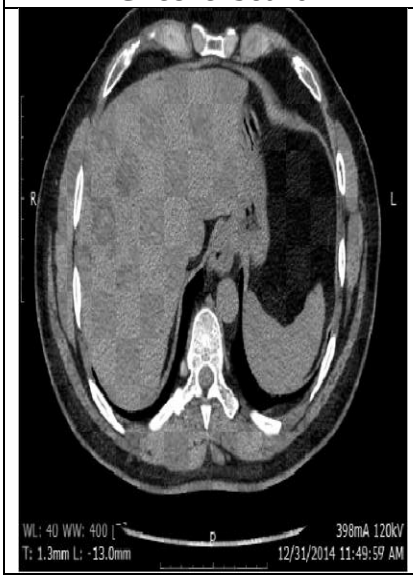	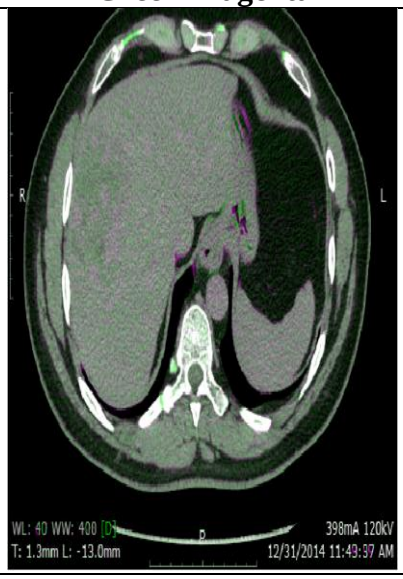	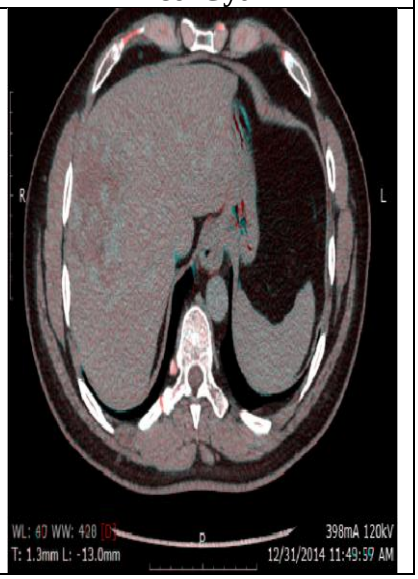

- The three images combination using the MSER with the Triple phase CT as the fixed image and the delayed 10 min. as the moving image.

Checkerboard	Green-Magenta	Red-Cyan
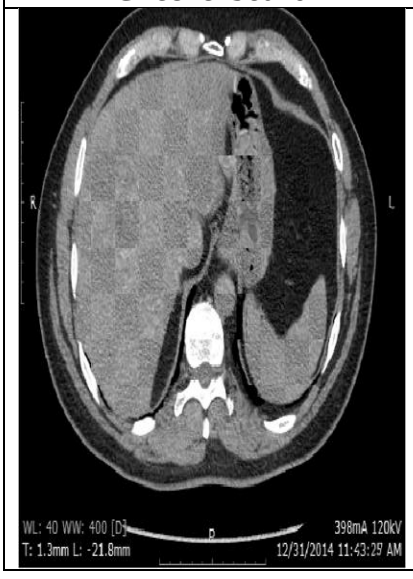	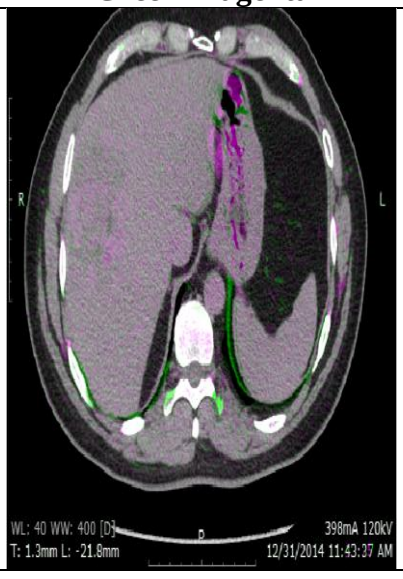	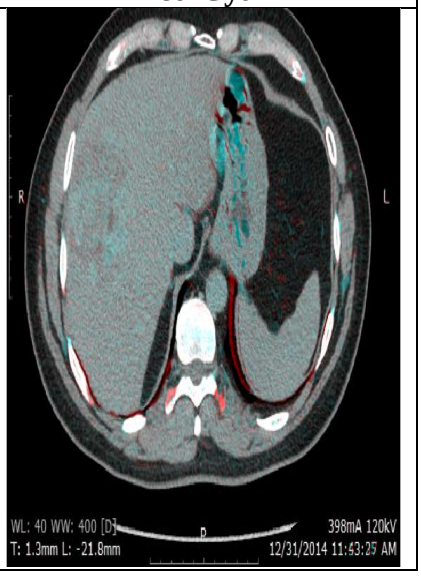

- The three images combination using the SURF with the Triple phase CT as the fixed image and the delayed 10 min. as the moving image.

Checkerboard	Green-Magenta	Red-Cyan
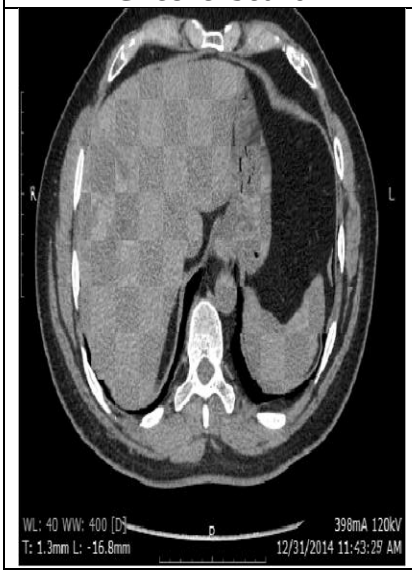	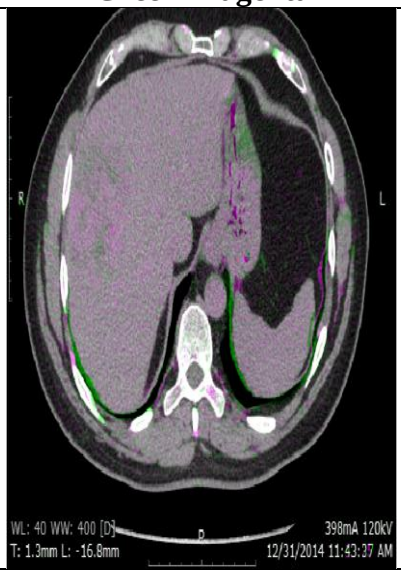	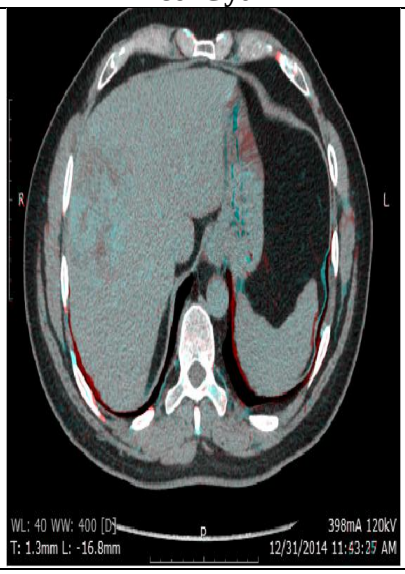

- The three images combination using the MSER with the arterial phase as the fixed image and the venous phase as the moving image.

Checkerboard	Green-Magenta	Red-Cyan
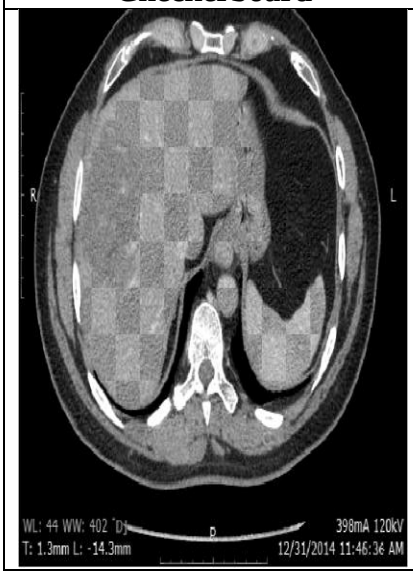	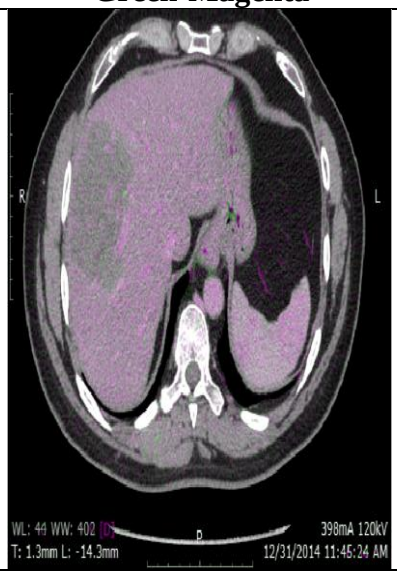	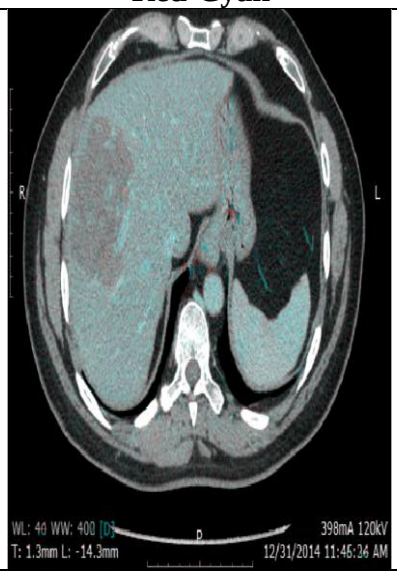

- The three images combination using the SURF with the arterial phase as the fixed image and the venous phase as the moving image.

Checkerboard	Green-Magenta	Red-Cyan
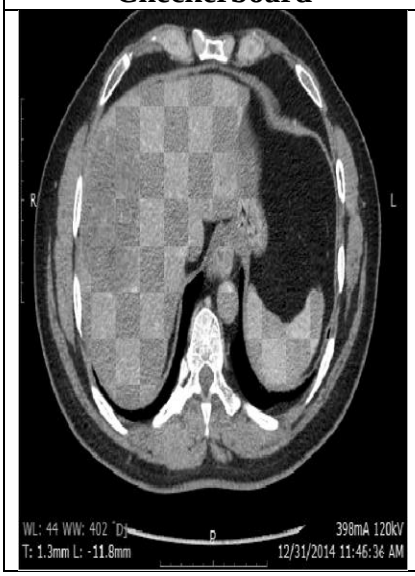	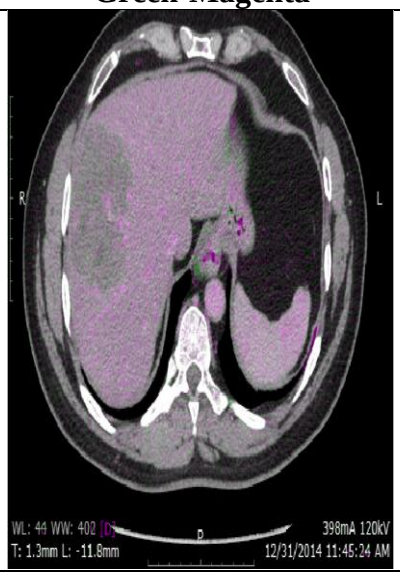	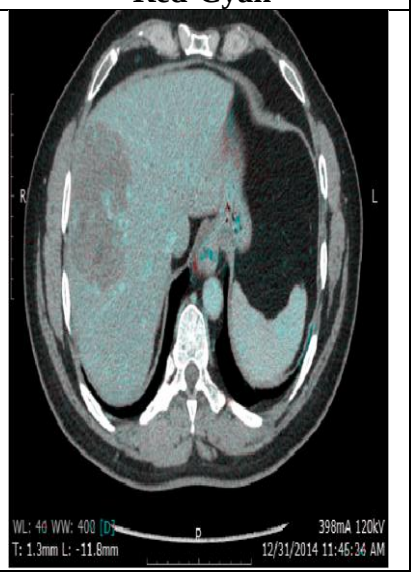

- The three images combination using the MSER with the arterial phase as the fixed image and the delayed as the moving image.

Checkerboard	Green-Magenta	Red-Cyan
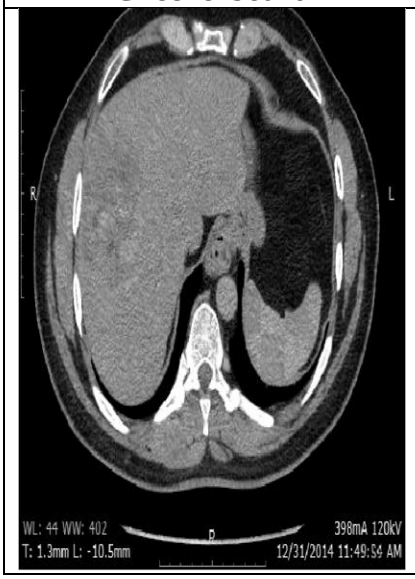	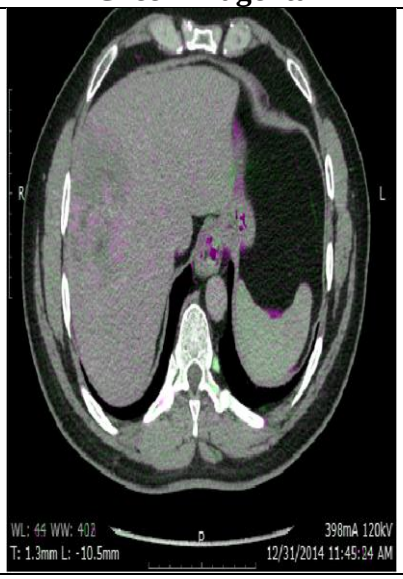	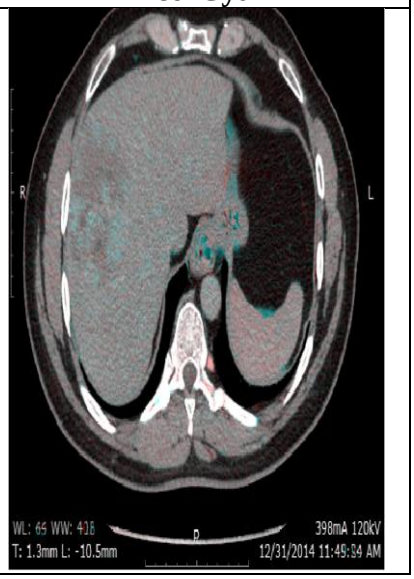

- The three images combination using the SURF with the arterial phase as the fixed image and the delayed as the moving image.

Checkerboard	Green-Magenta	Red-Cyan
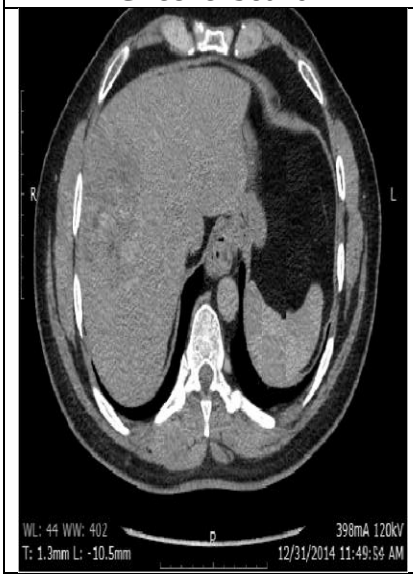	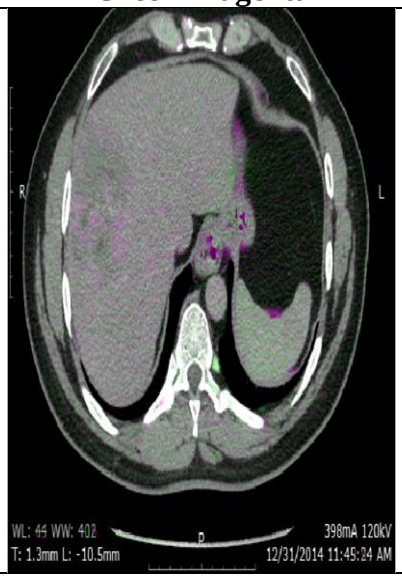	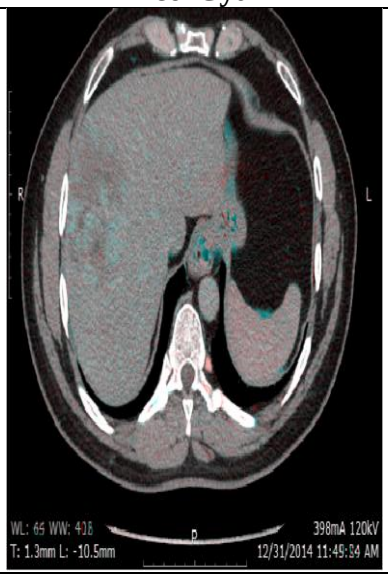

- The three images combination using the MSER with the arterial phase as the fixed image and the delayed 10 min. as the moving image.

Checkerboard	Green-Magenta	Red-Cyan
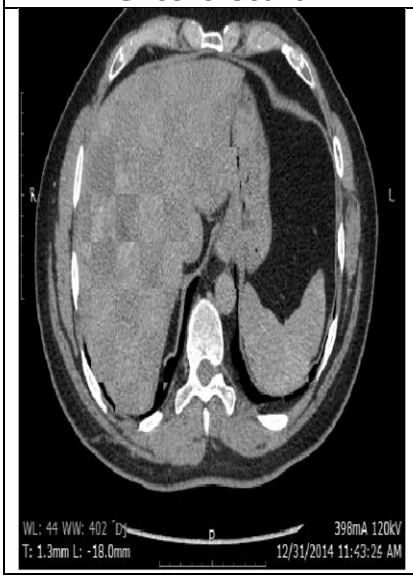	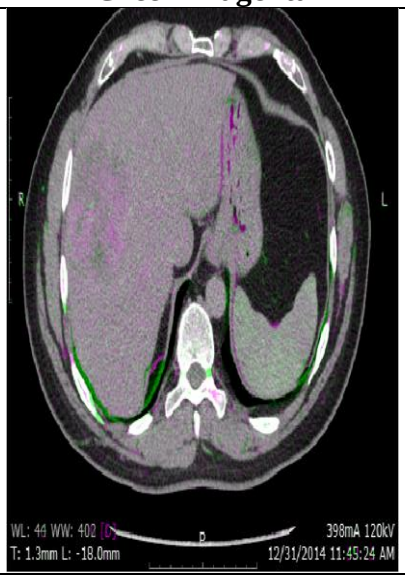	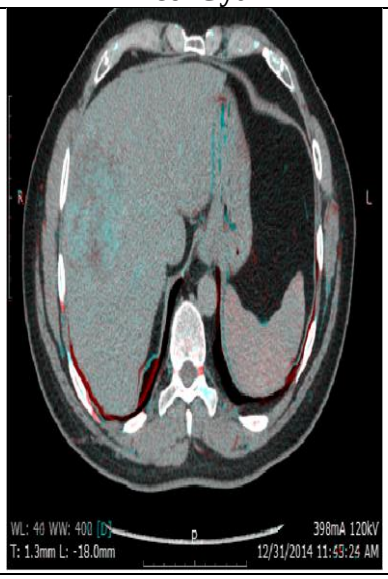

- The three images combination using the SURF with the arterial phase as the fixed image and the delayed 10 min. as the moving image.

Checkerboard	Green-Magenta	Red-Cyan
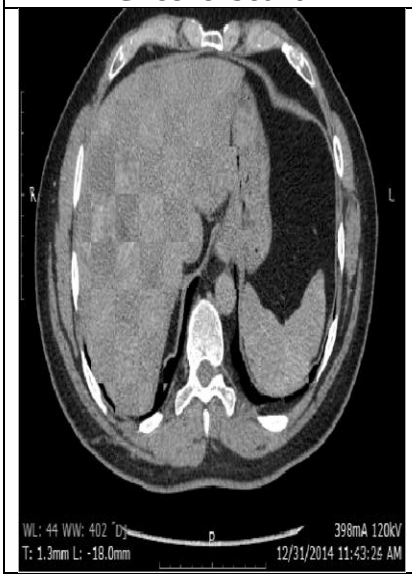	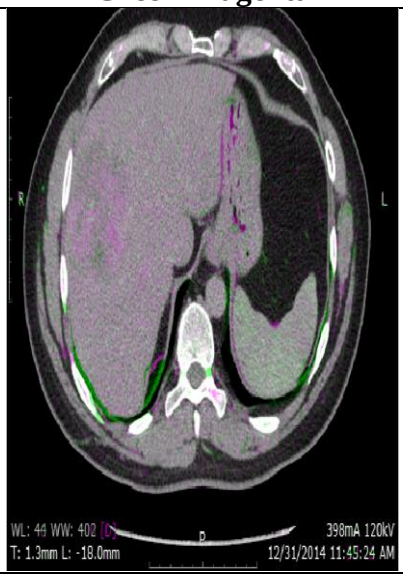	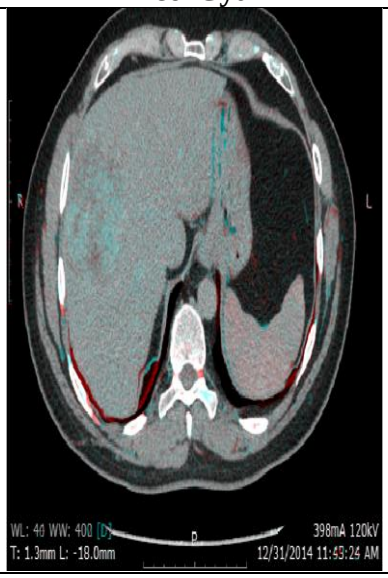

- The three images combination using the MSER with the venous phase as the fixed image and the delayed as the moving image.

Checkerboard	Green-Magenta	Red-Cyan
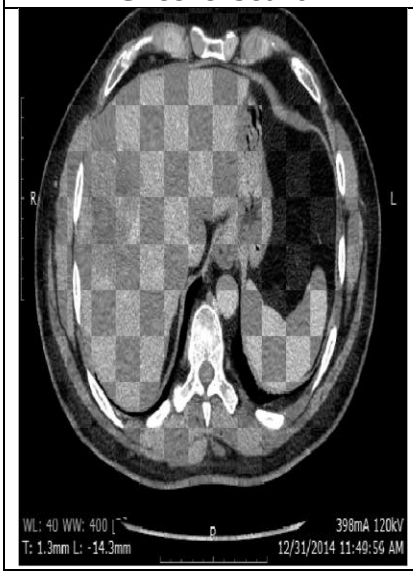	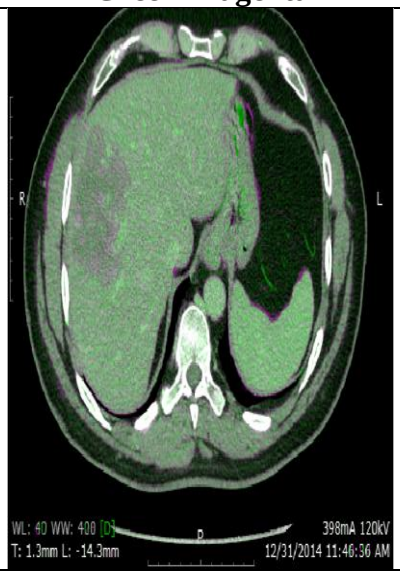	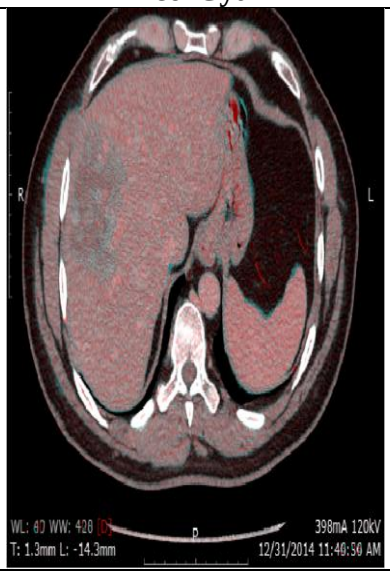

- The three images combination using the SURF with the venous phase as the fixed image and the delayed as the moving image.

Checkerboard	Green-Magenta	Red-Cyan
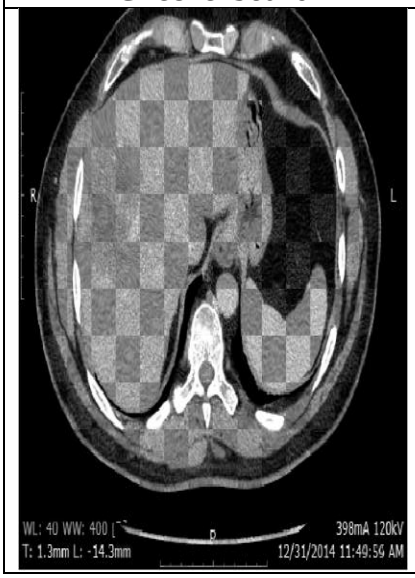	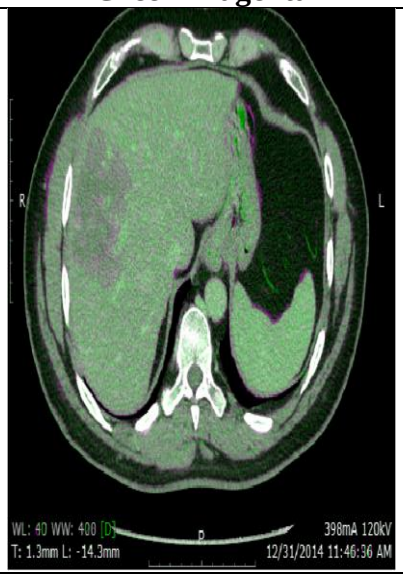	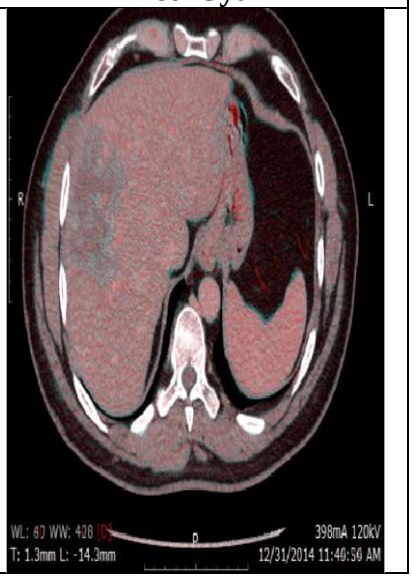

- The three images combination using the MSER with the venous phase as the fixed image and the delayed 10 min. as the moving image.

Checkerboard	Green-Magenta	Red-Cyan
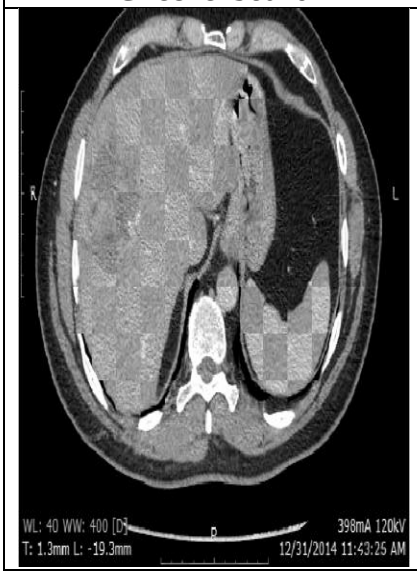	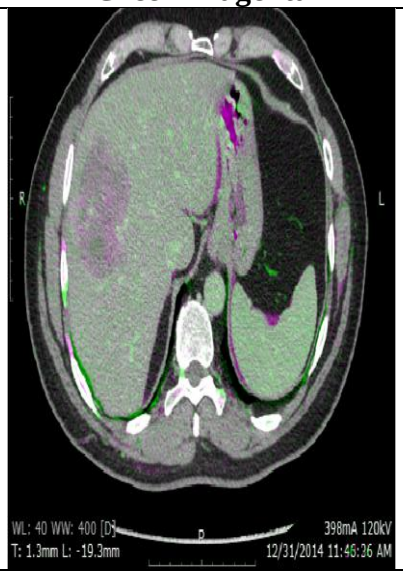	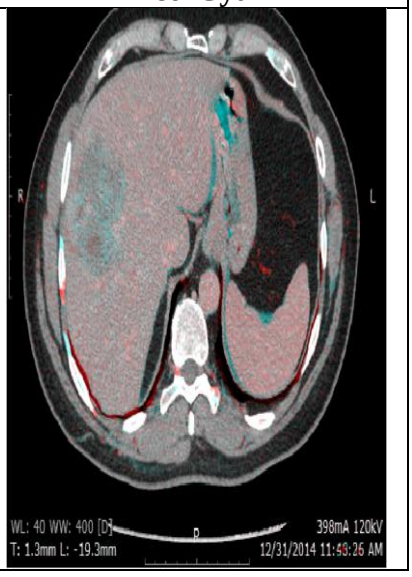

- The three images combination using the SURF with the venous phase as the fixed image and the delayed 10 min. as the moving image.

Checkerboard	Green-Magenta	Red-Cyan
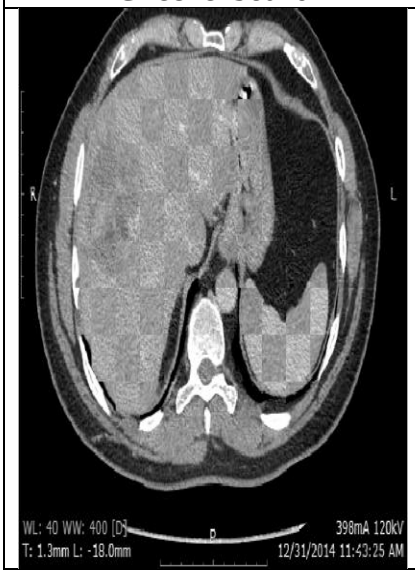	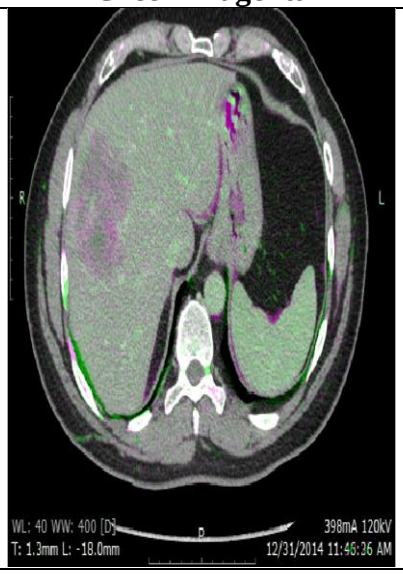	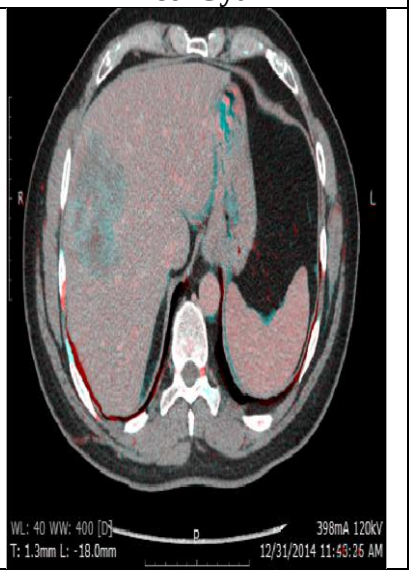

- The three images combination using the MSER with the delayed as the fixed image and the delayed 10 min. as the moving image.

Checkerboard	Green-Magenta	Red-Cyan
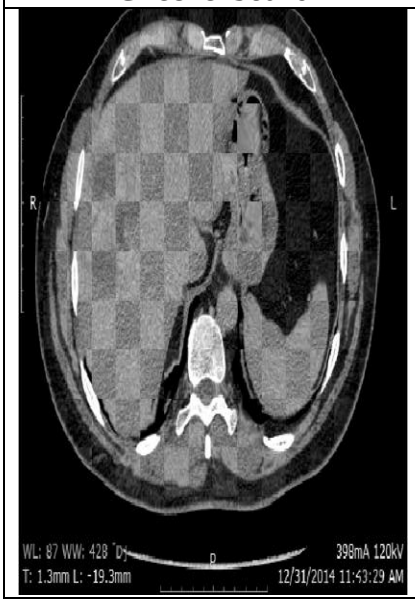	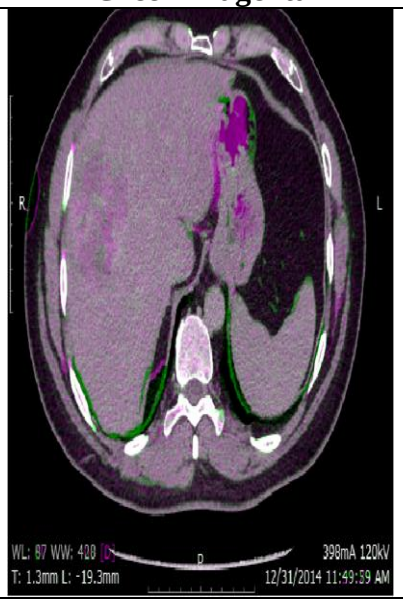	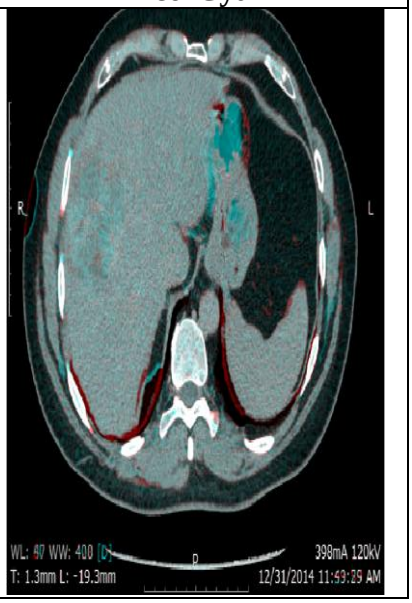

- The three images combination using the SURF with the delayed as the fixed image and the delayed 10 min. as the moving image.

Checkerboard	Green-Magenta	Red-Cyan